TECHNISCHE UNIVERSITÄT WIEN

D I P L O M A R B E I T

Electrochemical properties of (La,Sr)(Cr,Mn)O$_{3-\delta}$ thin film electrodes

Ausgeführt am Institut für

Chemische Technologien und Analytik

der Technischen Universität Wien

unter Anleitung von

Univ.-Prof. Dipl.-Phys. Dr.rer.nat. Jürgen Fleig und

Univ.Ass. Dipl.-Ing. Dr.techn. Alexander Karl Opitz

Projektass. Dipl.-Ing. Dr.techn. Matthias Gerstl

durch

Maximilian Morgenbesser, BSc.

Lokomotivstraße 1 / 4

2700 Wiener Neustadt

Wien, 28. September 2016

Geschätzte Leserin! Geschätzter Leser!

Während ich dieses Vorwort tippe, denke ich an die Arbeit, die mich im letzten Jahr begleitet hat; eine Arbeit, auf die ich mit Interesse, Freude und Begeisterung zurückblicke. Vieles habe ich gelernt, einiges erkannt und so manches gar zu verstehen geglaubt. Zu den Zuvorgenannten mag sich auch ein bisschen Wehmut gesellen. Ein Abschnitt geht zu Ende – eine Gelegenheit, dieses letzte Jahr im Geiste Revue passieren zu lassen: Pechini, PLD, Leitfähigkeitsmessungen, EMRS Spring Meeting 2016, Forschungszentrum Jülich, die montäglichen Besprechungen, …

Es sind viele Eindrücke. Es sind Eindrücke, die in Erinnerung bleiben werden. Ich möchte diese Stelle nützen, um mich bei all jenen bedanken, die dies überhaupt erst möglich gemacht haben:

An erster Stelle möchte ich mich bei Professor Jürgen Fleig für die Möglichkeit bedanken, meine Diplomarbeit in seiner Arbeitsgruppe durchzuführen.

Besonderer Dank gilt auch den Betreuern meiner Diplomarbeit, Matthias und Alex. Danke für eure Geduld, eure Erklärungen und die zahlreichen Ergebnisdiskussionen.

Weiters möchte ich mich bei meinen Zimmergenossinnen, Julia und Kathi, bedanken. Für die zahlreichen Gespräche mit Julia – subversiver und konspirativer Klatsch aus der Uniwelt, Urlaubspläne, Verzweiflung ob der Diplomarbeit und das Wochenende. Für die neuen Einblicke in die Welt des Spitzensportes, die ich durch Kathi gewonnen habe.

Außerdem möchte ich mich bei der gesamten Arbeitsgruppe bedanken: Tobi, Tschisi, Alex, Plüsch, Edvinas, Markus, Alex, Andi, Gregor, Steffi, Alex, Bernhard, Georg, Matthias, Michael, Julia und Kathi. Für das angenehme Klima in der Arbeitsgruppe, die zahlreichen Gespräche über Verschwörungstheorien und Pseudowissenschaft, die gemeinsamen Mittagessen und die Gewissheit, dass immer jemand da ist, den man fragen kann, wenn gar nichts mehr geht. Dafür – und für vieles mehr – möchte ich euch danken.

Weiterer Dank gebührt Werner Artner für die Unterstützung im Röntgenzentrum und Elisabeth Eitenberger für die Arbeit am Elektronenmikroskop.

Schlussendlich möchte ich mich bei meiner Familie bedanken. Meine Eltern, die mir mein Studium ermöglicht haben und mich in so vielen weiteren Wegen unterstützt haben. Die Liste der Dinge, für die euch Dank gebührt, könnte eine weitere Arbeit füllen; dafür an dieser Stelle ein allumfassendes Dankeschön. Auch bei meiner Freundin möchte ich mich bedanken, für die moralische Unterstützung und den IT-Support.

Sollte ich jemanden vergessen haben: Auch dir sei hier gedankt.

Nun möchte ich meine Diplomarbeit noch kurz mit ein paar Worten einleiten: Diese Diplomarbeit enthält keine selbstgezeichneten Mandalas, keine Paint-Pläne der Donauinsel, kein Channeling spiritueller Geister, keinen Beweis der Hohlerde und keine Originalfotographien von Ufos. Dennoch – oder gerade deshalb: Viel Vergnügen beim Lesen!

Der Autor   Wien, 31. Juli 2016

Abstract

The change from solid oxide fuel cell (SOFC) cathodes with surface path kinetics to mixed conducting cathodes exhibiting a bulk path was one of the most important achievements within the last decade of SOFC research. Also in case of anodes the transition to mixed conducting systems is expected to further increase the performance of SOFCs. A promising material for this application is (La,Sr)(Cr,Mn)$O_{3-\delta}$ (LSCrM), which provides the opportunity of two possible ways of changing its electronic properties:

- the Sr-doping on the A-site
- the Cr:Mn ratio on the B-site.

In this study, LSCrM thin films with both varying Sr content and Cr:Mn ratio were prepared by pulsed laser deposition (PLD). Conductivity measurements on these thin films were carried out in 1 % O_2, 100 % O_2 as well as H_2/H_2O (1:1) atmospheres using the Van-der-Pauw-method. The obtained conductivity data are discussed in terms of the material's defect chemistry. Low Mn contents, for example, decrease the conductivity drastically, most likely due to trapping of charge carriers (electron holes) on the Mn sites. With higher Mn contents, site percolation occurs and much higher conductivities can be obtained. The activation energies for each material's conductivity are calculated from Arrhenius plots and are discussed referring to the corresponding conductivity. A connection between conductivity and activation energy was found. Higher activation energies correspond to lower conductivities at the probed temperatures. Furthermore, the prepared samples demonstrated stability during the time of the measurement under oxidizing as well as reducing conditions.

In the second part of the study selected compositions were also investigated as model-type thin film electrodes on yttria stabilized zirconia (YSZ) electrolytes in H_2/H_2O atmosphere, using a porous Ni/YSZ counter electrode. Electrochemical behavior was characterized by means of impedance measurements and elementary properties such as electrode polarization resistance are discussed referring to the material's conductivity. The polarization resistance in humid H_2 is less dependent on the total conductivity, however, a rather low resistance was observed for $La_{0.9}Sr_{0.1}Cr_{0.2}Mn_{0.8}O_{3-\delta}$ electrodes. Therefore, the Mn concentration appears to affect the polarization resistance to a higher extent.

Kurzfassung

Der Wechsel von Kathoden in Festoxidbrennstoffzellen (SOFC) mit Oberflächenpfadkinetik zu gemischt leitenden Kathoden mit Volumenspfad war eine der wichtigsten Errungenschaften innerhalb des letzten Jahrzehnts in der Festoxidbrennstoffzellenforschung. Auch im Fall der Anoden wird mit dem Übergang zu gemischt leitenden Systemen eine weitere Erhöhung der Leistung der Festoxidbrennstoffzellen erwartet. Ein vielversprechendes Material für diese Anwendung ist (La,Sr)(Cr,Mn)$O_{3-\delta}$ (LSCrM), das die Möglichkeit bietet, die elektronischen Eigenschaften auf zwei Arten zu verändern:

- die Sr-Dotierung am A-Platz
- das Cr:Mn Verhältnis am B-Platz

In dieser Arbeit wurden LSCrM Dünnschichten mit sowohl variierendem Sr Gehalt als auch mit variierendem Cr:Mn Verhältnis mittels gepulster Laserabscheidung (pulsed laser deposition, PLD) hergestellt. Leitfähigkeitsmessungen an diesen Schichten wurden in 1% O_2, 100 % O_2 und H_2/H_2O (1:1) Atmosphären mittels Van-der-Pauw Methode durchgeführt. Die erhaltenen Leitfähigkeitsmessdaten werden im Zusammenhang mit der Defektchemie des Material diskutiert. Niedrige Mn Konzentrationen führen beispielsweise zu einer drastischen Verringerung der Leifähigkeit, höchstwahrscheinlich durch Trapping der Ladungsträger (Elektronenlöcher) auf den Mn Plätzen. Mit höheren Mn Konzentrationen kommt es zur Perkolation der Mn Trap-Niveaus und weitaus höhere Leitfähigkeiten können erreicht werden. Die Aktivierungsenergie für die Leitfähigkeit jedes einzelnen Materials wird mit Hilfe von Arrhenius-Diagrammen bestimmt und im Zusammenhang mit der zugehörigen Leitfähigkeit diskutiert. Dabei wurde ein Zusammenhang zwischen Leitfähigkeit und Aktivierungsenergie erkannt, wobei höhere Aktivierungsenergien im Fall von niedrigeren Leitfähigkeiten zu finden waren. Weiters blieben die hergestellten Proben während der gesamten Messzeit sowohl unter oxidierenden als auch unter reduzierenden Bedingungen stabil.

Im zweiten Teil dieser Arbeit wurde von ausgewählten Zusammensetzungen auch die elektrochemische Aktivität für die H_2-Oxidation untersucht. Diese Experimente wurden an Dünnschicht-Modellelektroden auf Yttriumoxid stabilisierten Zirkoniumdioxid-Elektrolyten in H_2/H_2O Atmosphäre durchgeführt, wobei eine poröse Ni/YSZ Gegenelektrode verwendet wurde. Das elektrochemische Verhalten wurde mittels Impedanzspektroskopie charakterisiert und die grundlegenden Eigenschaften wie Elektrodenpolarisationswiderstand werden im Zusammenhang mit der Leitfähigkeit des Materials diskutiert. Der Elektrodenwiderstand hängt dabei nur schwach von der Gesamtleitfähigkeit ab, allerdings wurde ein niedriger Widerstand für $La_{0.9}Sr_{0.1}Cr_{0.2}Mn_{0.8}O_{3-\delta}$ beobachtet, was durch eine Abhängigkeit des Elektrodenpolarisationswiderstandes vom Mn Gehalt erklärt werden konnte.

Table of Content

1 Introduction

1.1 Motivation

With serious problems concerning fossil fuels, especially the geographic concentration in politically unstable regions, pollution of the environment, release of carbon dioxide, volatility in the oil price and the future shortage of oil, renewable energy sources are on the rise. A very promising technology towards a more sustainable energy supply are fuel cells. Fuel cells can help to solve the problems regarding fossil fuels, they have higher efficiency and may be operated with a large variety of fuels (e.g. hydrogen and hydrocarbons such as methanol, syngas, biogas, methane, diesel reformate, …). Moreover, fuel cells also show great synergy with other renewable energy sources including solar and wind power. Both of them generate power irregularly. The storage of electricity is therefore a huge problem of these techniques. With electrolysis, easily accessible chemicals like water or carbon dioxide can be turned into fuels for fuel cells and then be stored. Hydrogen and carbon monoxide produced this way can also be used in the Fischer-Tropsch synthesis to form hydrocarbons [1-4].

Electrolysis reactions:

$$2\ H_2O\ \rightarrow\ 2\ H_2 +\ O_2$$

$$2\ CO_2\ \rightarrow\ 2\ CO + O_2$$

Fischer-Tropsch synthesis:

$$x\ H_2 + y\ CO\ \rightarrow\ Hydrocarbons +\ y\ H_2O$$
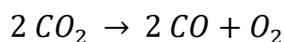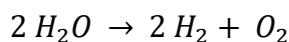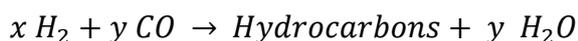
Fuel cells are galvanic cells that directly convert the chemical energy stored in fuels into electrical energy. In the past a number of different types of fuel cells was developed, which operate at different temperatures, use different electrolytes and are specialized on different fuels. A very common nomenclature of fuel cell types is based on the respective electrolyte. Polymer electrolyte membrane fuel cells (PEMFCs) employ a proton conducting electrolyte, which operate at maximum 80 °C. PEMFCs are currently used in boats, submarines, military vehicles and personal cars. PEMFCs, however, are prone to CO poisoning, which strongly limits the usable fuels; mainly pure H_2 is used to run PEMFCs. A special type, which is similar to the PEMFC, is the direct methanol fuel cell (DMFC). Although having a reduced efficiency, the main advantage of DMFCs is that methanol is a liquid, thus providing easier storage and overall easier handling. Alkaline fuel cells use KOH as an electrolyte, operating at 60 °C - 120 °C. They were mainly used in astronautics. They also suffer from CO_2 poisoning and have reduced durability due to the corrosive electrolyte. Phosphoric acid fuel cells (PAFCs) are medium-temperature fuel cells, operating between 150 °C and 200 °C. They are used for stationary power generation as well as in buses. Fuel cells operating at high temperatures are molten carbonate fuel cells (MCFCs), which operate between 600 °C and 700 °C, and solid oxide fuel cells (SOFCs), which operate between 700 °C and 900 °C. They are both tolerant to CO or CO_2 [5].

Within the field of fuel cells, solid oxide fuel cells (SOFCs) are generally seen as a promising technology. A generalized model of galvanic cells and the inputs and outputs of SOFCs are shown in Figure 1.
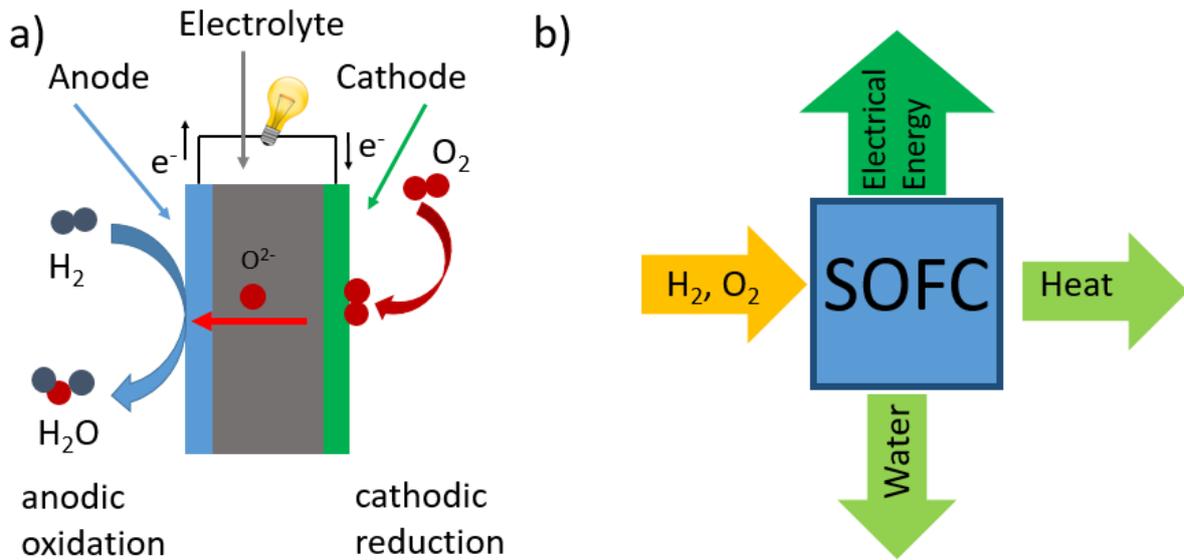
Figure 1: Electrochemical cells; a) a generalized model of an SOFC showing the integral parts of such electrochemical cells (anode, electrolyte, cathode) as well as the corresponding electrode reactions, namely the oxidation at the anode and the reduction at the cathode; ionic and electronic currents are shown as black and red arrows, respectively; b) input and output of a typical SOFC; typical inputs are H_2 as a fuel and O_2 as the oxidizing agent; the most important output is electrical energy, with water and heat as side products.

SOFCs operate on a large variety of fuels at temperatures between 700 °C and 900 °C and can be coupled with heating systems. While carbon monoxide leads to poisoning of the Pt electrode in PEMFCs, SOFCs are CO tolerant and – owing to their higher operating temperature - can actually use CO to produce power. Moreover, by using combined power and heating systems (CPH), the already high efficiencies of SOFCs can be improved even further. Mitsubishi Heavy Industries reported in 2011 to reach an efficiency of up to 70 % when combining a SOFC, a gas turbine and a steam turbine [6]. The SOFC is operated on natural gas and the exhaust gas is used in a gas turbine.

Bloom Energy reports a cumulative maximum efficiency of their energy servers of 60 % - 65 %, depending on the product series. The energy servers operate on natural gas or bio gas, thus demonstrating the flexibility in the choice of the fuel [7].

However, there are still problems concerning the use of SOFCs. On the cathode side, current research deals with Sr doped $LaCoO_{3-\delta}$ (LSC) and Sr doped $La(Co,Fe)O_{3-\delta}$ (LSCF) as a mixed ionic and electronic conducting electrode, which are the presently most active cathodes, but have

problems with long term stability. This optimization of SOFC cathode materials led to a decreased resistance of the cathode [8].

Optimization of the electrolyte, especially the use of thin film electrolytes, also led to a decreased resistance of the electrolyte [9-11].

For the anode a major problem is sulfur poisoning, which prevents the use of biogas as a fuel [12, 13]. Other problems concerning the Ni-based anode are the deposition of carbon when using hydrocarbons as a fuel, as well as the volume change when Ni is oxidized to NiO, which might lead to cracks in the electrolyte – a problem that becomes increasingly relevant since an increased performance of SOFCs can be achieved by thin film electrolytes [14-17].

Metal supported SOFCs (MSCs) are in the spotlight of current research, especially due to their application as auxiliary power unit (APU). While MSCs are robust and can be heated to the operating temperature fast, the anode cannot be prepared as in conventional SOFCs. MSC anodes are prepared by sintering metallic Ni/YSZ in reducing atmospheres, which leads to a higher anode resistance [18-20].

Due to the recent developments in regard to improving the performance of SOFCs by optimization of the cathode and the electrolyte, the reduction of the resistance of the anode is more and more important – a trend that is further enhanced by the increasing interest in MSCs.

Finding new anode materials is, therefore, essential to improve SOFCs. Many promising materials are perovskite type oxides. In contrast to the state-of-the-art Ni/YSZ anode, the main advantage of oxide anodes is their reduced volume change compared to Ni upon redox cycling [21]. Additionally, the use of ceramic electrodes may prevent the deposition of carbon[22-24]. A widely used cathode material is Sr-doped $LaMnO_{3-\delta}$ (LSM). However, LSM is unstable in reducing atmospheres and cannot be used as an anode consequently [25]. On the other hand, $LaCrO_{3-\delta}$ (LSCr) is stable in reducing atmospheres, but has a very low conductivity [25]. One possible approach is to investigate perovskite type oxides containing both Mn and Cr. The obtained material, $La_{1-x}Sr_xCr_{1-y}Mn_yO_{3-\delta}$ (LSCrM), possibly combines both their advantages, resulting in a material with high conductivity as well as stability under both oxidizing and reducing atmospheres. LSCrM also provides two possible ways of changing the electronic properties. The first one is the Sr-doping on the A-site, the second one is the Cr:Mn ratio on

the B-site. In order to find a suitable material, in the present work the Cr:Mn ratio was varied, keeping the amount of Sr-doping constant. In addition, the amount of Sr-doping was varied, keeping a fixed Cr-Mn ratio. The samples were investigated in humid hydrogen, demonstrating the necessary chemical stability during the measurement.

1.2 Strategy for controlling the defect chemistry of (La, Sr)(Cr, Mn)O$_{3-\delta}$

Both ways of changing the properties of La$_{1-x}$Sr$_x$Cr$_{1-y}$Mn$_y$O$_{3-\delta}$ are now described in more detail. The first one is the degree of acceptor-type strontium doping on the A-site of the perovskite. More Sr is expected to increase the amount of charge carriers, resulting in a higher conductivity:

$$SrO \rightarrow Sr'_{La} + O_O^x + h^\bullet$$

$$SrO \rightarrow Sr'_{La} + O_O^x + \frac{1}{2}V_O^{\bullet\bullet}$$
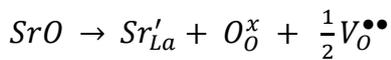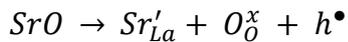
However, research shows that the amount of charge carries is, at least for higher Mn concentration, independent of the Sr dopant concentration [26].

The other parameter is the Cr:Mn ratio on the B-site of the perovskite lattice. Varying this ratio enables a fine tuning between chemical stability in reducing atmospheres and high conductivity. Due to the different chemical properties of Mn and Cr, a change of the predominant charge carrier (oxygen vacancies, electron holes) can occur, thus affecting the ionic and electronic conductivity of the material (see section 2.1 and Figure 2).

While current research usually reports on the results using one specific composition of LSCrM, there is also literature on the effect of varying the Cr:Mn ratio in LSCrM, investigating the conductivity for different compositions in regard to their respective Mn concentration [26]. However, in this study bulk samples were investigated only under oxidizing conditions.

1.3 Aim of the current work

Current research on LSCrM deals with:

- The use of certain LSCrM compositions as anodes, using hydrogen or hydrocarbons as fuels, e.g. [27].

- The use of individual LSCrM compositions in symmetrical SOFCs, e.g. [28].

- The fabrication of LSCrM composite materials, e.g. with Gd doped ceria (GDC), e.g. [29].

In this applied research, A-site deficient perovskites (ABO_3, see section 2.6) are often used for practical reasons, such as enhanced sintering behavior and increased stability towards the electrolyte [30, 31]. However, they are also prone to the formation of secondary phases [32]. In addition, usually porous electrodes are used. While porous electrodes are beneficial when operating a SOFC, porous electrodes are much harder to characterize, due to the often unknown geometry (e.g. unknown surface area).

Therefore, this work aims at providing a deeper understanding of the materials properties and possible ways of changing them. This work contributes to the field in the following ways:

- The conductivity of LSCrM thin films was investigated under both oxidizing and reducing conditions.

- A systematic study was carried out to investigate the dependency of the conductivity on the Sr doping concentration as well as on the Cr:Mn ratio. By systematically scanning different compositions, a much better overview over the materials properties can be given and materials with high conductivities can be identified. The effect of Sr doping and varying the Cr:Mn ratio can be separated and discussed individually, which results in a deeper understanding of how to improve the conductivity of the material.

- By using stoichiometric (i.e. not A-site deficient) materials, the formation of phase pure samples is easier. Therefore, the actual properties of the respective material are investigated and the results are not influenced by secondary phases (e.g. spinel phases).

- Electrochemical properties were obtained by means of electrochemical impedance spectroscopy on thin film model electrodes. Therefore, electrochemical data such as the electrode polarization resistance can be obtained. This information is essential when using a material as an electrode.

- The approach to use thin films on insulating substrates and thin film model electrodes on ion conducting YSZ substrates enables the collection of both electrical and electrochemical properties. The application of thin film model with well-defined geometry allowed the measurement of the area specific polarization resistance.

2 Theory

2.1 Defects in solids

While solids are generally viewed as a highly organized state of matter, considering the crystallinity, the periodicity and the unit cell, defects are of vital essence for understanding the electrical, as well as the mechanical, properties of a solid material. As an analogy, the autoprotolysis of water creates H^+ and OH^- ions that are essential for the conductivity of water. In this regard, the H+ can be seen as a defect at a site where it is not supposed to be in the ideal state, while OH^- is actually a missing H^+, or a H^+ vacancy. Another example of defects are electrons in the conduction band of a semiconductor or electron holes in the valence band of a semiconductor [33].

Different defects can be distinguished in solids: First of all, there are ionic and electronic point defects. Point defects are defects located on a single site, in contrast to higher dimensional defects which affect a line (1D), an area (2D) or a volume (3D). Electronic defects are electrons or electron holes. Examples for ionic point defects are vacancies and interstitials. For nomenclature of point defects, the Kröger-Vink notation is usually used, which for a generalized point defect reads [34]:

$$Particle\ (A)_{site\ (B)}^{relative\ charge\ (C)}\ .$$

Therein, *A* stands for the atom or ion, for vacancies the symbol *V* is used. *B* is the atom/ion, which occupies this site in case of an ideal crystal. When speaking of interstitial sites, the symbol *i* is used. The term C denotes the relative charge. The relative charge is defined as the real charge on this position minus the charge of the ideal crystal on this position. Dots show a positive relative charge, slashes a negative and *X* means that the point defect is relatively neutral. When speaking of an ideal material, the abbreviation *nil* is used to indicate that no defects are present.

Some examples of ionic point defects shall be given here:

$Ag_i^{\bullet}$ for a Ag⁺ ion on an interstitial site

$V_O^{\bullet\bullet}$ for an oxygen vacancy

Sr_{La}' for a Sr²⁺ ion on a La³⁺ site

Mn_{Cr}^X for a Mn³⁺ ion on a Cr³⁺ site

Generally speaking, the relative charge on one site is compensated for by other defects, e.g. doping ZrO₂ with Y³⁺ on the Zr⁴⁺ site (Y_{Zr}') also creates oxygen vacancies ($V_O^{\bullet\bullet}$) to keep the entire crystal uncharged. Due to the overall neutrality of the crystal, intrinsic defects in ionic ceramics only appear as paired defects and include the Schottky disorder (V_{cation}, V_{anion}), the Frenkel disorder (V_{cation}, $Cation_i$) and the anti-Frenkel disorder (V_{anion}, $Anion_i$). The example of doped ZrO₂ also highlights the importance of point defects when striving for functional materials. By doping ZrO₂ with Y³⁺ a material with a high ionic conductivity is obtained, which is used as an electrolyte in fuel cells.

Apart from ionic defects, also electronic defects, namely negatively charged electrons and positively charged electron holes, play an important role. In the Kröger-Vink notation, they are written as e' and $h^{\bullet}$. In analogy to the considerations above, electronic defects enable and enhance electronic conductivity. From a physical point of view, electrons in oxides can be seen as electrons in the conduction band (e.g. semiconductors). From a chemical point of view, it is probably a more intuitively accessible approach to attribute the respective charge to a cation. Thus, an electron hole localized on a Mn³⁺ site can be denoted as $Mn_{Mn^X}^{\bullet}$.

In ceramic materials, electronic and ionic defects are the charge carriers that enable the conduction of electric current. These charge carriers can be formed within the material (intrinsic charge carriers), thus increasing entropy of the system, or can be introduced into the material by doping (extrinsic charge carriers) [35].

Only at 0 K, the ideal crystal without defects could theoretically be observed. At higher temperatures, the increase of entropy leads to the formation of defects. At each temperature, there is an equilibrium concentration of intrinsic charge carriers. The formation of intrinsic charge carriers is strongly thermally activated. The higher the temperature, the higher is the concentration of intrinsic charge carriers, thus increasing the conductivity. The following reaction formulas show the formation of intrinsic defects:

$$nil \leftrightarrow h^\bullet + e'$$

$$nil \leftrightarrow V_O^{\bullet\bullet} + V_{cation}'' \text{ (Schottky disorder)}$$
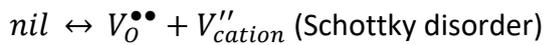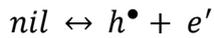
The formation of intrinsic charge carriers enables the conduction of electric or ionic current in an undoped material.

Extrinsic charge carriers are introduced to a material by doping. Foreign ions are introduced to lattice sites, leading to defects in the material. The concentration of extrinsic charge carriers is independent of the temperature. (Note: The conductivity, however, often increases with higher temperatures due to the increase in mobility.) These materials exhibit both good ionic and electronic conductivity [36, 37]. When doping, in principle both ionic and electronic defects can be introduced into a material. This issue shall be discussed using the examples of doping $LaMnO_3$ with Sr on the A-site of the perovskite. The divalent Sr on a three valent La site creates a negatively charged defect, the excess charge being compensated for by positively charged defects, which can either be electron holes or oxygen vacancies.

$$SrO \rightarrow Sr_{La}' + O_O^x + h^\bullet$$

$$SrO \rightarrow Sr_{La}' + O_O^x + \frac{1}{2}V_O^{\bullet\bullet}$$
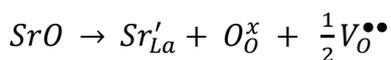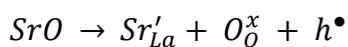
In this case, the possible electronic defect can be denoted as the oxidation of a cation, resulting in either La^{4+} or Mn^{4+}. While La strongly prefers the trivalent oxidation state, Mn can be found in many different oxidation states, including 4+. Due to the formation of electron holes in LSM and the resulting high electronic conductivity, this material is used as the state-of-the-art cathode in SOFCs due to its high electronic conductivity. However, also the formation of ionic defects, namely $V_O^{\bullet\bullet}$, can be observed in LSM, depending on the oxygen

partial pressures. At low oxygen partial pressures, oxygen vacancies are formed, while high oxygen partial pressure favour the formation of electron holes. The dependency of the defect concentration of ionic and electronic defects on the oxygen partial pressure can be seen in the so-called Brouwer diagram in Figure 2.
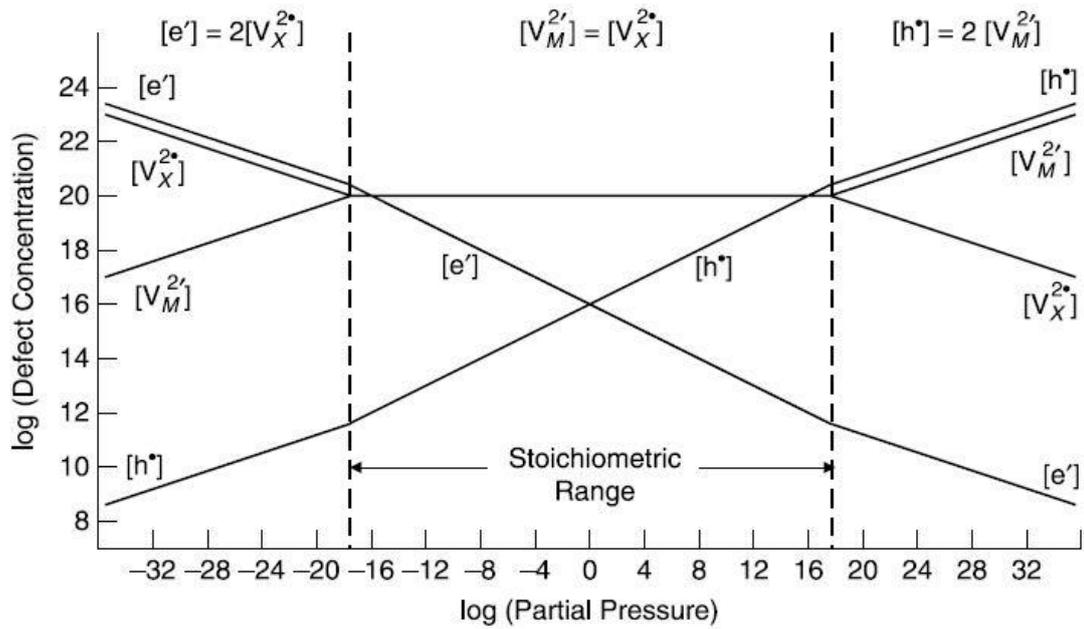
Figure 2: Brower diagram showing the concentration of defects vs. the oxygen partial pressure [35].

2.2 Conduction in solids

Electric conduction is the transport of charged particles. In general, the conductivity, i.e. the ability of a material to conduct electric currents, can be calculated by:

$$\sigma = z * F * u * c \qquad (2.1)$$

or $\sigma = z * e_0 * u * n$

with

$$F = e_0 * N_A \ \ and \ c = \frac{n}{N_A} \qquad (2.2)$$

with

z	Valency []
F	Faraday constant [C/mol]
u	Mobility [cm^2/s*V]
c	Concentration [mol/L]
n	Charge carrier density [1/L]
e_0	Elementary charge [C]
N_A	Avogadro constant [1/mol]

The above equations apply for different systems, such as aqueous solutions, semiconductors or ceramics. Only the type of charge carrier (ions solvated by water molecules, electrons, electron holes, oxygen vacancies, ...) differs. An oxygen vacancy as an example of ionic defects and its contribution to the conduction in a solid material is shown in Figure 3.
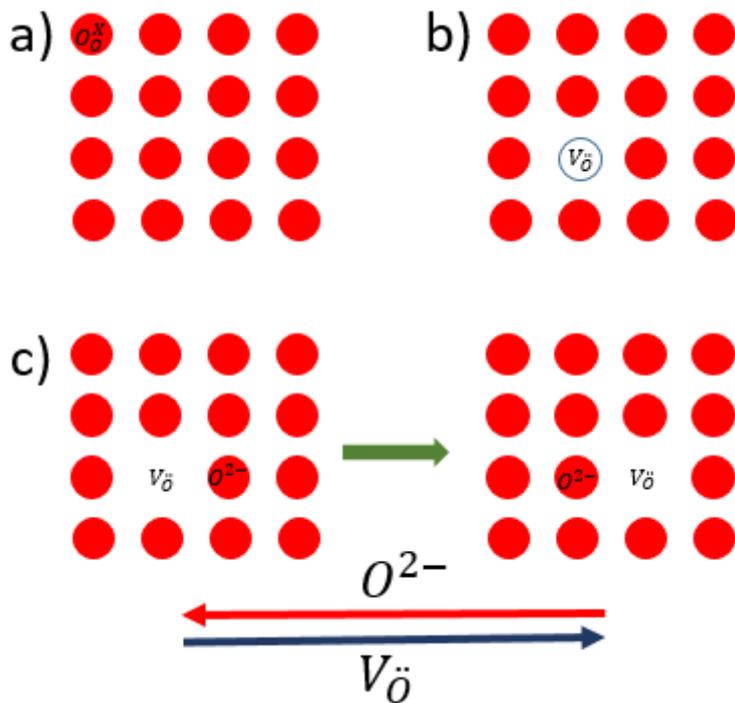
Figure 3: Oxygen vacancies as an example of ionic defects in solids; a) ideal crystal without defects; b) introduction of an oxygen vacancy to the material; c) conduction of oxygen vacancies; the movement of oxide ions can be denoted as the movement of oxygen vacancies in the opposite direction.

2.2.1 Polarons

Electronic defects, as discussed in section 2.1, can be localized at lattice sites. In LSCrM, an electron hole can be denoted as the oxidation of a Mn^{3+} ion ($Mn^{\bullet}_{Mn}x$). In ionic materials, an electron hole (or an electron) and the polarization induced on its surroundings together form a composite quasiparticle commonly referred to as a polaron. The degree of localization can vary. An electron hole and its surrounding lattice distortion is called small polaron, when the polarization is within the order of the lattice constant. The polarization of the surroundings of small polarons is then localized in the volume of one unit cell. Small polarons are transported in a material by thermally activated hopping. Typically, the activation energy for the conduction of small polarons is 0.5 eV. If the radius of the polaron is much higher than the lattice constant, it is referred to as large polaron (or Fröhlich polaron). In contrast to small

polarons, there is usually a band-like transport of large polarons. The activation energy is usually about 0.1 eV for large polarons. There is also evidence for the coexistence of small and large polarons in materials [38-42].

Figure 4 shows the introduction of an electron hole into an ideal crystal and the resulting polarization. In addition, a schematic representation of small and large polarons is given.
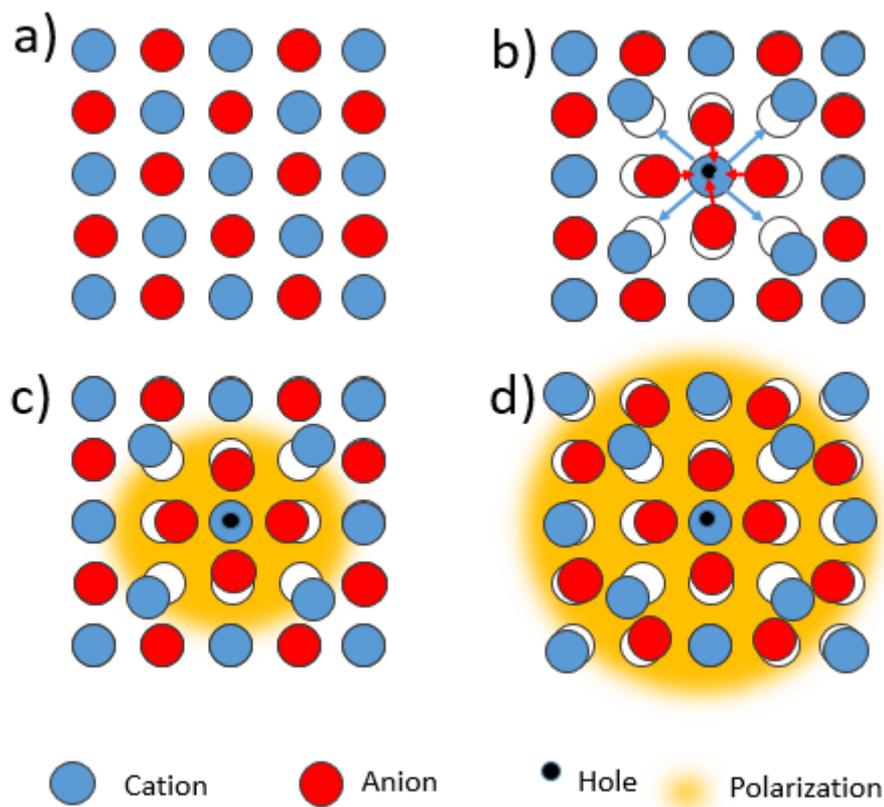
Figure 4: Polarons in solids; a) ideal ionic crystal without defects; b) introduction of an electron hole on a cation site; the respective positive charge leads to attraction of anions (red arrows) and to the repulsion of cations (blue arrows); this polarization of the surroundings of a localized electron hole due to the attraction and repulsion of ions is called a polaron; c) small polaron; the polarization is of the size of one unit cell; d) large polaron (or Fröhlich polaron); the polarized volume is much bigger than a unit cell.

2.2.2 Activation energy of the conductivity and Arrhenius plots

When chemical or physical processes are thermally activated, as found in 1889 by Svante Arrhenius for the rate constant of chemical reaction, the rate constant of a chemical reaction depends on the temperature by:

$$r = r_0\, e^{\frac{-E_A}{k_B T}}$$
(2.3)

With

| r | Rate constant [mol/s] |

E_A   Activation energy [eV]

r Rate constant [mol/s]

E_A Activation energy [eV]

k_B Bolzmann constant [eV/K]

T Absolute temperature [K]

In case of an elementary step of a reaction, the activation energy is the height of an energy barrier, which needs to be overcome in order for the reaction to proceed; a sketch of such an energy barrier is shown in Figure 5.
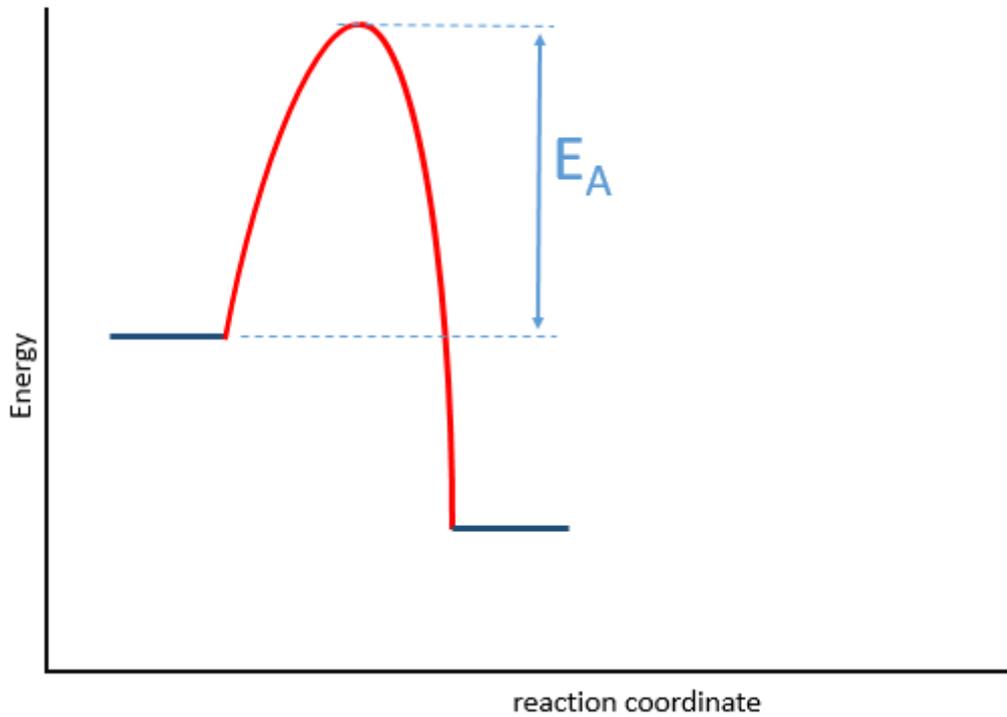
Figure 5: Activation energy for a chemical reaction; in order to reach an energetically lower state, an energy barrier has to be overcome.

A very similar picture is obtained for the long-range transport of localized charge carriers in solids. In order to move from one site to another, a charge carrier needs to overcome a certain hopping energy. The corresponding "energy landscape" is sketched in Figure 6.
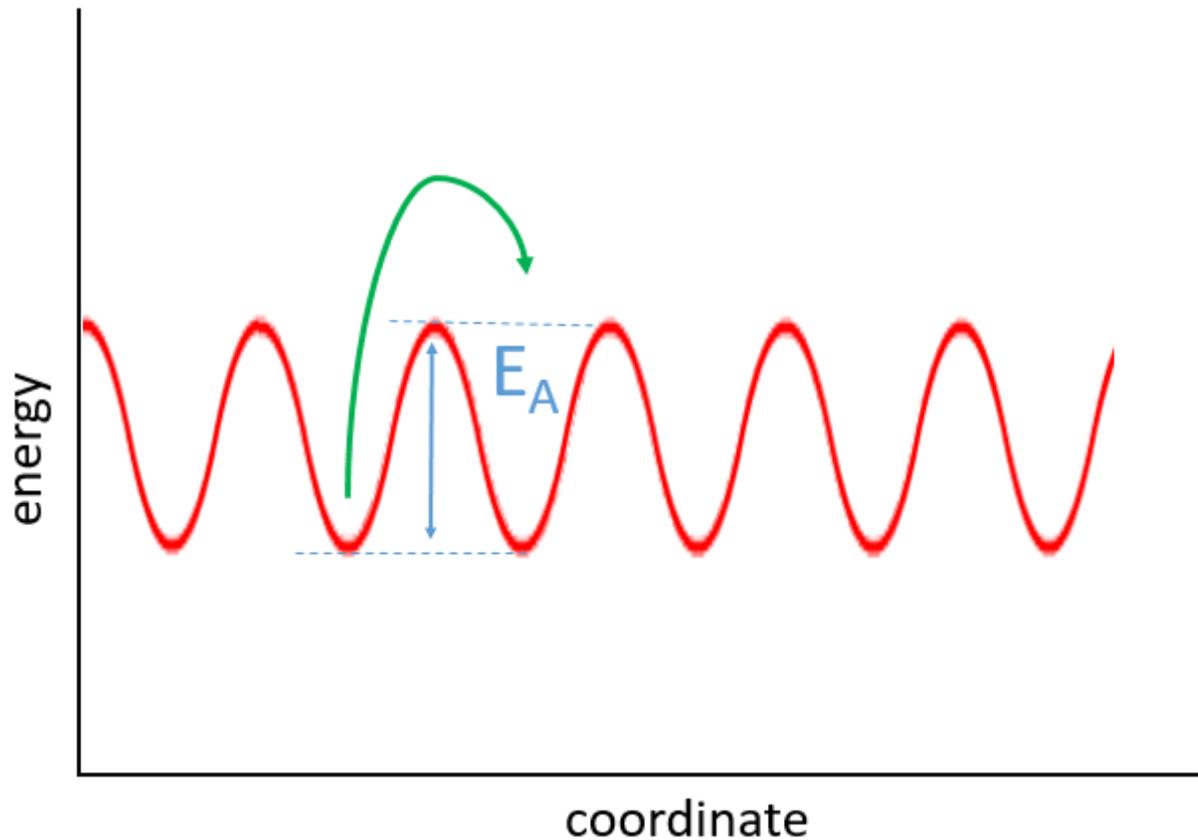
Figure 6: Energy vs. room coordinate; the energy shows minima and maxima; in order to move from one site to another, an energy barrier (E_A) has to be overcome.

Considering the Nernst-Einstein equation for the mobility of ions:

$$u = \frac{z*e_0*D}{k_B*T}$$
(2.4)

With

D   Diffusion coefficient [cm^2/s]

Combining the equations 2.3 and 2.4 yields the following equation, which also includes an exponential function:

$$\sigma = u*n*e_0 = \frac{z*n*e_0^2}{k_BT}*D = \frac{z*n*e_0^2}{k_BT}*D_0*e^{\frac{-E_A}{k_BT}} = \frac{A_T}{T}*e^{\frac{-E_A}{k_BT}}$$
(2.5)

With $A_T = \frac{z*n*e_0^2}{k_B}*D_0$ [S*K/cm]
(2.6)

An Arrhenius plot can be obtained as follows:

$$\sigma * T = A_T * e^{\frac{-E_A}{k_B T}}$$

(2.7)

Taking the logarithm yields:

$$ln(\sigma * T) = ln(A_T) - \frac{E_A}{k_B * T} = \frac{-E_A}{k_B} * \frac{1}{T} + ln(A_T)$$

(2.8)

This is basically a linear equation:

$$y = k * x + d \; with \; y = ln(\sigma * T); \; k = \frac{-E_A}{k_B}; \; x = \frac{1}{T}; \; d = ln(A_T)$$

(2.9)

When plotting $ln(\sigma * T)$ versus $\frac{1}{T}$, a straight line is obtained, as it can be seen in Figure 7. The activation energy can be calculated from the slope according to equation 2.9.
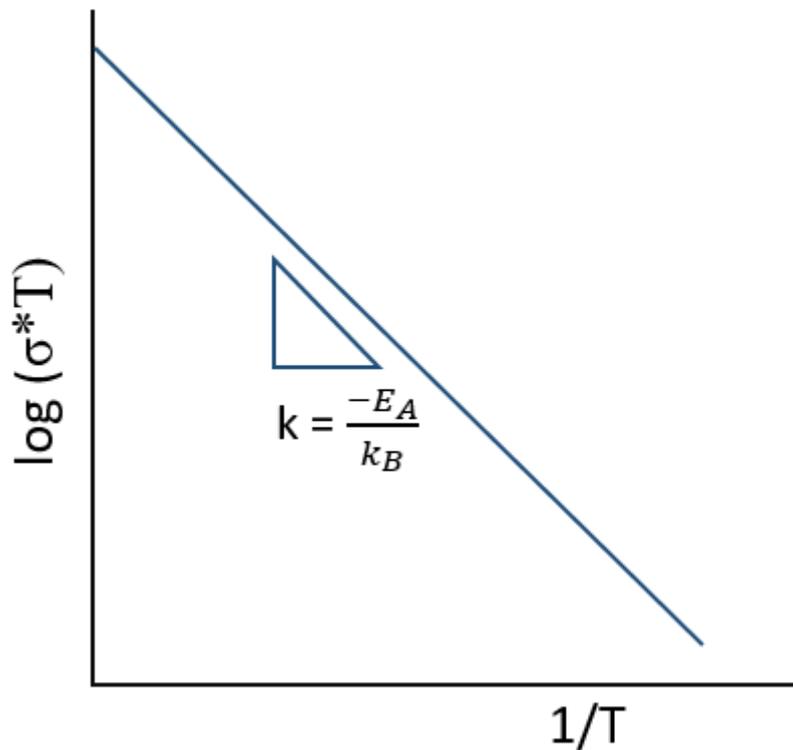
Figure 7: Schematic representation of an Arrhenius plot; the activation energy can be calculated from the slope.

2.3 Introduction to electrochemical cells

Electrochemical reactions involve the transfer of electrons in the course of a redox reaction. The formula below shows a generalized redox reaction:

$$A_{ox} + B_{red} \rightarrow A_{red} + B_{ox}$$
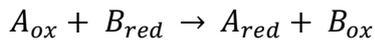
This reaction can now be split into two half-cell reactions.

$$A_{ox} + n\,e^- \rightarrow A_{red} \text{ (Reduction)}$$

$$B_{red} \rightarrow B_{ox} + n\,e^- \text{ (Oxidation)}$$
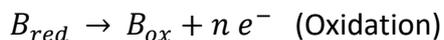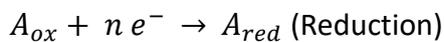
An example with practical relevance is the formation of water from its elements:

$$H_2 + \frac{1}{2}\,O_2 \rightarrow H_2O$$
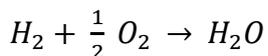
Splitting the oxyhydrogen reaction into the half-cell reactions yields the following formulas:

$$\frac{1}{2}\,O_2 + 2\,e^- \rightarrow O^{2-} \text{ (Reduction)}$$

$$H_2 + O^{2-} \rightarrow 2\,H_2O + 2\,e^- \text{ (Oxidation)}$$
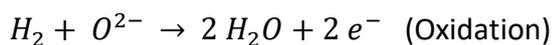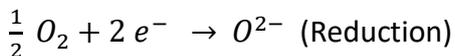
The number of electrons which are produced by one half-cell reaction are consumed by the other half-cell reaction.

In order to use the transferred electrons as an electric current, the half-cell reactions have to be separated locally: The oxidation takes place at the anode, the reduction at the cathode (see Figure 1.a). These are then connected by an external circuit, enabling the use of the electric current to power devices. The used reagents determine the obtained voltage.

If, however, the electrons as charge carriers moved only from one side to the other, this would lead to a charging and the difference in the electric potentials would eventually stop the reaction. Therefore, an electrolyte is needed. For example, the electrolyte can be a salt bridge

or a membrane which is permeable for certain ions. The ionic current compensates the electrical current.

A galvanic cell is an electrochemical cell that produces an electric current, such as fuel cells and batteries. A generalized example of a galvanic cell is shown in Figure 1.a.

In order to obtain the voltage of a galvanic cell, it is necessary to look at the reactions from a thermodynamic point of view. The reactions, like the formation of water, have to take place spontaneously, meaning:

$\Delta G < 0$ with

$$\Delta G = \Delta H - T * \Delta S \qquad\qquad (2.10)$$

with

ΔG Free enthalpy change [J/mol]

ΔH Enthalpy change [J/mol]

T   Absolute temperature [K]

ΔS Entropy change [J/mol*K]

The first principle of thermodynamics states the equivalence of chemical and electrical work (or energy) (see equation 2.13). Therefore:

$$W_{el} = Q * U = z * F * U_c \qquad\qquad (2.11)$$

$$W_{chem} = \Delta G = \Delta H - T * \Delta S \qquad\qquad (2.12)$$

with

W_{el} Electrical work [J/mol]

Q   Charge [C]

U   Voltage [V]

z   Valency []

F   Faraday constant [C/mol]

U_c Open circuit voltage voltage [V]

W_{chem} Chemical work [J/mol]

Due to their equivalence, it can be concluded:

$$W_{chem} = -W_{el} = \Delta G = -z * F * U_c$$ (2.13)

The open circuit voltage for a given chemical reaction is therefore given by:

$$U_c = \frac{-\Delta G}{z*F}$$ (2.14)

Depending on the chemical reaction, a different cell voltage is obtained. The theoretical voltage is easily accessible in the standard electrode potential series, which shows the potential for a given half-cell reaction, with hydrogen as the reference half-cell reaction having a defined potential of 0 V. Hydrogen and oxygen forming water has a theoretical cell voltage of 1.23 V. (Note: The standard electrode potential series does not list the potential of a half cell reaction, but the electrochemical potential of the electrons.)

2.4 Electrochemical energy conversion

The advantage of electrochemical energy conversion (e.g. fuel cells, batteries) is a higher efficiency than in conventional energy conversion (e.g. gas turbine, combustion engine). Figure 8 shows the difference between electrochemical and conventional energy conversion.
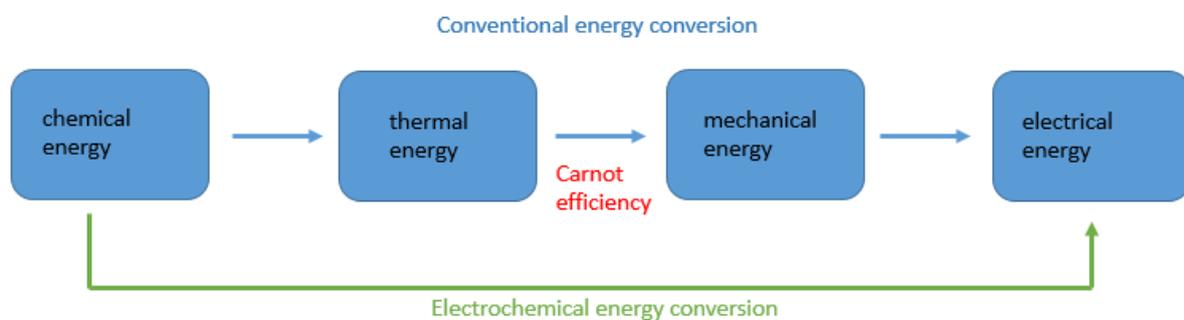
Figure 8: Conventional and electrochemical energy conversion; multiple intermediate steps in conventional energy conversion are in contrast to the single step in electrochemical energy conversion, thus resulting in higher efficiencies of electrochemical energy conversion.

The conventional energy conversion is based on the conversion of the chemical energy of a fuel (e.g. coal) into thermal energy by combustion. The resulting high temperatures are used to heat water which is vaporized. The thermal energy of the steam is converted into mechanical energy, by moving a turbine with the steam. The mechanical energy is converted to electrical energy by using a generator. The critical step is the conversion of thermal energy, to mechanical energy which is limited by the Carnot efficiency:

$$\omega_{carnot} = \frac{T_{hot} - T_{cold}}{T_{hot}} = 1 - \frac{T_{cold}}{T_{hot}} \qquad (2.15)$$

with

ω_{carnot} Carnot efficiency []

T_{hot} Highest Temperature within a process [K]

T_{cold} Lowest temperature within a process [K]

The Carnot efficiency is higher when T_{hot} is high and T_{cold} is low. An efficiency of 100 % cannot be reached, as neither 0 K for T_{cold} nor an infinitely high temperature for T_{hot} is physically possible.

The electrochemical energy conversion is not limited by the Carnot efficiency and takes place in one step, thus potentially reducing the losses.

The theoretical efficiency of an electrochemical process is given by:

$$\omega_{el.chem._{th}} = \frac{\Delta G}{\Delta H} = \frac{\Delta H - T\Delta S}{\Delta H} = 1 - \frac{T\Delta S}{\Delta H} \qquad (2.16)$$

with

$\omega_{el.chem._{th}}$ theoretical efficiency of an electrochemical process []

With ΔG being negative and ΔH being negative as well, efficiencies exceeding 100 % can be reached due to this definition, when ΔS is positive. In this case, the energy is taken from the surroundings.

The application of equation 2.16 shall be illustrated, using the example of the formation of water. For

$T = 0$

the theoretical efficiency for the fuel cell (see equation 2.16) yields

$$\omega_{el.chem.,th} = \frac{\Delta G}{\Delta H} = \frac{\Delta H - 0\Delta S}{\Delta H} = 1$$

The slope of the function is given by $\frac{-\Delta S}{\Delta H}$, which is positive if ΔS is positive, since ΔH is negative for the typical fuel cell reactions.

Figure 9 shows the theoretical efficiency of fuel cells and the Carnot efficiency.
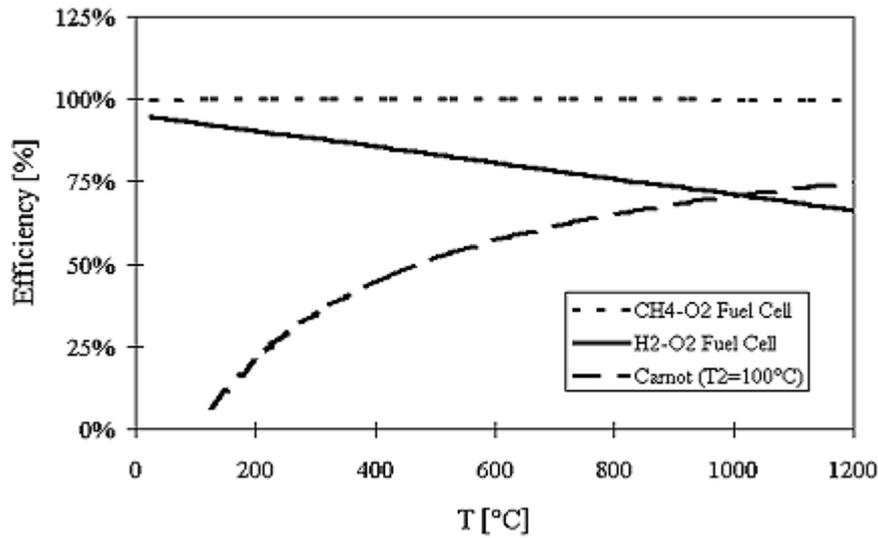
Figure 9: Dependency of the theoretical efficiency on the temperature for fuel cells and the Carnot cycle [43].

The reaction for the formation of water, however, has a negative entropy, which can easily be seen in the reaction equation, since one mole of gas molecules (H_2O) is formed out of 1.5 moles:

$$H_2 + \frac{1}{2} O_2 \rightarrow H_2O$$
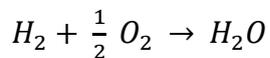
An advantage of solid oxide fuel cells is that they can be operated with various fuels, including methane, hydrogen, methanol, diesel reformate and others. The choice of fuel also means that there are different thermodynamic aspects for each reaction. While the thermodynamic efficiency of the hydrogen fuel cell decreases with higher temperatures, the decrease in efficiency for the methane fuel cell is barely perceptible. The reason for this difference is the different change in entropy. The reaction of the combustion of methane reads as follows:

$$CH_4 + 2\,O_2 \rightarrow CO_2 + 2H_2O$$
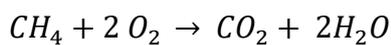
The number of gas molecules remains the same. It can be assumed that the change in entropy is therefore rather small. The thermodynamic data proves this point as the actual change in entropy ΔS is -7.1 J/K [44]. (Note: The above considerations only apply for the direct use of methane as a fuel. In real SOFC applications, methane is reformed and the actual fuel is again hydrogen.)

Even though Figure 9 suggests operating an SOFC at low temperatures (e.g. for H_2 as a fuel), usually kinetic aspects favor higher temperatures. While the decrease in efficiency is true for the theoretical efficiency, there is actually an optimum in the total efficiency at higher temperatures. At higher temperatures the ohmic losses in the electrolyte are smaller and the electrode kinetics are faster. Fuel cells couple the generation of electrical current I with a chemical reaction rate r.

$$I \sim r \; with \; r = r_0 e^{\frac{-E_A}{k_B T}}$$ (2.17)

with

I   Electrical current [A]

Apart from the faster kinetics at the electrodes at higher temperature, the ionic conductivity of the ceramic electrolyte also increases with temperature. Speaking from a kinetic point of view, higher temperatures increase the reaction rate, thus increasing the electrical current. The kinetic efficiency increases therefore with temperature. The total efficiency is:

$$\omega_{total} = \omega_{th} * \omega_{kin} * \omega_{gas} * \omega_r$$ (2.18)

with

ω_{total} total efficiency []

ω_{th} theoretical efficiency []

ω_{kin} kinetic efficiency []

ω_{gas} efficiency for the gas usage []

ω_r efficiency for all remaining processes []

Figure 10 shows the theoretical, the kinetic and the total efficiency of an SOFC. The theoretical efficiency decreases with temperature, while the kinetic efficiency increases with temperature. Therefore, a maximum in total efficiency is observed.
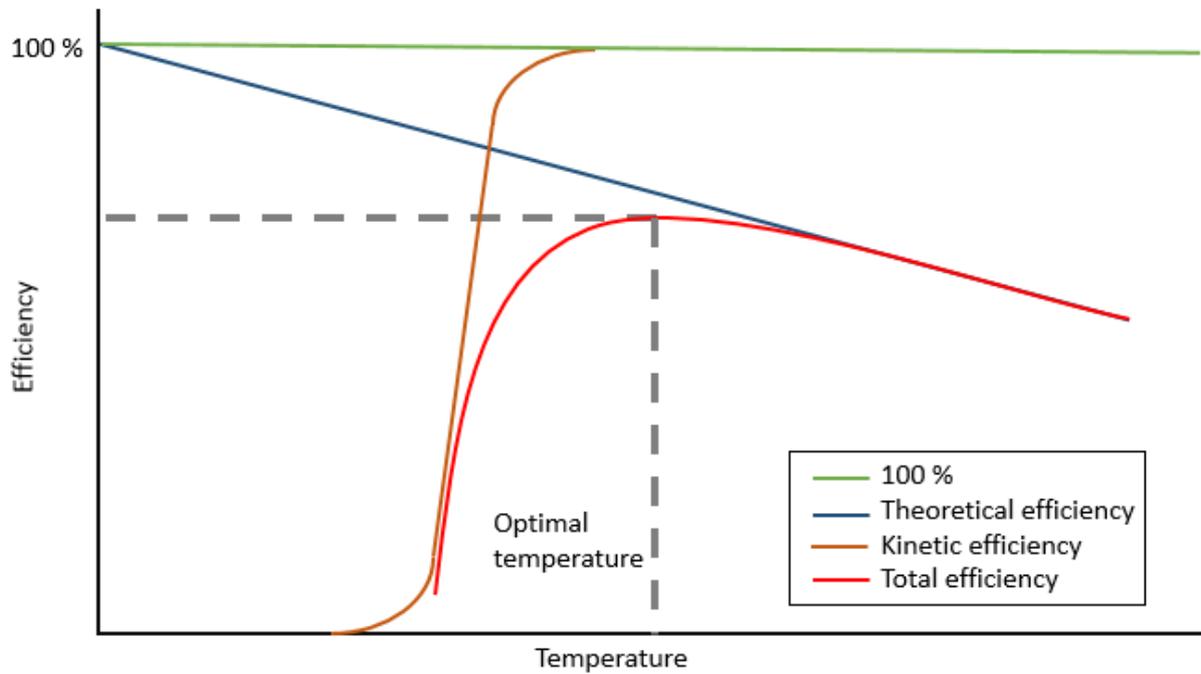
Figure 10: Schematic representation of theoretical and kinetic efficiency of SOFC resulting in a maximum in the total efficiency at higher temperatures.

The total efficiency is lower than the theoretical efficiency, due to losses which can occur in every conversion step. Electrochemical energy conversion could therefore reach higher efficiencies than conventional energy conversion, which requires multiple steps, since energy is potentially lost at every step.

2.5 Solid oxide fuel cells

Solid oxide fuel cells (SOFCs) are a high-temperature type of fuel cells. As for all galvanic cells, SOFCs consist of two electrodes as well as an electrolyte. For SOFC applications, where higher voltages are needed, the individual SOFCs can be stacked in series. In this case, an interconnect material (e.g. Sr-doped $LaCrO_3$, nickel- or steel-based alloys, …) between the anode of one cell and the cathode of another cell is needed [45, 46].

The electrolyte most commonly used is yttria-stabilized zirconia (YSZ). The electrolyte should have a very high ionic conductivity, but a very low electronic conductivity to prevent internal short circuiting.

The electrodes should ideally be both, a good ionic and electronic conductor. The ionic conductivity is needed for better electrode kinetics, eventually opening up the bulk path (see Figure 12) Other important requirements for electrodes in SOFCs include thermochemical stability, stability under different oxygen partial pressures and a high catalytic activity towards the respective reaction [47].

A schematic representation of an SOFC is shown in Figure 11.
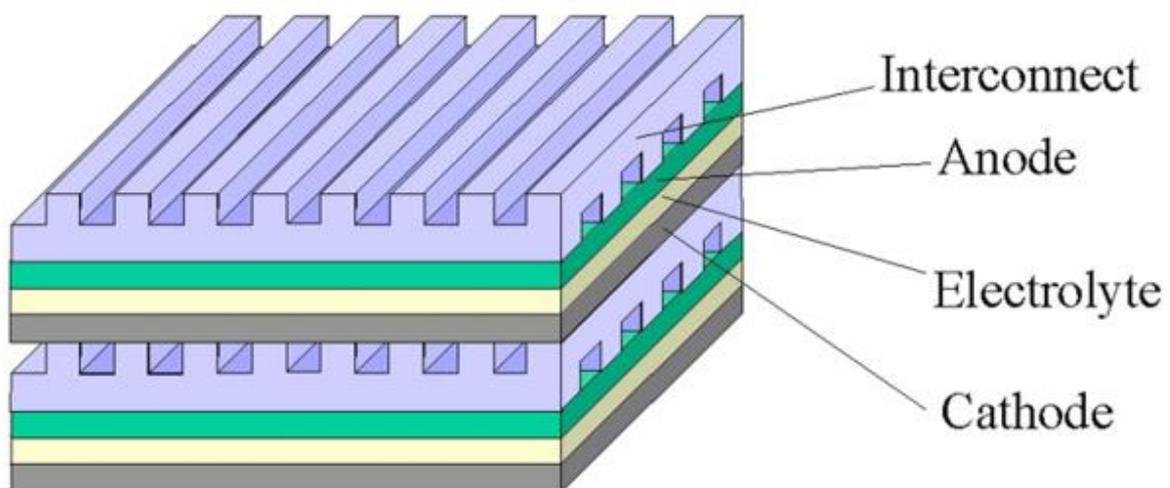
Figure 11: Generalized structure of SOFCs; stacking of SOFCs to obtain a higher voltage; between the individual SOFCs there is the interconnect layer [48].

While Ni/YSZ anodes, which are most commonly used, offer high catalytic activity for H_2 oxidation and high electrical conductivity, it also exhibits some problems including sulfur poisoning, chromium poisoning, carbon deposition, sintering and redox-cycling stability [47, 49].

Materials used as cathodes, which meet the requirements for SOFC electrodes, are often perovskites such as strontium doped $LaMnO_3$ (LSM) [45] as well as $(La,Sr)(Co,Fe)O_{3-\delta}$ (LSCF) [50].

The reduction of oxygen leads to negatively charged oxygen ions which are transferred through the electrolyte. There are two possible ways of incorporating oxygen – the surface path and the bulk path [51, 52] . These are shown in Figure 12.

The first one to be explained in detail is the surface path, which means that the oxygen is absorbed and dissociated on the surface of an electrode particle and then diffuses to the three phase boundary (i.e. the region where electrode, electrolyte and gas phase meet). At the triple phase boundary (TPB), the ionization of the adsorbed oxygen takes place and the formed oxide ion is incorporated into the electrolyte. Electrode materials with low ionic conductivity follow this mechanism. An example for a material predominantly governed by this path is LSM as well as Pt.

The second possible way is the incorporation via the bulk of the electrode. The oxygen is again absorbed on the surface and dissociated, but the reduction of oxygen occurs on the electrode surface. The resulting oxide ion is incorporated into the electrode and travels through the electrode bulk to the electrolyte. As a result, the whole area of the electrode is active, not only the three phase boundary. Therefore, electrode materials which follow the bulk path can increase the performance of the fuel cell. These materials have to be mixed ionic and electronic conductors (MIECs), providing both a good electronic and ionic conductivity. An example is Sr doped $LaCoO_3$ (LSC).
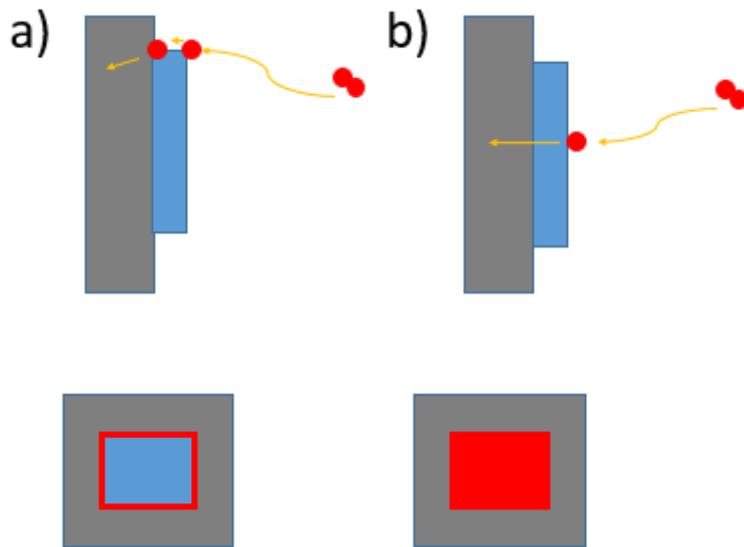
Figure 12: Different paths for the oxygen reduction reaction in SOFC cathodes; the electrode is shown in blue, the YSZ in grey, the active area for the oxygen reduction reduction reaction is highlighted in red; a) a tripple phase boundary active material; b) a surface path active material.

While there have been attempts to use MIECs as SOFC cathodes, such as LSC and LSCF, the Ni/YSZ anode is triple phase boundary active. The electronic conductivity comes from the Ni while the ionic conductivity comes from the YSZ. When using Gd doped CeO_2 instead of YSZ, the electronic conductivity of Gd doped CeO_2 is sufficient to activate the CeO_2 surface for the hydrogen oxidation, thus opening the bulk path for H_2 oxidation [53, 54]. Different composite anode materials, state-of-the-art materials as well as possible materials for future applications, are compared in Table 1. In the future, new anode materials might help to improve anode performance.

Table 1: Electronic and ionic conductors in SOFC anode materials and the area expectedly active for the oxidation of H_2.

	σ_{ion} **provided by**		
σ_{eon} **provided by**	*YSZ*	*GDC*	*LSCrM*
Ni	TPB	GDC surface	LSCrM surface
LSCrM	LSCrM surface (+ TPB)	both surfaces	LSCrM surface

2.6 $La_{1-x}Sr_xCr_{1-y}Mn_yO_{3-\delta}$ (LSCrM) anodes in SOFCs

Perovskite-type oxides are materials with the same crystal structure as $CaTiO_3$. The chemical formula of perovskites can be generalized as ABO_3, where A (e.g. Ca^{2+}, Ba^{2+}, ...) and B (e.g. Ti^{4+}, ...) are large and small cations, respectively. The coordination number in regard to oxygen ions for the A site is 12 and for the B site is 6. The unit cell of a perovskite is shown in Figure 13. There is a wide variety of cation combinations that form perovskite structures with different properties. As an example, there are perovskites involving cations A and B with a charge of +3 each, such as $LaMnO_3$ and $LaCrO_3$, including the ions La^{3+}, Mn^{3+} and Cr^{3+}, respectively.
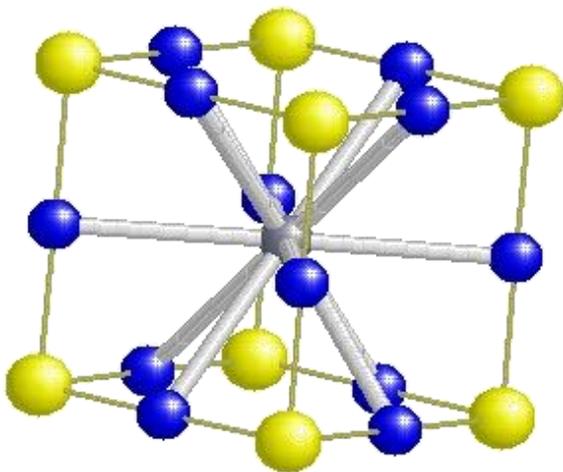
Figure 13: Perovskite structure; Grey: A-site; Yellow: B-site; Blue: oxygen [55].

Owing to this compositional diversity, perovskites demonstrate a large variety of interesting properties including electronic conductivity, ionic conductivity, catalytic activity and magnetism [56].

Moreover, these properties can be tuned by doping, i.e. by introducing different cations on the A or B site, which yields the mixed perovskites $(A^1, A^2)BO_3$ or $A(B^1, B^2)O_3$.

Very often alkaline earth metals are used as acceptor-type dopants on the A-site. The effect of e.g. Sr doping on the A-site is the introduction of electron holes and/or oxygen vacancies in the material, thus increasing the total conductivity. However, higher amounts of Sr tend to destabilize the perovskite. On the B-site a large number of transition metals can be used as dopant owing to their similar ionic radii. As an example, Cr in $LaCrO_3$ can be substituted with other transition metals. The introduction of Mn on the B-site of $LaCrO_3$ improves the catalytic activity and ionic conductivity. On the other hand, the introduction of Cr on the B-site of $LaMnO_3$ improves the stability under reducing atmospheres. [57]

Finally, also doping on both sites is possible – e.g. different compositions of $La_{1-x}Sr_xCr_{1-y}Mn_yO_{3-\delta}$ have been reported in literature. Due to its stability under reducing conditions [57] and relatively high electronic conductivity, LSCrM is a potential SOFC anode material. Different LSCrM compositions have successfully been used as anodes, not only with hydrogen as fuel, but also with hydrocarbons [27, 58, 59]. LSCrM/GDC composite anode were developed for direct oxidation of methane, showing that LSCrM/GDC provides good stability in CH_4 fuel and exhibits good electrochemical performance, which is comparable to Ni/YSZ anodes [60].

In order to use a material as an anode, an electrical conductivity of at least 1 S/cm is required [47, 61]. The electrical conductivity of the A site deficient perovskite $(La_{0.75}Sr_{0.25})_{1-x}Cr_{0.5}Mn_{0.5}O_{3-\delta}$ ($0 < x < 0.1$) is 38.6 S/cm in air and 1.49 S/cm in dry hydrogen at 900 °C [61].

The electronic conductivity of $(La_{0.75}Sr_{0.25})_{0.95}Cr_{0.5}Mn_{0.5}O_{3-\delta}$ in the temperature range between 750 °C and 1000 °C is between 20 S/cm and 35 S/cm in oxidizing conditions. Reducing below oxygen partial pressures of 10^{-12} to 10^{-16} atm increases the amount of oxygen vacancies and thus the ionic conductivity, but the total conductivity was found to be between 1 S/cm and 3 S/cm [62].

Therefore, the requirements for the use of a material as an electrode are met.

The reason for these strongly varying conductivity values in oxidizing and reducing atmospheres can be understood by the $p(O_2)$-dependence of the material's defect chemistry (cf. Figure 2). The perovskite-type oxide and the surrounding atmosphere are in equilibrium via:

$$O_O^x \leftrightarrow \frac{1}{2} O_2 + V_O^{\bullet\bullet} + 2\,e'$$
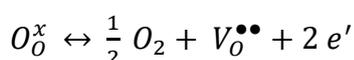
Since electrons and holes recombine ($h^\bullet + e' \leftrightarrow nil$), this reaction is equivalent to

$$O_O^x + 2h^\bullet \leftrightarrow \frac{1}{2} O_2 + V_O^{\bullet\bullet}.$$
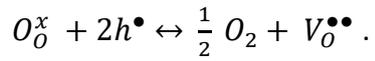
Upon reduction of the surrounding p(O_2), electron holes are consumed, thus decreasing the p-type conductivity.

On a side note, it should be mentioned that LSCrM can also be used as cathodes. Therefore, many successful attempts have been made to produce symmetrical SOFCs, i.e. using LSCrM as both cathode and as anode material [28, 63-67].

2.7 Van-der-Pauw method

The Van-der-Pauw method can be used to measure the specific resistance or the specific conductivity of a plane parallel sample [68, 69]. Van-der-Pauw's theorem is applicable for samples with a uniform thickness and infinitely small contact points placed on the very edges of the sample. Van der Pauw started his derivation using four points (A, B, C, D) on a straight line, then demonstrating by conformal mapping that his theorem is valid for a randomly formed sample, including square samples like the ones used in this work. The measurement setup is shown in Figure 14.
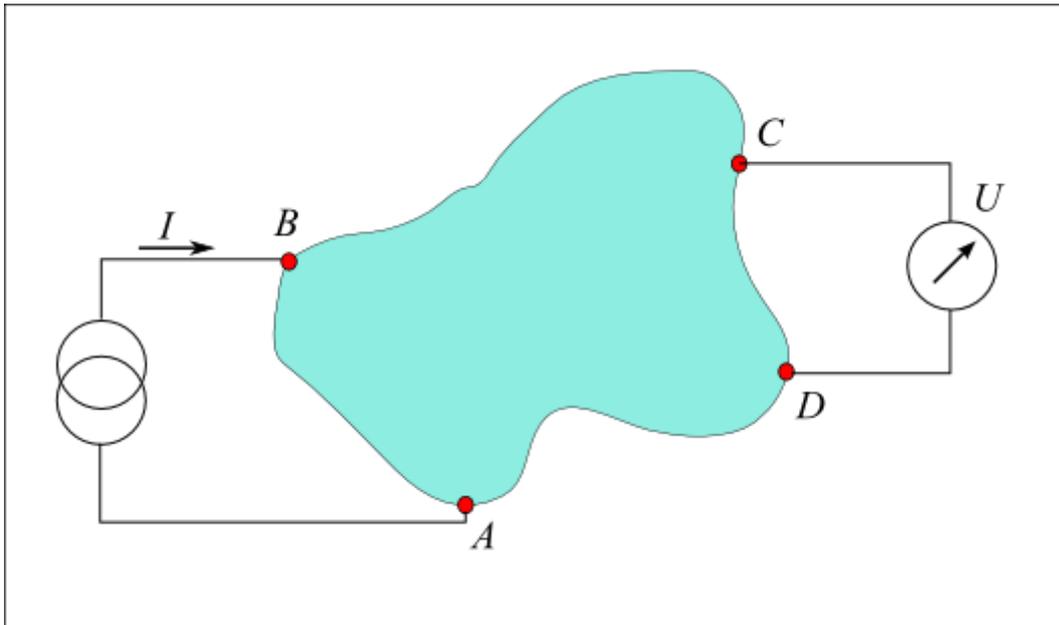
Figure 14: Generalized principle of the Van-der-Pauw method [70].

A voltage is applied between C and D and a corresponding current is measured between A and D. In this setup, $R_{AB,CD}$ is obtained, by a rotating switching of the contacts (i.e. voltage between B and C, current between D and A), $R_{BC,DA}$ is obtained.

Van-der-Pauw's theorem reads as follows:

$$e^{\frac{-\pi*d}{\rho}} * R_{AB,CD} + e^{\frac{-\pi*d}{\rho}} * R_{BC,DA} = 1 \qquad (2.19)$$

With

d   Thickness of the thin film [m]

ρ Specific resistance [Ωm]

$R_{AB,CD}$ Resistance (current measured between A and B applying a voltage between C and D; see Figure 14) [Ω]

$R_{BC,DA}$ Resistance (current measured between B and C applying a voltage between D and A; see Figure 14) [Ω]

The specific resistance can then be calculated as

$$\rho = \frac{\pi*d}{ln(2)} * \frac{R_{AB,CD} + R_{BC,DA}}{2} * f \qquad (2.20)$$

With the geometric factor f

$$f \approx 1 - \left(\frac{R_{AB,CD} - R_{BC,DA}}{R_{AB,CD} + R_{BC,DA}}\right)^2 * \frac{ln(2)}{2} - \left(\frac{R_{AB,CD} - R_{BC,DA}}{R_{AB,CD} + R_{BC,DA}}\right)^4 * \left(\frac{ln(2)^2}{4} - \frac{ln(2)^3}{12}\right) \qquad (2.21)$$

2.8 Electrochemical Impedance Spectroscopy (EIS)

When applying AC voltage to a sample, two types of current can occur:

There can be motion of free charge carriers within the material, commonly referred to as Faradayic current. The resistance in this case can be calculated using the geometric dimensions and the conductivity σ.

$$Z = R \; with \; R = \frac{1}{\sigma} * \frac{l}{A} \; for \; an \; ohmic \; resistance \qquad (2.22)$$

With

Z	Impedance [Ω]
R	Resistance [Ω]
σ	Conductivity [S/m]
l	Length of the sample [m]
A	Area [m²]

The second possibility is a charge transport via a displacement current. In physical materials such a transient current is usually due to dielectric polarization. The dielectric, or capacitive, properties of the material thus cause an impedance. The capacitance in this case can be calculated using the permittivity ε.

$$Z = \frac{1}{i\omega C} \; with \; C = \; \varepsilon * \frac{A}{l} \qquad (2.23)$$

With

ω	Frequency [Hz]
C	Capacitance [F]
ε	Permittivity [F/m]

Since real materials usually exhibit both conductive and dielectric behavior, a material can in the simplest case be described by a parallel connection of a resistor and a capacitor (cf. Figure 15).
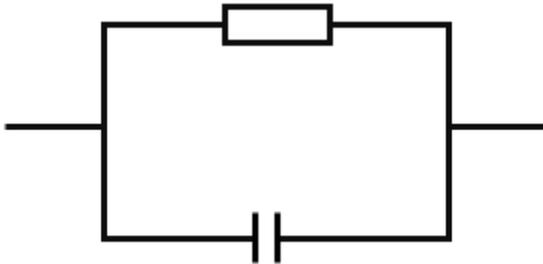
Figure 15: Resistor-capacitor circuit.

The impedance Z is then composed of these two parts, Z_R and Z_C.

Using a parallel connection of equations 2.22 and 2.23 yields:

$$Z = \frac{R}{1+i\,\omega\,R\,C} \quad \text{with } Z = \sum_i \frac{1}{Z_i} \tag{2.24}$$

When measuring the impedance of a material, the impedance is measured at different frequencies. At very low frequencies, or even in the extreme case of DC voltage, the current has to take the path via the ohmic resistor. At higher frequencies, the capacitive pathway gets more and more important, and a higher and higher current flows via the capacitor. When plotting the imaginary part of the impedance versus the real part of the impedance, called a Nyquist plot, a semicircle is obtained (see Figure 16).

42
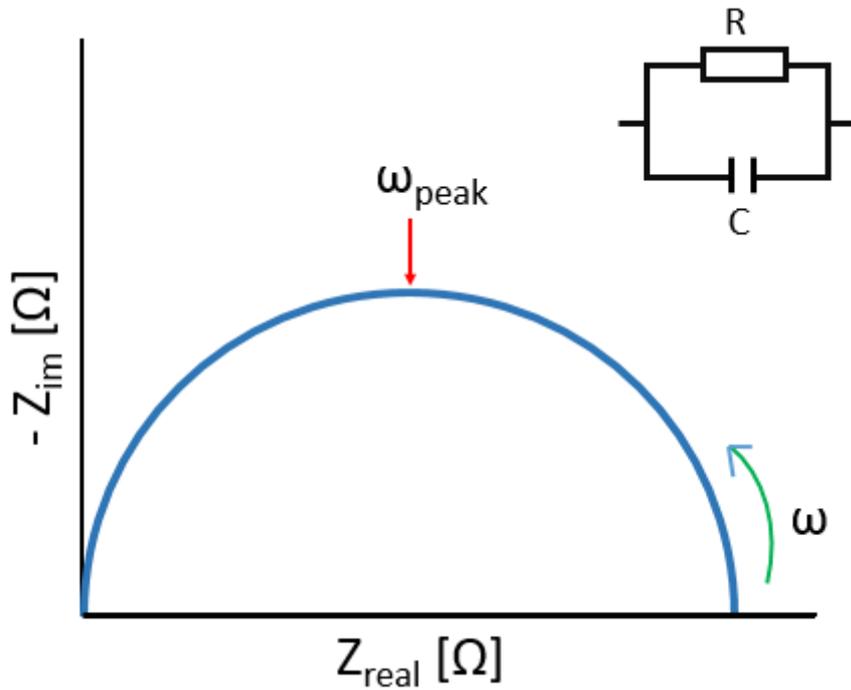
Figure 16: Nyquist plot for a resistor-capacitor circuit.

The frequency at which $|Z_{Real}| = |Z_{Im}|$ is called peak frequency ω_P. The peak frequency can be calculated by:

$$\omega_P = \frac{1}{RC} \qquad (2.25)$$

With

ω_P Peak frequency [Hz]

Combining equations 2.22, 2.23 and 2.25 yields:

$$\omega_P = \frac{1}{RC} = \frac{1}{\frac{1}{\sigma}*\frac{l}{A}*\varepsilon*\frac{A}{l}} = \frac{\sigma}{\varepsilon}$$

The peak frequency only depends on the material properties σ and ε and can therefore be used to differentiate between different materials.

Mixed ionic and electronic conductors (MIECs) with limited surface incorporation are of practical relevance to this work. Such electrode materials can be described by the equivalent circuit in Figure 17. R$_{YSZ}$ is the resistance of the YSZ electrolyte, R$_{INT}$ is the resistance of the

interface. The resistance of the surface incorporation is R_{INC}. The double layer capacitance is C_{DL}. C_{CHEM} is the chemical capacitance.
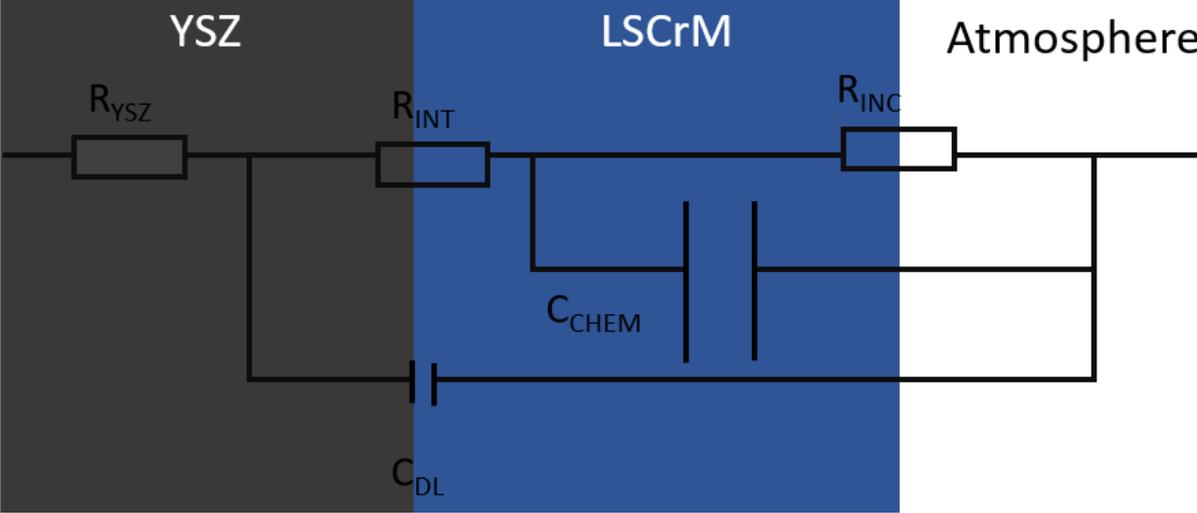
Figure 17: Equivalent circuit for a MIEC with surface limitation.

2.9 Pulsed Laser Deposition (PLD)

Pulsed laser deposition, a physical vapor deposition technique, uses a laser beam to strike a target in an evacuated chamber. The target material is vaporized rather homogeneously due to the high local energy. The ablated material is deposited on a heated substrate (e.g. YSZ, MgO, …). By varying the substrate temperature, the oxygen partial pressure and the pulse rate, the properties of the thin film can be changed. An advantage of this technique is that, under certain conditions, the stoichiometry can be transferred from the target to the thin film. The principle and a PLD device are shown in Figure 18.
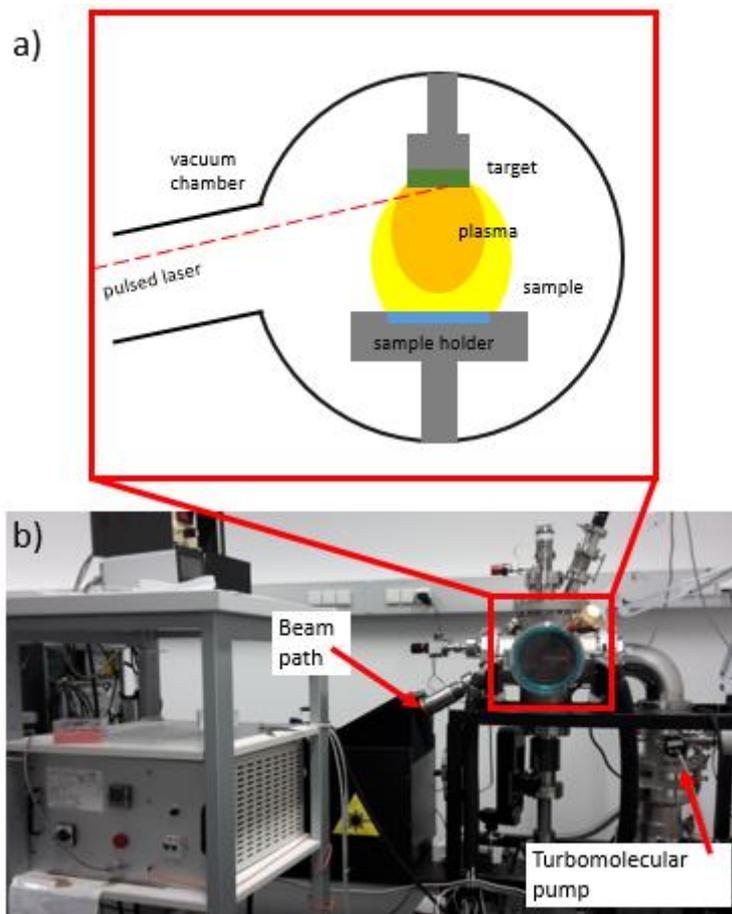
Figure 18: PLD device; a) schematic representation; b) device used in this work.

.

3 Experimental

3.1 List of used materials

Materials used in this work are shown in Table 2.

Table 2: Materials used in this work and a detailed description of them.

Material	Description
Photoresist	ma-N 1420 Negativ Photoresist (Micro Resist Technology GmbH, GER)
Developer	ma-D 533S Developer for Photoresis (Micro Resist Technology GmbH, GER)
YSZ (100)	ZrO_2:Y (100)K (9.5 mol% Y_2O_3) single sided polished, single crystal, 10x10x0.5 mm (Crystec, GER)
MgO (100)	MgO (100)K single sided polished, single crystal, 10x10x0.5 mm (Crystec, GER)
Al_2O_3 (0001)	Al_2O_3 (0001)K single sided polished, single crystal, 10x10x0.5 mm (Crystec, GER)
$LaAlO_3$ (100)	$LaAlO_3$ (100)K single sided polished, single crystal, 10x10x0.5 mm (Crystec, GER)
Reagents for Pechini synthesis	La_2O_3 (99.99 %, Sigma Aldrich, USA) $SrCO_3$ (99.995 %, Sigma Aldrich, USA) $MnCO_3$ (99.985 %, Alpha Aesar, USA) $Cr(NO_3)_3$x9H_2O (99.99 %, Alpha Aesar, USA) Citric acid monohydrate (99.9998 %, Sigma Aldrich, USA) Nitric acid (99.999 %, Sigma Aldrich, USA)

3.2 List of used devices

The devices used in this work are shown in Table 3.

Table 3: Devices used in this work and a detailed description of them.

Device	Description
PLD laser	KrF (248 nm) excimer laser (Lambda COMPexPro 205F
Pyrometer	Heitronics KT19.99
CIP	KIP-PK Ø25 (Paul-Otto Weber Maschinen- und Apparatebau GmbH, GER)
Sintering furnace	CWF1300 (Carbolite, GER)
Spincoater	Delta6RCTT (SUSS MicroTec, GER)
UV lamp	350W high pressure Hg lamp, maximum intensity 365nm (Ushio Inc., JAP)
Sputter machine	MED020 Coating system, QSG100 Quartz Film Thickness Monitor (BAL-TEC, now Leica Microsystems, AT)
EIS measurement device	Alpha-A High Performance Frequency Analyzer & Electrochemical Test Station POT/GAL 30V/2A (Novocontrol Technologies, GER)
SMU	2611 System Source Meter (Keithley Instruments Inc., GER)
SEM	Quanta 200 FEG (FEI, USA)
Furnace (Micro-Macro setup)	SR 70-200/12SO (Gero GmbH, GER)
Van-der-Pauw measurement device	SMU 2410 (Keithley Instruments Inc., GER) DMM 2000 (Keithley Instruments Inc., GER) – for the thermocouple DMM 2000 (Keithley Instruments Inc., GER) – for 4-wire measurements SR 70-200/12SO (Gero GmbH, GER)

3.3 Powder synthesis via a modified Pechini method and sample preparation

The used powders were La_2O_3, $SrCO_3$, $MnCO_3$ and $Cr(NO_3)_3 x9H_2O$. The desired amounts of educts were weighed out. Each compound was dissolved in water and/or concentrated HNO_3. Chromium nitrate was dissolved in water, while lanthanum oxide and strontium carbonate was dissolved in water containing a few drops of concentrated HNO_3. Manganese carbonate does not dissolve in water and, by adding too much concentrated HNO_3, the manganese is oxidized to manganese dioxide, which precipitates. However, it can be dissolved using citric acid due to the formation of a complex.

An excess of 20 % of citric acid monohydrate was weight out assuming a 1:1 reaction with the metal cations.

All solutions were mixed in a fused silica beaker. The initially blue solution is heated until it thickens and a dark viscous gel is received. Heating upon further, formation of nitrous gases is observed and a bluish black foam is liberated from the gel. To fully decompose the foam, the beaker was placed on a tripod and heated with a Bunsen burner, until the bluish black foam spontaneously ignited leaving a black powder behind. The beaker with this powder was calcined at 800 °C for 4 hours in air. After calcination, the powder was pressed at 3000 bar using cold isostatic pressing (CIP) and sintered at 1300 °C for 7 h. The different steps of the powder synthesis are shown in Figure 19. The phase purity of the pellets was checked by X-ray diffraction (XRD). One pellet, which was not phase pure after this treatment was annealed again at 1400 °C for 12 h in air. Details regarding the XRD analysis will be discussed in section 4.1.
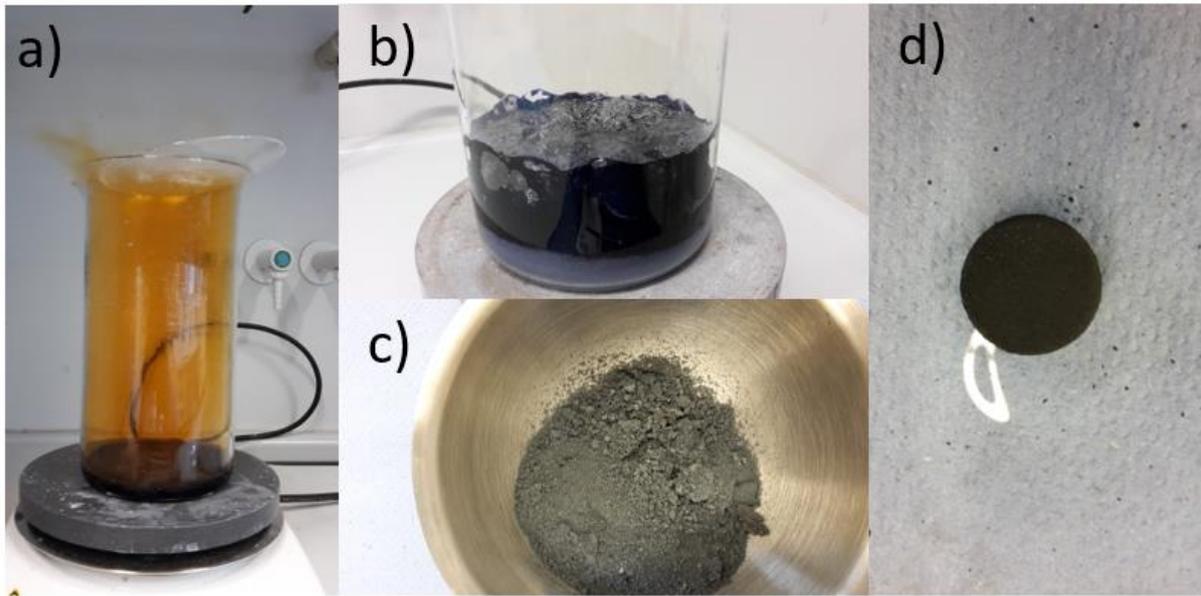
Figure 19: Different stages of the Pechini sythesis; a) formation of nitrous gases; b) thickening of the solution and formation of a gel and formation of a solid foam on the bottom of the beaker; c) obtained powder after calcination; d) pellet obtained by pressing of the remilled powder.

The sample was glued on the sample holder for the PLD. To this end, 1 g resin was mixed with 0.28 g hardener. One drop of the black sticky substance was placed between the sample and the sample holder and, in order to harden the resin, heated to 120 °C for 4 h, then to 180 ° for 1 h and finally to 220 °C for 1 h.

3.4 Pulsed laser depositon (PLD)

For the Van der Pauw measurements, thin films were deposited by PLD. The deposition parameters are shown in Table 4.

Table 4: Parameters for the thin film deposition.

Temperature [°C]	Pressure [mbar]	Energy per puls [mJ]	Time [min]	Rate [Hz]	Desired thickness [nm]
640 ± 10	$1.5*10^{-2}$	400	34	5	200

The obtained film thickness was determined by breaking the samples and analyzing the cross section by scanning electron microscopy (SEM); results of the measurements are shown in section 4.2.

3.5 Van-der-Pauw measurement

Figure 20 show the measurement setup.
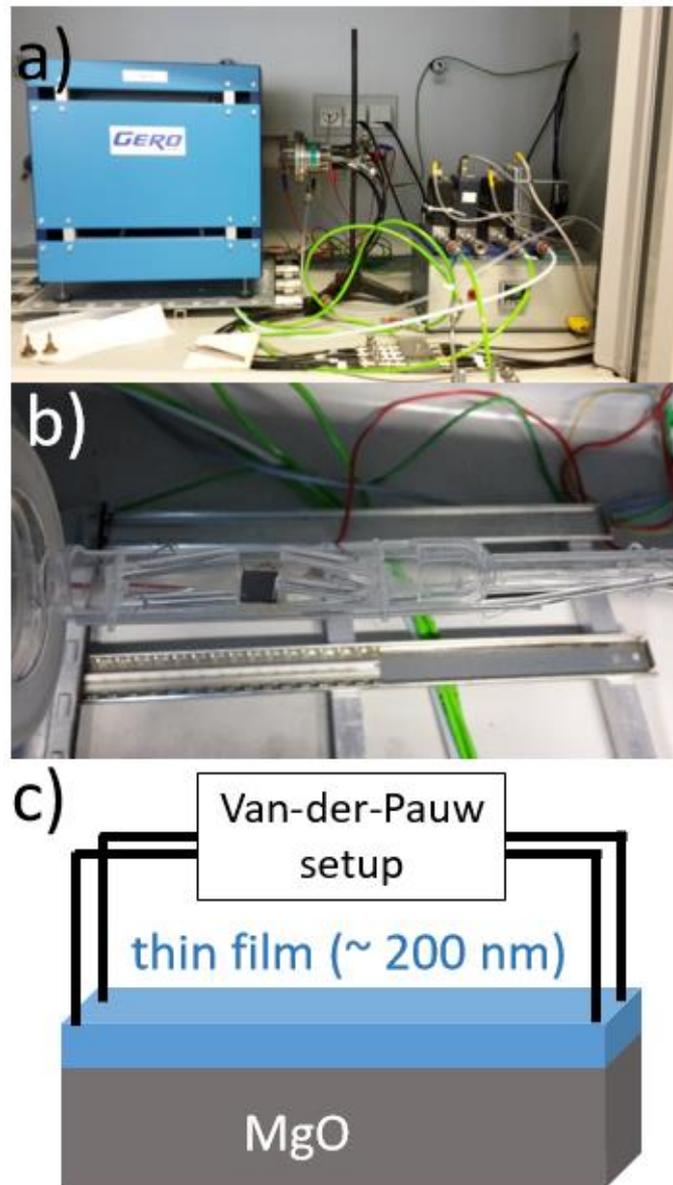
Figure 20: Van-der-Pauw measurement setup; a) overview of the measurement setup with mass flow controllers (MFCs) and the furnace; b) sample on the sample holder and contacted with Pt needles; c) schematic representation of the sample in the Van-der-Pauw measurement setup.

Van der Pauw measurements were carried out with different LSCrM compositions on three different substrates (MgO, Al_2O_3, $LaAlO_3$ (LAO)). Table 5 shows the parameters of the Van-der-Pauw measurements.

Table 5: Parameters for the Van-der-Pauw measurement.

T_{start} [°C]	T_{end} [°C]	Step [°C]	Number of Steps	Atmosphere	U [V]
300	950	50	14	humid H_2 (2.5 % H_2 in Ar, $H_2O:H_2$ = 1:1) 1 % O_2 in N_2 100 % O_2	± 0.01

As a reference, the substrates were measured without any thin film on them. To quantify parallel conduction pathways, uncoated substrates were measured as references.

Additionally, $La_{0.9}Sr_{0.1}Cr_{0.2}Mn_{0.8}O_{3-\delta}$ was deposited on all of these three substrates. These measurements were conducted to investigate the influence of the substrate on the conductivity of the thin film.

Table 6 provides an overview over all the measured samples.

Table 6: Overview of all measured types of samples.

Material	T_{start} [°C]	T_{end} [°C]	Atmosphere	Substrate
$LaCrO_{3-\delta}$	280	900	humid H_2 (2.5 % H_2 in Ar, $H_2O:H_2$ = 1:1), 1 % O_2, 100% O_2	MgO
$La_{0.9}Sr_{0.1}CrO_{3-\delta}$	280	900		MgO
$La_{0.8}Sr_{0.2}CrO_{3-\delta}$	280	900		MgO
$La_{0.9}Sr_{0.1}Cr_{0.9}Mn_{0.1}O_{3-\delta}$	280	900		MgO
$La_{0.9}Sr_{0.1}Cr_{0.85}Mn_{0.15}O_{3-\delta}$	280	900		MgO
$La_{0.9}Sr_{0.1}Cr_{0.8}Mn_{0.2}O_{3-\delta}$	280	900		MgO, Al_2O_3
$La_{0.9}Sr_{0.1}Cr_{0.65}Mn_{0.35}O_{3-\delta}$	280	900		MgO
$La_{0.9}Sr_{0.1}Cr_{0.5}Mn_{0.5}O_{3-\delta}$	280	900		MgO
$La_{0.9}Sr_{0.1}Cr_{0.2}Mn_{0.8}O_{3-\delta}$	280	900		MgO, Al_2O_3, LAO
$La_{0.8}Sr_{0.2}Cr_{0.2}Mn_{0.8}O_{3-\delta}$	280	900		MgO
$La_{0.6}Sr_{0.4}Cr_{0.2}Mn_{0.8}O_{3-\delta}$	280	900		MgO
$La_{0.5}Sr_{0.5}Cr_{0.2}Mn_{0.8}O_{3-\delta}$	280	900		MgO, LAO

3.6 Sample preparation for electrochemical impedance spectroscopy measurements

The samples used for impedance spectroscopy were prepared as follows: At first, a Ni/YSZ paste and subsequently a Ni paste was screen printed on the bottom of the substrate as a current collector. After drying at 300 °C for 30 min, the sample was sintered at 1250 °C for 2 h in air.

For preparation of model-composite electrodes with a buried current collector (see Figure 21.b), Ti (5 nm)/Pt (100 nm) layer was sputter deposited on the polished side of the substrate. From this Ti/Pt metal thin film a current collecting grid with 10 μm stripe width and 10 μm stripe distance was prepared by micro structuring using photolithography and ion beam etching:

1. Photoresist was spin coated for 45 sec on the YSZ substrate. Then the photoresist was dried on a hot plate.
2. A mask for photolithography was aligned and the photoresist was hardened by UV light.
3. The YSZ was then placed in a developer solution. Colorful streaks can be observed when the photoresist unaffected by the UV light dissolves. When the streaks disappear, the sample was put in water to stop the developer solution.
4. Using ion beam etching, the unprotected Pt layer was etched away.
5. Then the desired LSCrM thin film (220 nm) was deposited on top of the Ti/Pt grid using PLD.
6. In order to obtain microelectrodes, the obtained model-composite thin film was structured via photolithography and ion beam etching as well (see steps 1 – 4).

The used microelectrodes are circular with 300 μm in diameter. Figure 21 shows the sample and the measurement setup.

3.7 Electrochemical impedance spectroscopy measurement

Impedance measurements were carried out in humid H_2 (H_2O:H_2 = 1:1) and in 100 % O_2 over a temperature range between 300 °C and 950 °C. Impedance results recorded of LSCrM at temperatures lower than 650 °C, however, could not be analyzed further due to high data scattering most probably caused by too little conductivity. The asymmetrically heated micro-contact measurement setup [71] is shown in Figure 21.
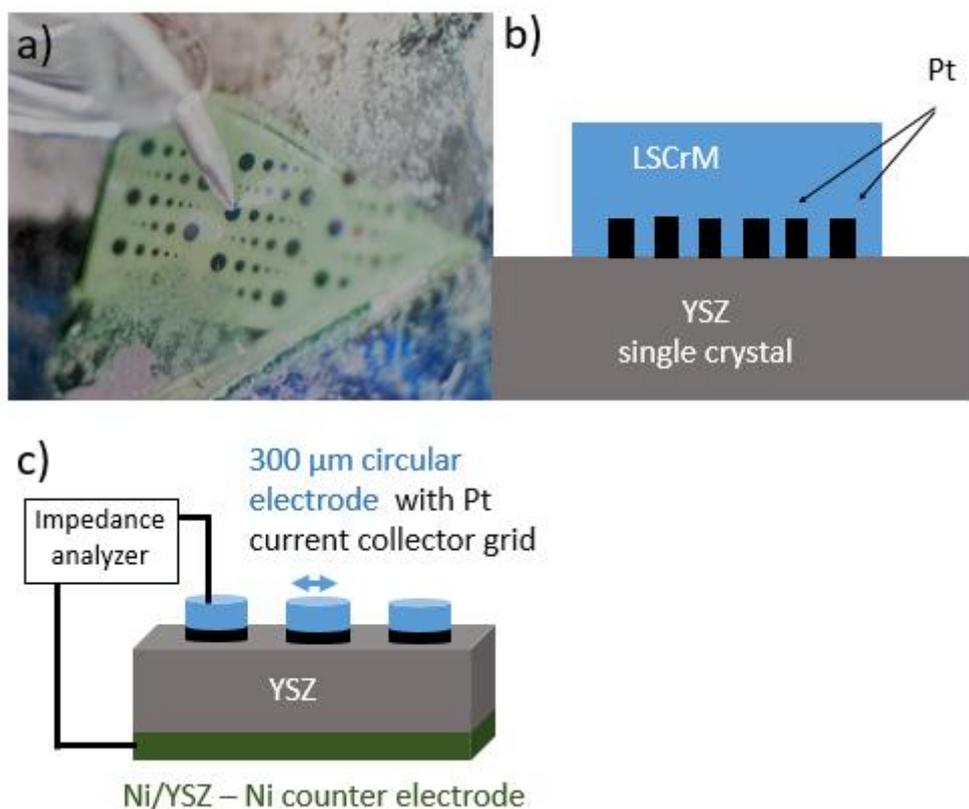
Figure 21: Electrochemical Impedance Spectroscopy measurement and setup; a) Pt needle contacting a microelectrode; b) schematic representation of the Pt grid buried beneath the electrode; c) schematic representation of the measurement setup.

The parameters as well as the samples that were characterized with electrical impedance spectroscopy are listed in Table 7.

Table 7: Parameters and overview of the samples characterized by means of impedance spectroscopy.

Material	T_{start} [°C]	T_{end} [°C]	Atmosphere	Substrate	Pt current collector
$La_{0.9}Sr_{0.1}CrO_{3-\delta}$	660	900	Humid H_2	MgO	Yes
$La_{0.9}Sr_{0.1}Cr_{0.9}Mn_{0.1}O_{3-\delta}$	660	900	(2.5 % H_2 in Ar,	MgO	Yes
$La_{0.9}Sr_{0.1}Cr_{0.65}Mn_{0.35}O_{3-\delta}$	760	900	$H_2O:H_2$ = 1:1),	MgO	Yes
$La_{0.9}Sr_{0.1}Cr_{0.2}Mn_{0.8}O_{3-\delta}$	660	900	100 % O_2	MgO,	Yes

4 Results and discussion

4.1 XRD

The powders were analyzed by means of X-ray diffraction after pressing and sintering at 1300 °C in a Pt crucible. Figure 22 shows the typically obtained diffractogram. All peaks can be attributed to an orthorhombic perovskite, a minor impurity (< 1 %, peak at 30 °) could not be identified. Diffractograms are shown in Figure 22 to Figure 27.
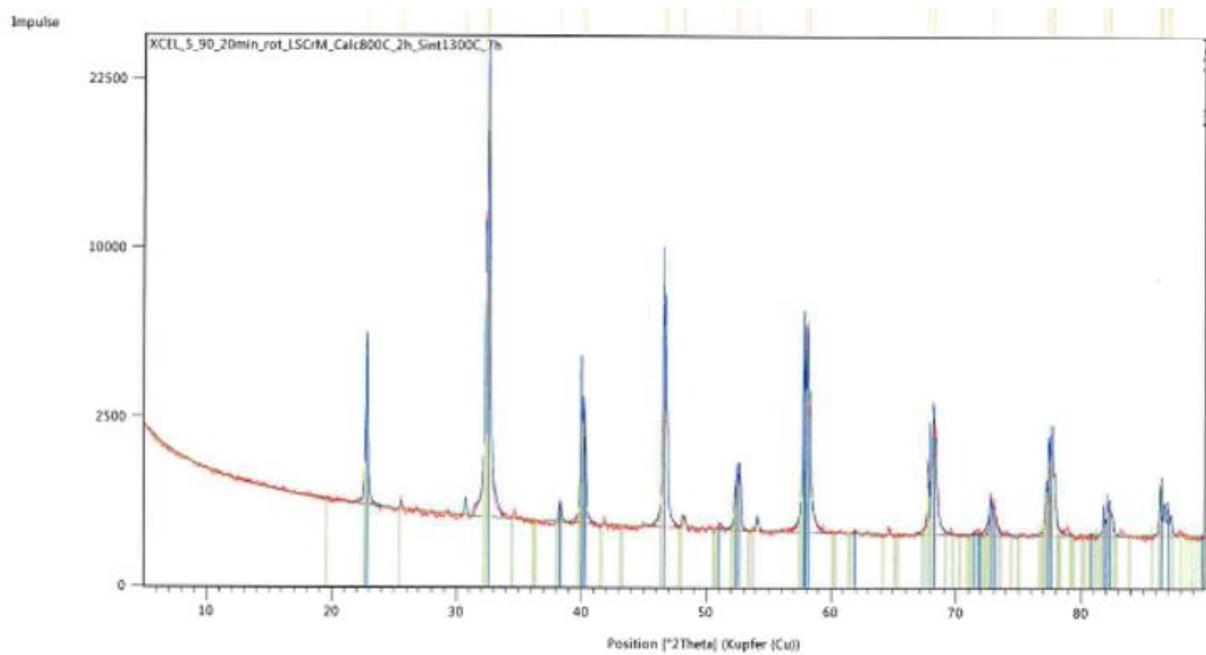
Figure 22: Diffractogram of $La_{0.9}Sr_{0.1}Cr_{0.5}Mn_{0.5}O_{3-\delta}$; after sintering at 1300 °C for 7 h; minor impurity at about 30°; blue: 04-013-5344 $Sr_{0.25}La_{0.75}Cr_{0.5}Mn_{0.5}O_3$; green: 04-013-5342 $Sr_{0.25}La_{0.7}CrO_3$.
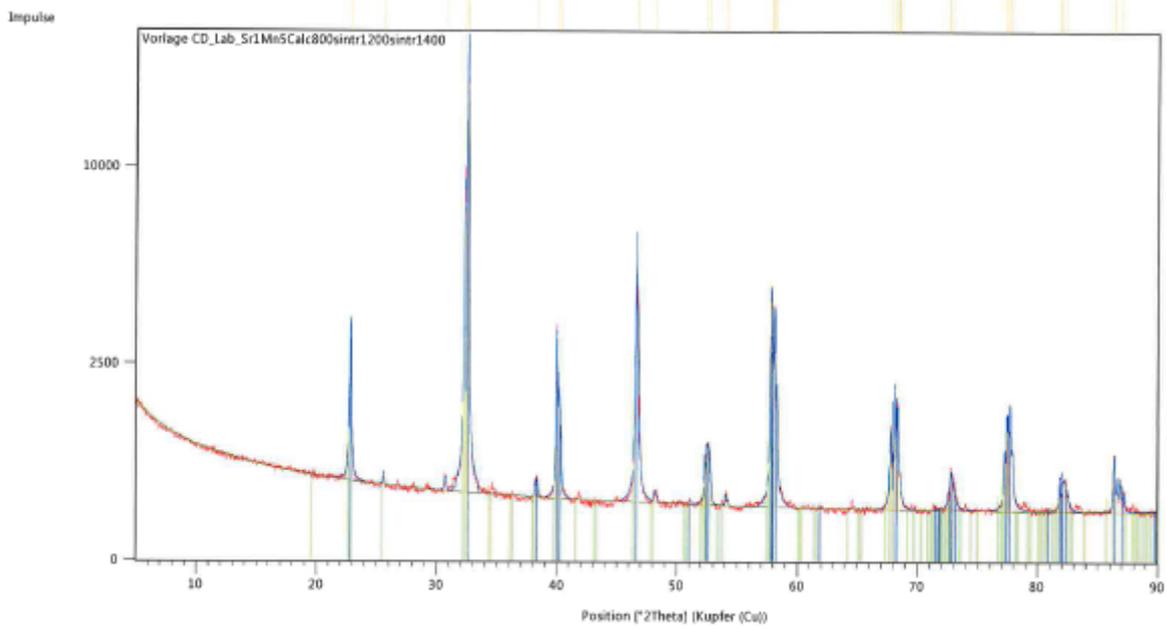
Figure 23: Diffractogram of La$_{0.9}$Sr$_{0.1}$Cr$_{0.5}$Mn$_{0.5}$O$_{3-\delta}$; after sintering at 1300 °C for 7 h and then sintering again at 1400 °C for 12 h; minor impurity at about 30° still observable, but < 1%; blue: 04-013-5344 Sr$_{0.25}$La$_{0.75}$Cr$_{0.5}$Mn$_{0.5}$O$_3$; green: 04-013-5342 Sr$_{0.25}$La$_{0.7}$CrO$_3$.
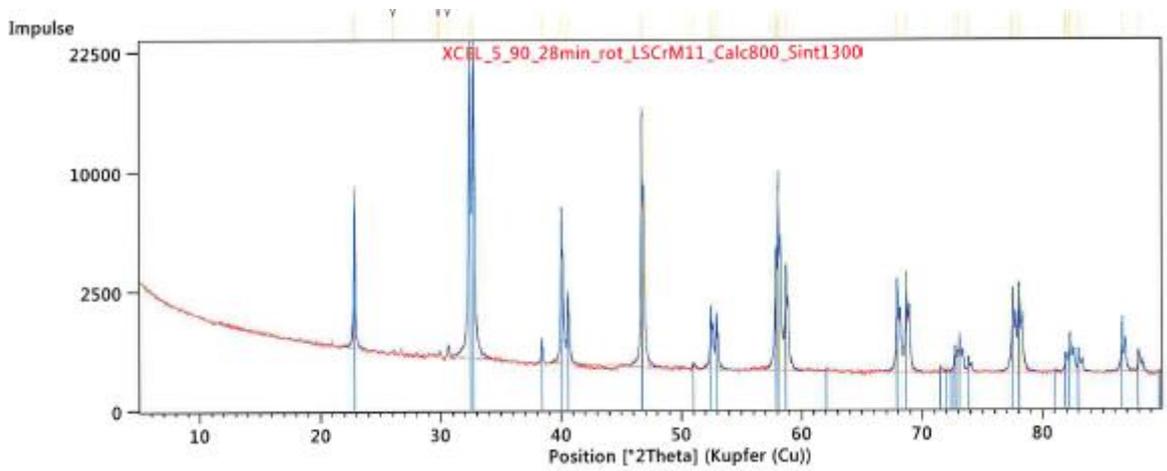
Figure 24: Diffractogram of La$_{0.9}$Sr$_{0.1}$Cr$_{0.9}$Mn$_{0.1}$O$_3$; blue: 01-089-2469 La$_{0.96}$MnO$_{3.05}$.
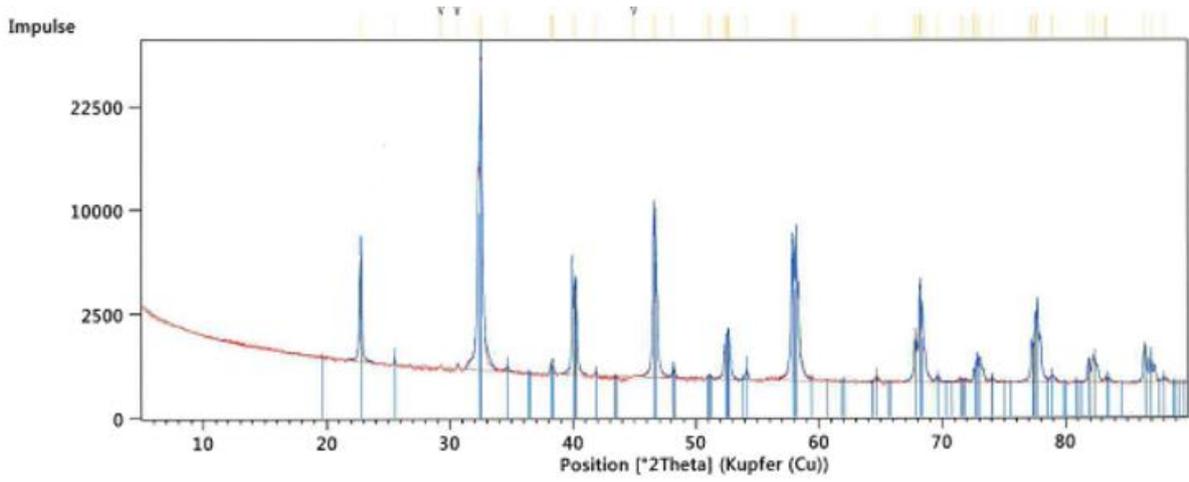
Figure 25: Diffractogram of $La_{0.9}Sr_{0.1}Cr_{0.85}Mn_{0.15}O_3$; blue: 04-010-1333 $LaCrO_3$.
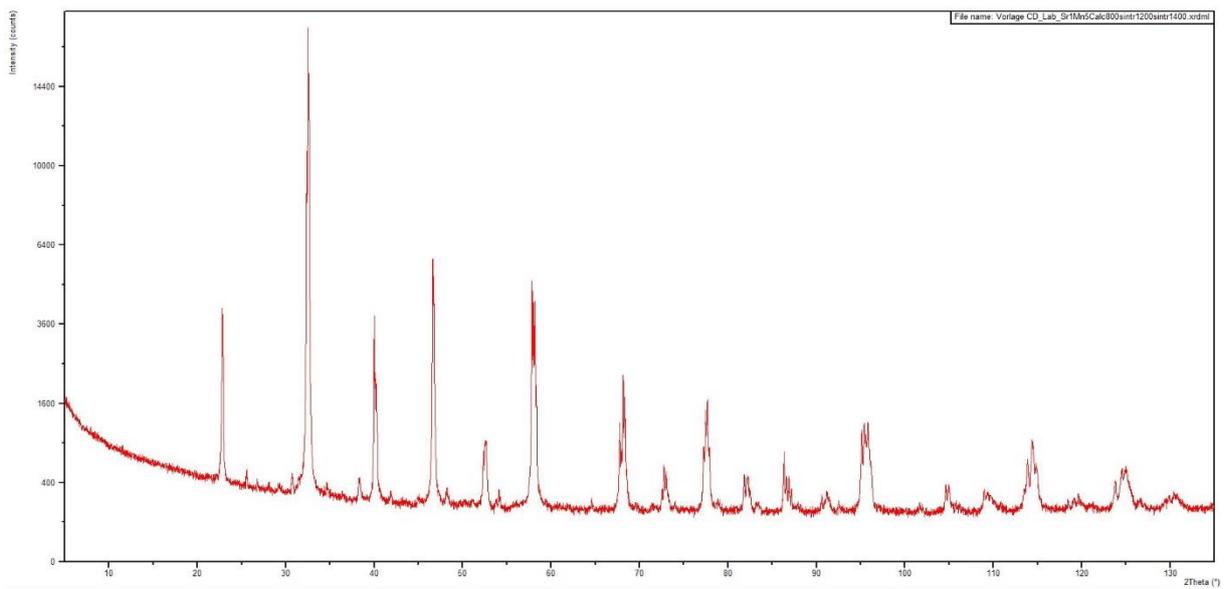
Figure 26: Diffractogram of $La_{0.9}Sr_{0.1}Cr_{0.65}Mn_{0.35}O_{3-\delta}$.
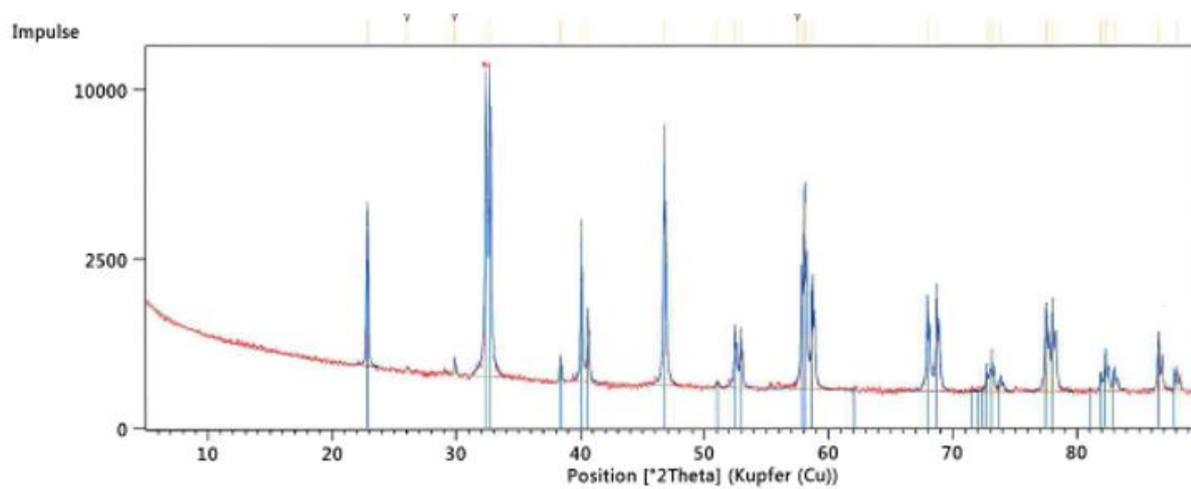
Figure 27: Diffractogram of La$_{0.8}$Sr$_{0.2}$Cr$_{0.2}$Mn$_{0.8}$O$_3$; blue: 04-013-6899 Sr$_{0.3}$La$_{0.7}$Cr$_{0.08}$Mn$_{0.92}$O$_3$.

4.2 Film thickness

The samples were broken and the cross section was analyzed by scanning electron microscopy. The film thickness could be determined, as one can see in Figure 28 and Figure 29. Results for different samples are listed in Table 8. While the same deposition parameters (see Table 4) were used, a variation of the obtained film thickness can be observed. Especially samples with both high Sr and high Mn concentrations seem to produce thicker thin films under the same parameters used for PLD deposition. This can be seen in Figure 30.

HV	mag □	WD	det	spot	tilt	HFW	⊢——— 1 µm ———⊣
10.00 kV	100 000 x	8.5 mm	ETD	3.0	-3 °	4.14 µm	
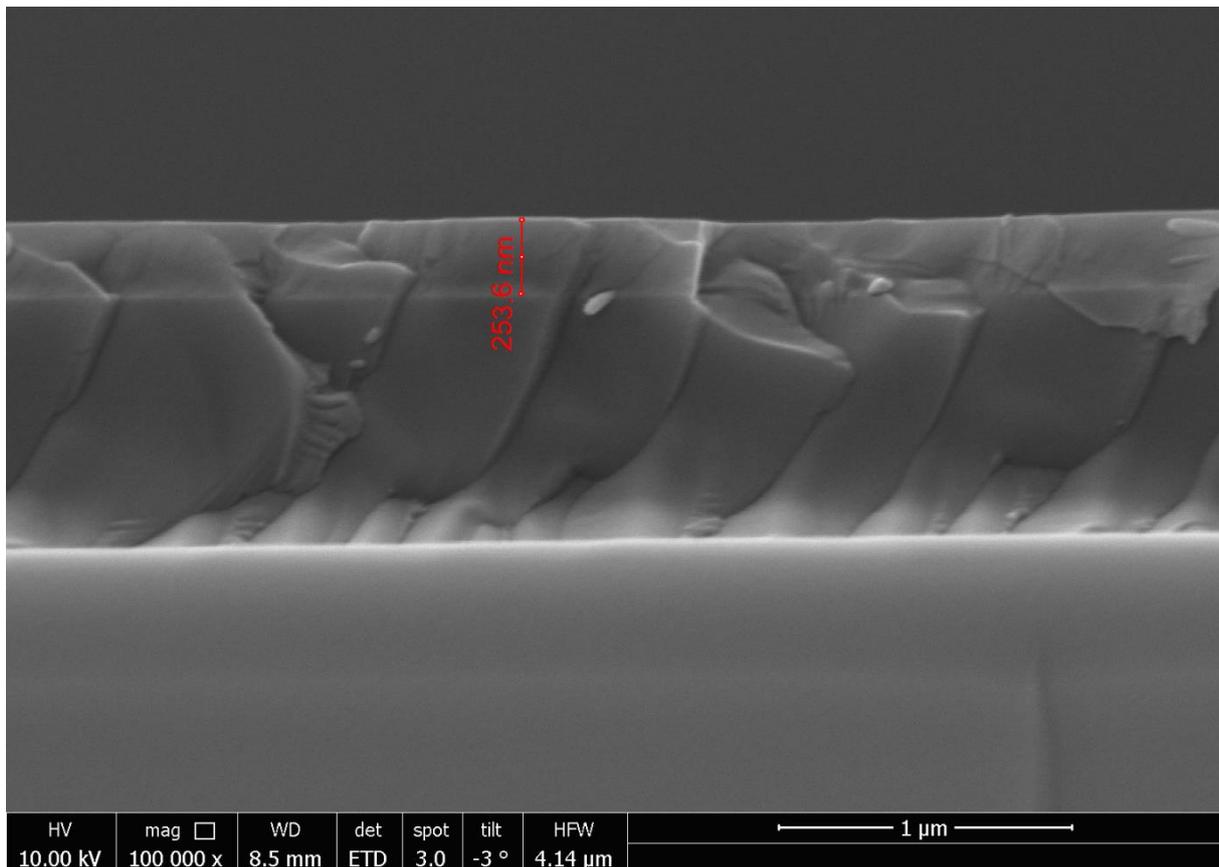
Figure 28: SEM cross-section of La$_{0.9}$Sr$_{0.1}$Cr$_{0.2}$Mn$_{0.8}$O$_{3-\delta}$ on LaAlO$_3$.
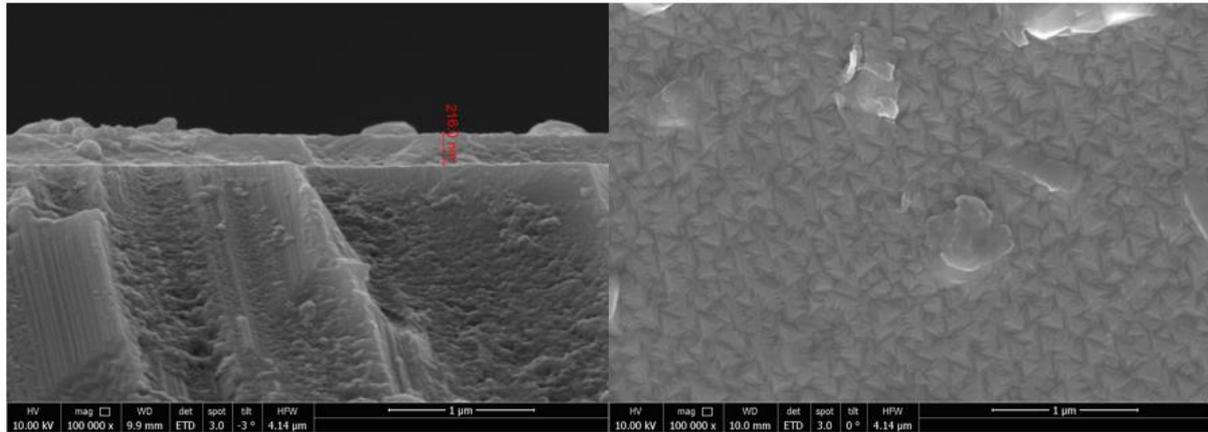
Figure 29: SEM images of La$_{0.9}$Sr$_{0.1}$Cr$_{0.8}$Mn$_{0.2}$O$_{3-\delta}$ on Al$_2$O$_3$; a) cross section; b) surface.

Table 8: Film thicknesses of all deposited thin films.

Material	Substrate	Film thickness [nm]
LaCrO$_{3-\delta}$	MgO	162
La$_{0.9}$Sr$_{0.1}$CrO$_{3-\delta}$	MgO	202
La$_{0.8}$Sr$_{0.2}$CrO$_{3-\delta}$	MgO	218
La$_{0.9}$Sr$_{0.1}$Cr$_{0.9}$Mn$_{0.1}$O$_{3-\delta}$	MgO	208
La$_{0.9}$Sr$_{0.1}$Cr$_{0.85}$Mn$_{0.15}$O$_{3-\delta}$	MgO	202
La$_{0.9}$Sr$_{0.1}$Cr$_{0.8}$Mn$_{0.2}$O$_{3-\delta}$	MgO	286
La$_{0.9}$Sr$_{0.1}$Cr$_{0.8}$Mn$_{0.2}$O$_{3-\delta}$	MgO	219
La$_{0.9}$Sr$_{0.1}$Cr$_{0.8}$Mn$_{0.2}$O$_{3-\delta}$ (deposition T: 550 °C)	Al$_2$O$_3$	207
La$_{0.9}$Sr$_{0.1}$Cr$_{0.8}$Mn$_{0.2}$O$_{3-\delta}$	Al$_2$O$_3$	216
La$_{0.9}$Sr$_{0.1}$Cr$_{0.65}$Mn$_{0.35}$O$_{3-\delta}$	MgO	221
La$_{0.9}$Sr$_{0.1}$Cr$_{0.5}$Mn$_{0.5}$O$_{3-\delta}$	MgO	259
La$_{0.9}$Sr$_{0.1}$Cr$_{0.2}$Mn$_{0.8}$O$_{3-\delta}$	MgO	289
La$_{0.9}$Sr$_{0.1}$Cr$_{0.2}$Mn$_{0.8}$O$_{3-\delta}$	Al$_2$O$_3$	264
La$_{0.9}$Sr$_{0.1}$Cr$_{0.2}$Mn$_{0.8}$O$_{3-\delta}$	LAO	205
La$_{0.8}$Sr$_{0.2}$Cr$_{0.2}$Mn$_{0.8}$O$_{3-\delta}$	MgO	254
La$_{0.6}$Sr$_{0.4}$Cr$_{0.2}$Mn$_{0.8}$O$_{3-\delta}$	MgO	283
La$_{0.5}$Sr$_{0.5}$Cr$_{0.2}$Mn$_{0.8}$O$_{3-\delta}$	MgO	305
La$_{0.5}$Sr$_{0.5}$Cr$_{0.2}$Mn$_{0.8}$O$_{3-\delta}$	LAO	280
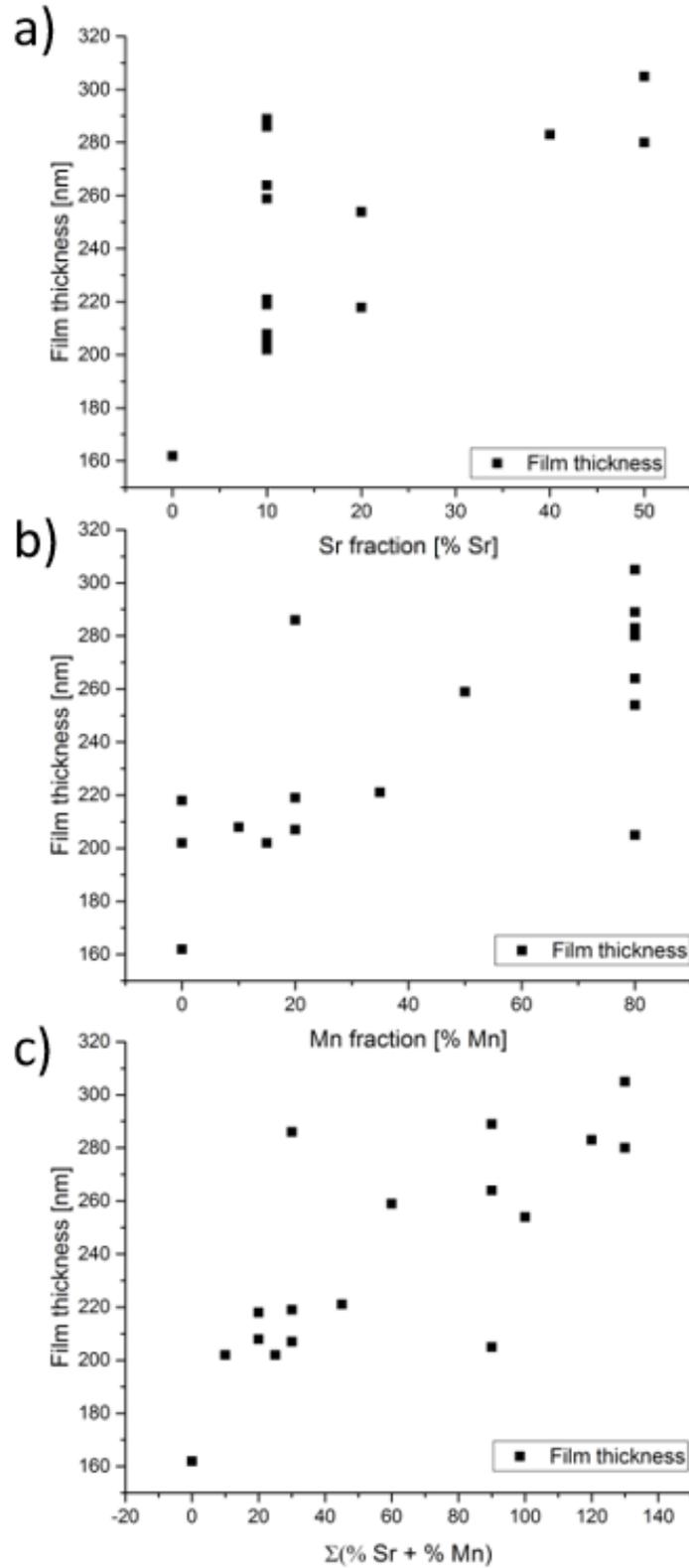
Figure 30: Dependency of the film thickness on the composition; a) film thickness vs. Sr fraction; b) film thickness vs. Mn fraction; c) film thickness vs. the sum of the Sr fraction and the Mn fraction; All films were obtained under nominally identical PLD conditions.

4.3 Van-der-Pauw measurements

4.3.1 Choice of substrate

The Van-der-Pauw method was used to compare the conductivity of thin layers of different LSCrM compositions, see section 2.7. The required substrates were judged regarding the following properties:

- It should be an insulator. For the used substrate geometry (10 mm x 10 mm x 0.1 mm) the substrate was regarded as sufficiently insulating if on the bare crystal currents lower that 1 nA are measured for a voltage of 0.01 V in the Van-der-Pauw geometry.
- There should be a suitable growth of the thin film on the substrate (e.g. ideally epitaxy). For example, cracks within the thin film could be a problem, especially continuous cracks, which force the current through the insulating substrate. No cracks were observed in the SEM.

The limit of 1 nA was defined as follows: An electrode material should have a conductivity of at least 1 S/cm [47, 61]. However, since lower conductivities might also be of interest in this work, a lower limit of the conductivity of the thin film samples of 10^{-2} S/cm was assumed. The current, which flows through a thin film with 200 nm thickness and a conductivity of 10^{-2} S/cm, is approximately 2 nA for 0.01 V. This result was rounded down to 1 nA. Hence, any substrate showing a current flow higher than 1 nA at any temperature will be rejected as a viable material for the subsequent thin film conductivity measurements. The basic principle of the Van-der-Pauw geometry are shown in Figure 14, the distance of the Pt contacts was about 0.9 cm.

In order to choose a proper substrate, blank (i.e. without any conducting layers deposited on them) MgO, $LaAlO_3$ (LAO) and Al_2O_3 single crystals were measured in the Van-der-Pauw setup.

When measuring the conductivity of thin films, at first, the ratio of the two different modes is determined by measuring the sample in $R_{AB,CD}$ mode and then, after switching the contacts, in

the $R_{BC,DA}$ mode (see Figure 14). The respective resistances can be calculated from the measured currents and applied voltages. Typically, the measured currents were between 10^{-8} A and 10^{-5} A at 900 °C for thin films with low or high conductivity, respectively. For the actual measurement of the sample, measuring in only one measurement mode is enough since the resistance of the other one can be calculated with the previously determined ratio. Using $R_{AB,CD}$ and $R_{BC,DA}$, the geometric factor can be determined using equation 2.20. The conductivity is then obtained using equation 2.19.

Figure 31 shows the current for the three different substrate materials for different temperatures.
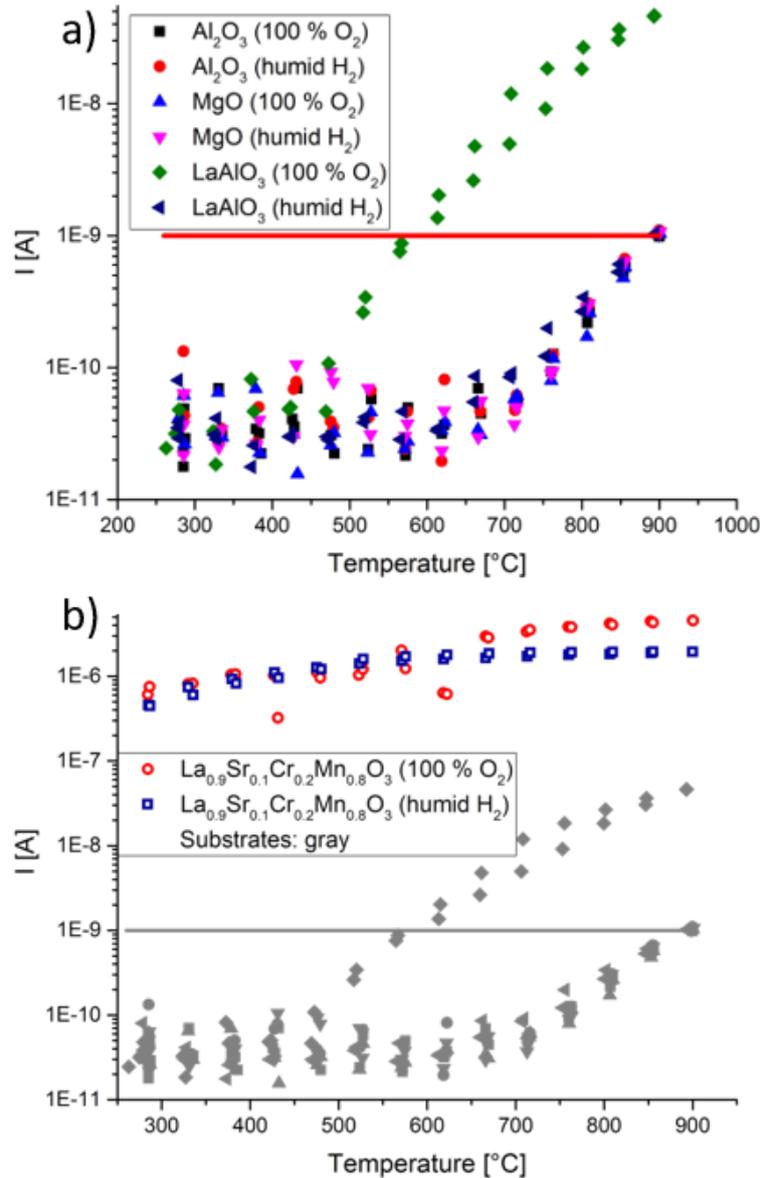
Figure 31: Current vs temperature for different substrate materials; the red line indicates 1 nA; a) detailed comparison of the respective substrate materials; b) currents measured for La$_{0.9}$Sr$_{0.1}$Cr$_{0.2}$Mn$_{0.8}$O$_3$ on MgO compared with the currents measured for the substrates.

MgO and Al$_2$O$_3$ are insulating materials, while the current measured in LAO in 100 % O$_2$ exceeds the limit of 1 nA. The measured current for LAO is still very low, however, it is about one order of magnitude higher than in MgO or sapphire. Depending on the conductivity of a deposited thin film, the electrical current could partially flow via the LAO substrate, thus leading to invalid conductivity measurements. This effect would be most pronounced for thin layers or low film conductivities. However, LAO was still not ruled out completely. While it

cannot properly be used for thin films with low conductivities under oxidizing conditions, it might be suitable for materials with high conductivities.

As a next step, $La_{0.9}Sr_{0.1}Cr_{0.2}Mn_{0.8}O_{3-\delta}$ was deposited on all three substrates and the conductivity of the thin film was measured. Figure 32 show the conductivity of the thin film deposited on the different substrates for different atmospheres. In wet H_2, the conductivity of the $La_{0.9}Sr_{0.1}Cr_{0.2}Mn_{0.8}O_{3-\delta}$ thin film showed the highest conductivity on LAO, followed by MgO, and the lowest conductivity was observed on sapphire. When looking at the conductivities of the thin film in 1 % O_2, the highest conductivity can again be observed on LAO, which is about twice as high as the measured conductivity on the other substrates. In contrast to the conductivity in wet H_2, the thin films measured on MgO and Al_2O_3 show good agreement when measured in 1 % O_2.
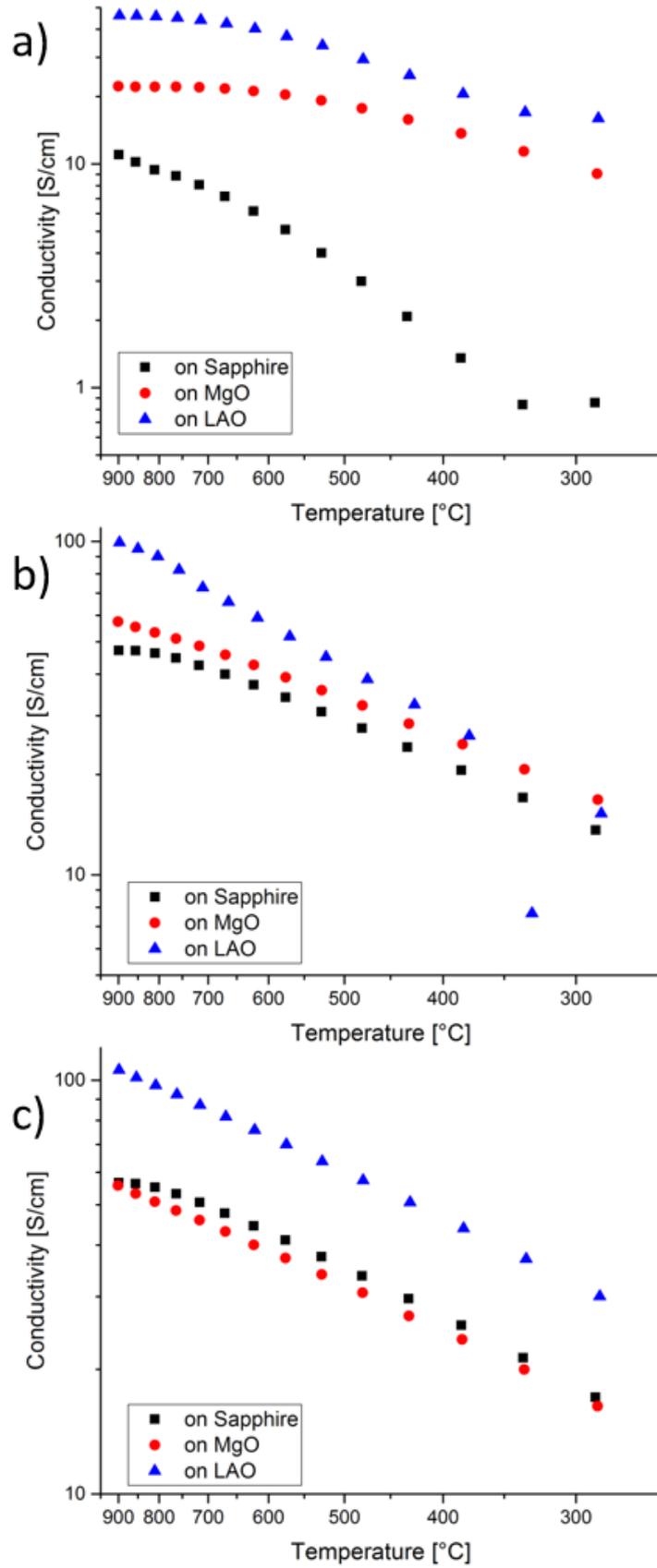
Figure 32: Conductivity of $La_{0.9}Sr_{0.1}Cr_{0.2}Mn_{0.8}O_{3-\delta}$ deposited on different substrates measured in different atmospheres: a) humid H_2; b) 1 % O_2; c) 100 % O_2.

Excellent agreement of conductivities was found for the thin films deposited on MgO and Al_2O_3 measured in 100 % O_2. The conductivity of the thin film deposited on LAO, however, is again higher. However, the higher conductivities found for layers on LAO cannot be ascribed to parallel current pathways through the substrate as this effect would be less pronounced at lower temperatures, which is not the case. LAO and LSCrM have very similar lattice parameters, therefore, it is reasonable to assume that epitaxial layers were grown on this substrate [72]. The absence of grain boundaries would consequently explain the higher conductivities [73].

While LAO seems to be a great substrate for materials with high conductivity, it cannot properly be used for films with low conductivity. Therefore, MgO was chosen as substrate for most measurements, also due to the consistency with the thin film deposited on Al_2O_3. In addition, LAO was used for samples with a high conductivity. When the sample has a rather high conductivity (e.g. 100 S/cm at 900 °C), the vast majority of the current takes the path via the thin film, meaning that the resulting error due to parallel current pathways through the substrate is negligible.

4.3.2 Van-der-Pauw measurements of thin films

When looking at LSCrM, there are two ways of changing the properties of the material, doping the A site with Sr and varying the Cr:Mn ratio on the B site. In order so separate the effects of the respective strategies, three different measurement series were conducted, keeping one of those two parameters constant in each measurement series. Therefore, the A-site doping was investigated for fixed Cr:Mn ratios, while the effect of different Cr:Mn ratios was studied for a constant Sr dopant concentration. Figure 33 shows the prepared samples and their subdivision into different measurement series.
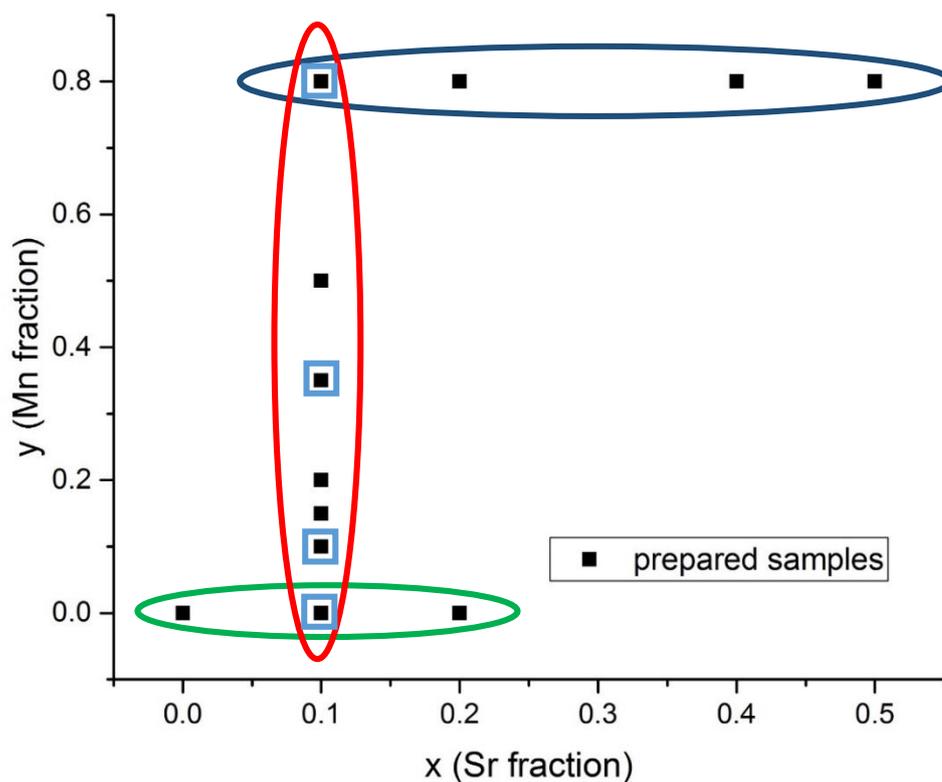
Figure 33: Composition of the prepared samples and their subdivision into different measurement series; elliptically highlighted compositions show the measurement series analyzed by Van-der-Pauw measurements; individual compositions highlighted by light blue squares show the compositions analyzed by Electrochemical Impedance Spectroscopy (EIS).

4.3.2.1 Investigation of the effect of Sr-doping on $La_{1-x}Sr_xCrO_{3-\delta}$

This measurement series is highlighted in green in Figure 33. The Sr concentration on the A-site was varied while keeping the Cr:Mn ratio constant. In this case, no Mn doping was introduced on the B-site.

Measurements in humid H_2

The conductivity of LSCr in humid hydrogen is heavily dependent on the Sr content (see Figure 34): The conductivity of the undoped sample ($LaCrO_3$) is about two orders of magnitude lower than the conductivity of the doped ones. Especially at lower temperatures (300 °C – 500 °C) in reducing atmospheres, the calculation of the conductivity for $LaCrO_3$ sometimes yields nonsensical negative values due to the high resistance. For $La_{0.9}Sr_{0.1}CrO_3$ and $La_{0.8}Sr_{0.2}CrO_3$, Sr dopant was introduced to the A site of the perovskite. The Sr carries a negative relative charge, which is compensated by defects, namely electron holes or oxygen vacancies (see chapter 2.1). This increase of charge carriers results in a dramatically increased conductivity compared to the undoped sample. The conductivity does not seem to increase upon further Sr doping, when comparing $La_{0.9}Sr_{0.1}CrO_{3-\delta}$ and $La_{0.8}Sr_{0.2}CrO_{3-\delta}$, at least not at high temperatures.

The activation energy for $LaCrO_{3-\delta}$ is 1.37 eV, for 10 % Sr dopant concentration it is 0.56 eV. For the sample with 20% doping, no single linear relationship could be determined in the $\log(\sigma T)$ vs. 1/T Arrhenius plot (see section 2.2.2), therefore two activation energies were determined: It is 0.71 eV between 290 °C and 570 °C and 0.43 eV between 620 °C and 900 °C.
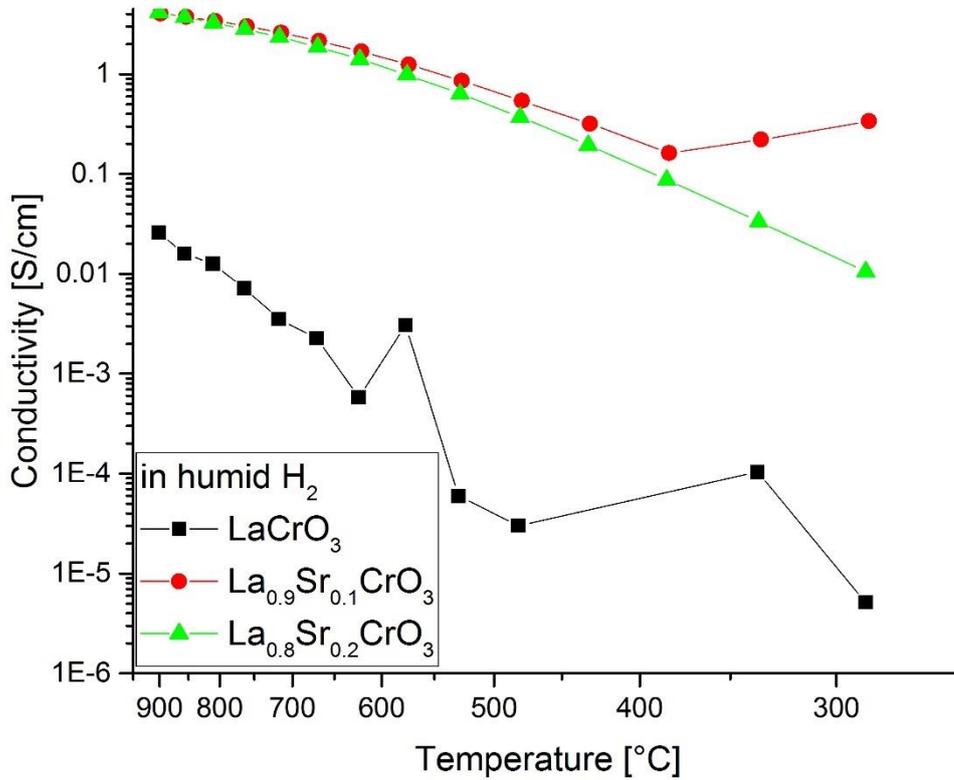
Figure 34: Arrhenius-type diagram of conductivity vs. temperature for La$_{1-x}$Sr$_x$CrO$_{3-\delta}$ in humid H$_2$ (see Table 5).

Measurements in 1 % O$_2$

In Figure 35 the conductivity values for La$_{1-x}$Sr$_x$CrO$_{3-\delta}$ in 1% O$_2$ are plotted. For LaCrO$_{3-\delta}$, still low, but more reliable values (i.e. less data scattering) for the conductivity can be obtained. The increase in conductivity when doping LaCrO$_3$ with Sr is about one order of magnitude. Higher amounts of Sr increase the conductivity further, resulting in a slightly higher conductivity for La$_{0.8}$Sr$_{0.2}$CrO$_{3-\delta}$. The increased conductivity for the sample with 20 % Sr in comparison to the sample with 10 % Sr can be seen in equation 4.1. The amount of charge carriers is determined by the Sr concentration:

$$[Sr'_{La}] = [h^\bullet] + 2 \ [V_O^{\bullet\bullet}] \tag{4.1}$$

In oxidizing atmospheres, electron holes are formed, therefore:

$$[Sr'_{La}] \approx [h^\bullet]$$

71

Increasing the Sr-concentration by a factor of two, therefore, leads to double the charge carrier concentration and, hence, assuming a concentration independent mobility, double the conductivity (see Figure 35).

The activation energy is about 0.30 eV for $LaCrO_{3-\delta}$, 0.14 eV for $La_{0.9}Sr_{0.1}CrO_{3-\delta}$ and 0.15 eV for $La_{0.8}Sr_{0.2}CrO_{3-\delta}$ in 1% O_2.
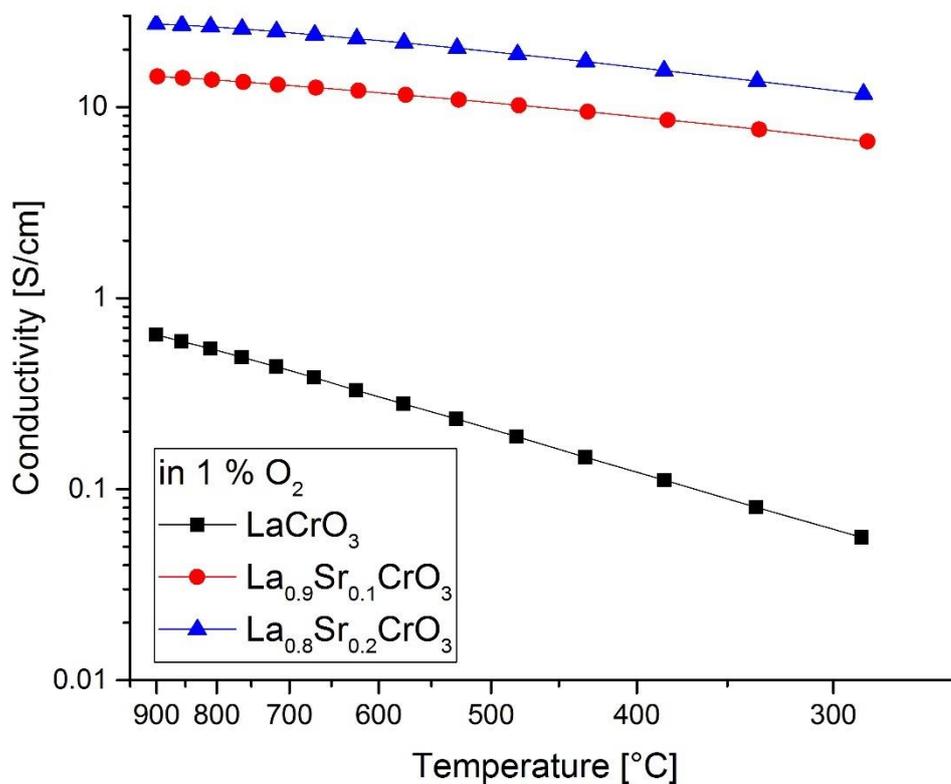
Figure 35: Arrhenius-type diagram of conductivity vs. temperature for $La_{1-x}Sr_xCrO_{3-\delta}$ in 1 % O_2 (see Table 5).

Measurements in 100 % O_2

The results are similar to what was observed under 1% O_2. The conductivity for $LaCrO_3$ is slightly higher than in 1 % O_2, but still lower than 1 S/cm. By doping, an increase in conductivity by one order of magnitude can be observed, compared to the undoped material (cf. Figure 36).

72

As already shown for the measurement series in 1 % O_2, twice the amount of Sr leads to double the conductivity.

The activation energy for $LaCrO_{3-\delta}$ is 0.29 eV in 100 % O_2, for $La_{0.9}Sr_{0.1}CrO_{3-\delta}$ it is 0.14 eV and for $La_{0.8}Sr_{0.2}CrO_{3-\delta}$ it is 0.15 eV.
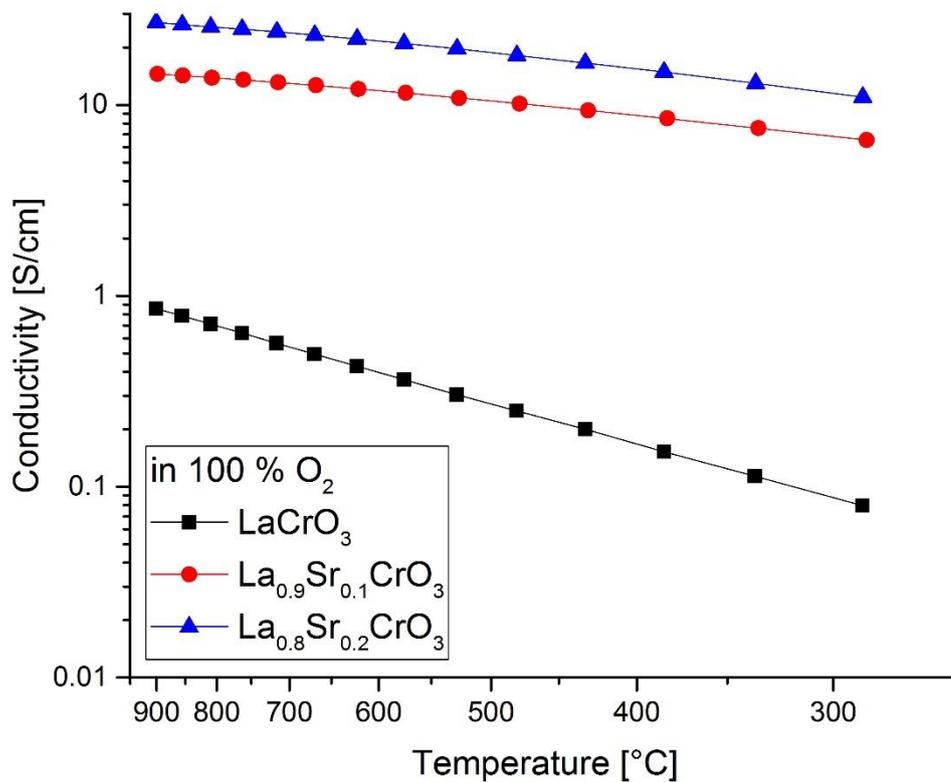
Figure 36: Arrhenius-type diagram of conductivity vs. temperature for $La_{1-x}Sr_xCrO_{3-\delta}$ in 100 % O_2 (see Table 5).

Discussion

Figure 37 and Figure 38 show the conductivity at 810 °C as well as the activation energy for conduction for this measurement series. In undoped $LaCrO_{3-\delta}$, the lowest conductivity was found as well as the highest activation energy. In $LaCrO_{3-\delta}$, the amount of charge carriers is limited to intrinsic charge carriers. For the undoped material, there is only a small amount of defects, in case there are no impurities or cation vacancies (see chapter 2.1), therefore:

$$2 [V_O^{\bullet\bullet}] = [e'] \qquad\qquad (4.2)$$

$$[V_O^{\bullet\bullet}] * \sqrt{p_{O_2}} * [e']^2 = K' \qquad\qquad (4.3)$$

However, if the sample were n-type conducting in the measured atmospheres, then the conductivity in humid H_2 should be higher. This suggests a small impurity as a dopant in the nominally undoped sample, which would explain the larger conductivities in oxidizing atmospheres. However, electrons might be the predominant charge carriers contributing to the conduction in H_2.

By introducing Sr to the A site of the perovskite, one electron hole (or half an oxygen vacancy) has to be formed for every Sr ion in order to compensate for the relative charge. The conductivity can be increased by two orders of magnitude for 10 % and 20 % Sr, when compared to the nominally undoped sample, under reducing atmospheres. For oxidizing atmospheres, the conductivity can be increased by one order of magnitude. The charge carriers induced by the Sr doping account for the increase in conductivity, as the conductivity is a function of the amount of charge carriers (see section 2.2). In 1 % O_2 and 100 % O_2, doubling the Sr dopant concentration yields double the conductivity (cf. equation 4.1).

The difference between reducing and oxidizing atmospheres can be seen in equation 4.4, since the oxygen partial pressure influences the equilibrium of defects.

$$K = \frac{[V_O^{\bullet\bullet}] * \sqrt{p_{O_2}}}{[h^\bullet]^2} \qquad\qquad (4.4)$$

Bulk conductivities from literature is shown in Table 9.

Table 9: Bulk conducitivities for LaCrO₃ and and Sr-doped LaCrO₃ reported in literature.

Material	Atmosphere	Temperature [°C]	Conductivity [S/cm]	Size [mm]	Reference
$LaCrO_3$	Air	800	0.11	56 x 33 x 17	[74]
$LaCrO_3$	3 % H_2-Ar		0.02		
$LaCrO_3$	Air	800	0.96	26 x 8 x 5	[75]
$LaCrO_3$	10 % H_2-N_2		0.26		
$La_{0.75}Sr_{0.25}CrO_3$	Air		59.1		
$La_{0.75}Sr_{0.25}CrO_3$	10 % H_2-N_2		7.07		

The conductivities obtained for the thin films in this work are 0.71 S/cm in 100 % O_2 and 0.01 S/cm in humid H_2 for the nominally undoped $LaCrO_3$. For $La_{0.8}Sr_{0.2}CrO_3$, a conductivity of 25.7 S/cm was found in 100 % O_2 and 3.28 S/cm in humid H_2 (see Figure 37), which is roughly half the conductivity that was found for bulk samples (see Table 9).
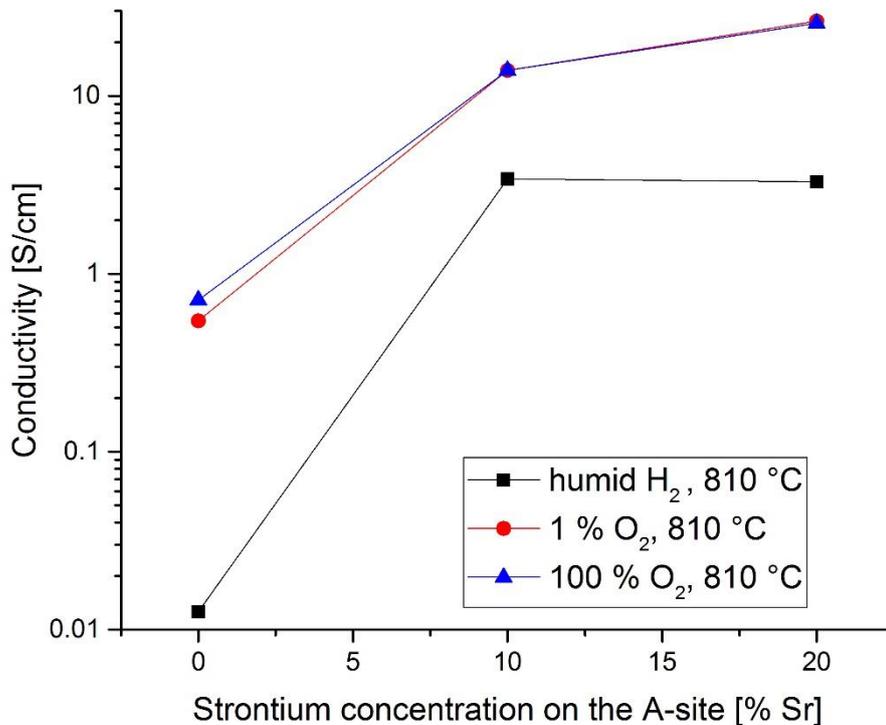
Figure 37: Conductivity vs. Sr concentration for $La_{1-x}Sr_xCrO_{3-\delta}$ for different atmospheres at 810 °C.
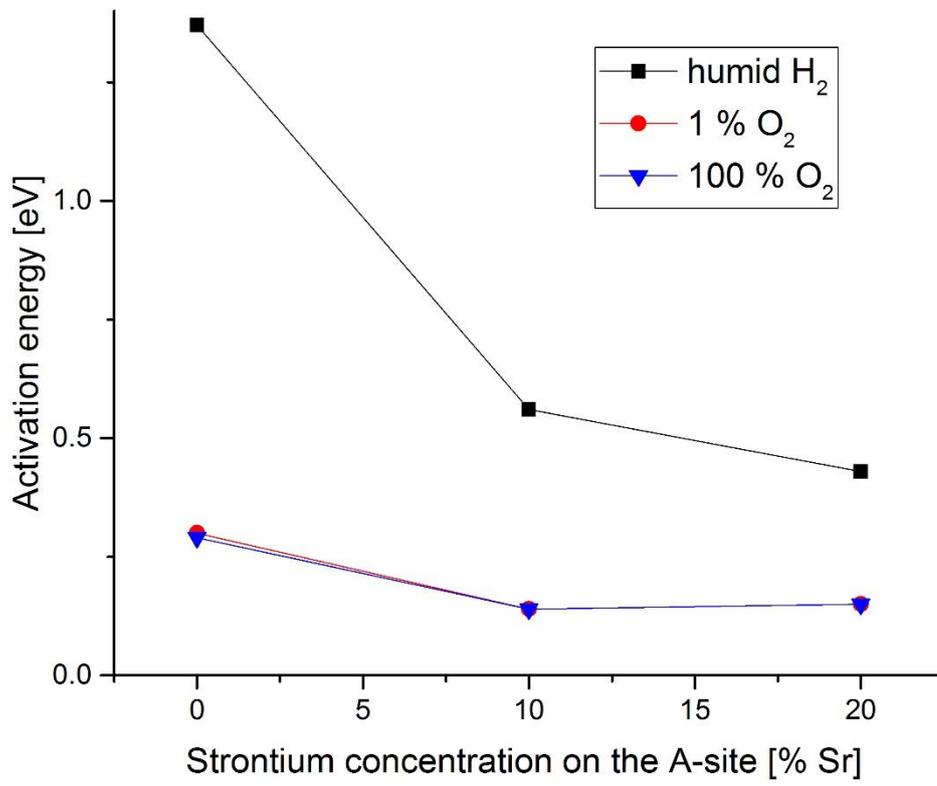
Figure 38: Activation energy versus Sr concentration for La$_{1-x}$Sr$_x$CrO$_{3-\delta}$ for different atmospheres at 810 °C.

4.3.2.2 Investigation of the effect of Sr-doping on $La_{1-x}Sr_xCr_{0.2}Mn_{0.8}O_{3-\delta}$

This measurement series is highlighted in blue in Figure 33.

Measurements in humid H_2

In Figure 39 the conductivities of $La_{1-x}Sr_xCr_{0.2}Mn_{0.8}O_{3-\delta}$ with different Sr concentrations in humid H_2 are plotted. The Sr concentrations inversely correlate with the conductivity. At 900 °C, the conductivity of the sample with 10 % Sr is one order of magnitude higher than the conductivity of the sample with 50 %. At lower temperatures, this gap is even wider, reaching about three orders of magnitude at 300 °C. For the whole measured temperature range, the difference in conductivity for the samples containing 40 % Sr and 50 % is one order of magnitude (e.g. conductivity at 900 °C: 10 S/cm for $La_{0.6}Sr_{0.4}Cr_{0.2}Mn_{0.8}O_{3-\delta}$; 1.2 S/cm for $La_{0.5}Sr_{0.5}Cr_{0.2}Mn_{0.8}O_{3-\delta}$). In contrast, the difference in conductivity for the samples with 10 % Sr and 20 % is less pronounced.

This wide range regarding the conductivity of the different compositions is also reflected in the activation energies in Figure 39. The different slopes are quite obvious to the eye. The two samples with the lower Sr concentrations exhibit, especially for higher temperatures, nearly temperature independent conductivities. A much steeper slope is observed for the samples with 40 % and 50 % Sr. The activation energy for $La_{0.9}Sr_{0.1}Cr_{0.2}Mn_{0.8}O_{3-\delta}$ is 0.18 eV, for $La_{0.8}Sr_{0.2}Cr_{0.2}Mn_{0.8}O_{3-\delta}$ it is 0.13 eV, for $La_{0.6}Sr_{0.4}Cr_{0.2}Mn_{0.8}O_{3-\delta}$ it is 0.36 eV and for $La_{0.5}Sr_{0.5}Cr_{0.2}Mn_{0.8}O_{3-\delta}$ it is 0.44 eV (see Figure 44 and Table 10).
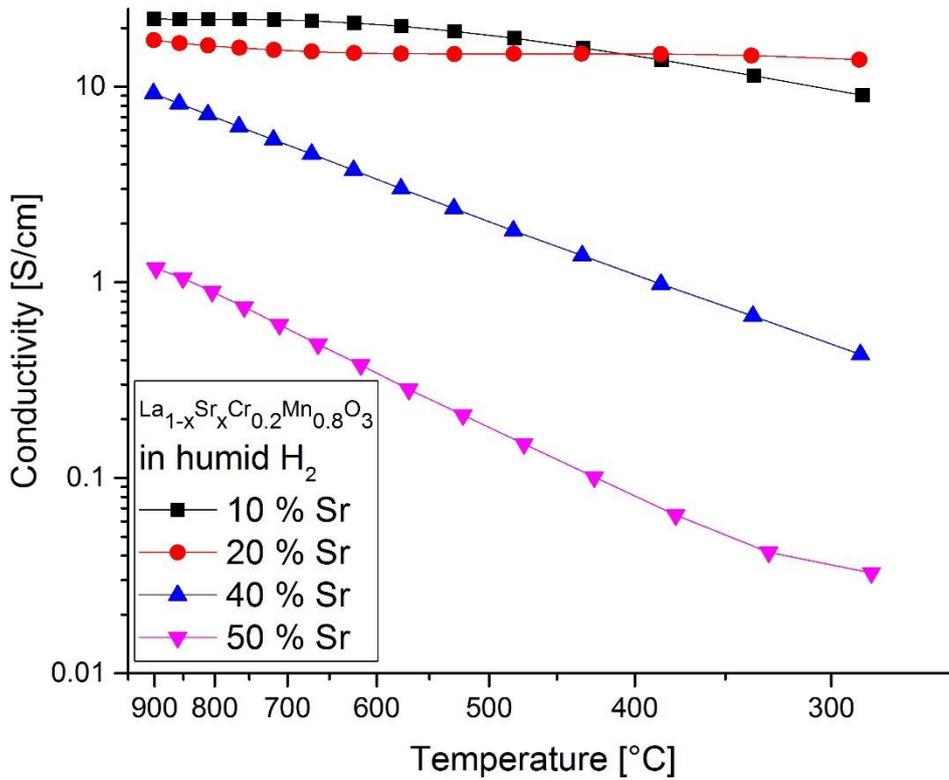
Figure 39: Arrhenius-type diagram of conductivity vs. temperature for La$_{1-x}$Sr$_x$Cr$_{0.2}$Mn$_{0.8}$O$_{3-\delta}$ in humid H$_2$ (see Table 5).

Measurements in 1 % O$_2$

While the conductivity under reducing atmospheres covers several orders of magnitude, the differences in the conductivity for the various compositions are much less pronounced under oxidizing atmospheres (cf. Figure 40). The highest observed conductivity in this measurement series was about 145 S/cm for La$_{0.6}$Sr$_{0.4}$Cr$_{0.2}$Mn$_{0.8}$O$_{3-\delta}$ at 900 °C, while the lowest conductivity of 57 S/cm at the same temperature was observed in La$_{0.9}$Sr$_{0.1}$Cr$_{0.2}$Mn$_{0.8}$O$_{3-\delta}$. An increase in conductivity can be observed when going to higher Sr dopant concentrations, reaching a maximum at 40 % Sr. At higher Sr concentrations, the conductivity decreases. For instance, the conductivities within the analyzed temperature range for La$_{0.5}$Sr$_{0.5}$Cr$_{0.2}$Mn$_{0.8}$O$_{3-\delta}$ are similar to those of La$_{0.8}$Sr$_{0.2}$Cr$_{0.2}$Mn$_{0.8}$O$_{3-\delta}$.

The activation energies are 0.18 eV for $La_{0.9}Sr_{0.1}Cr_{0.2}Mn_{0.8}O_{3-\delta}$, 0.16 eV for $La_{0.8}Sr_{0.2}Cr_{0.2}Mn_{0.8}O_{3-\delta}$ and 0.12 eV for $La_{0.6}Sr_{0.4}Cr_{0.2}Mn_{0.8}O_{3-\delta}$ and $La_{0.5}Sr_{0.5}Cr_{0.2}Mn_{0.8}O_{3-\delta}$ (see Figure 44 and Table 10).
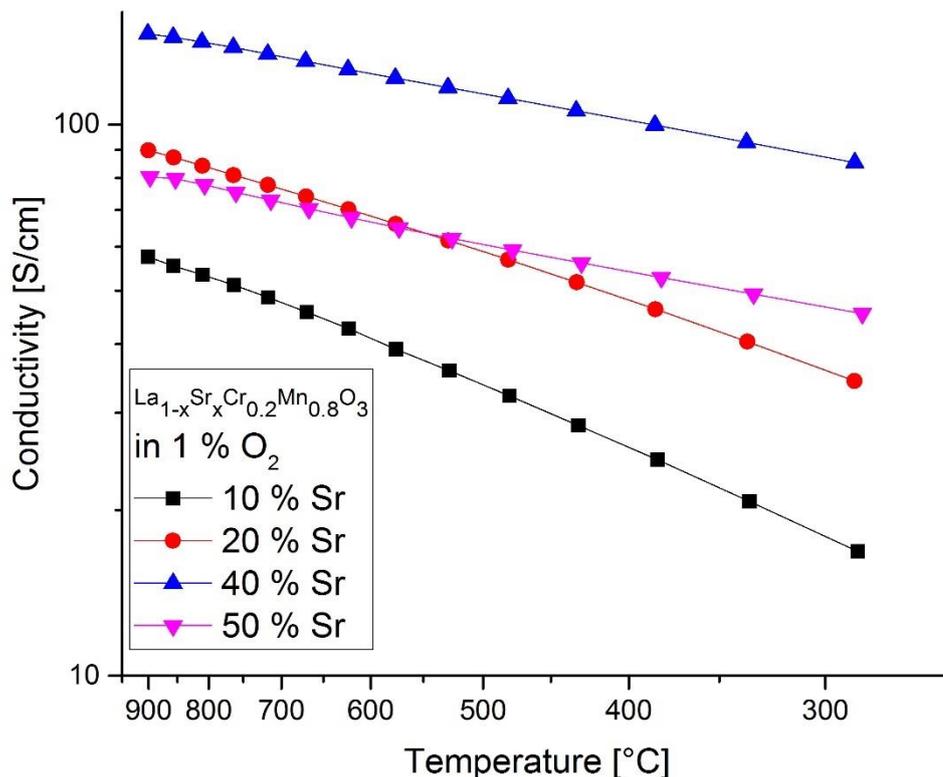
Figure 40: Arrhenius-type diagram of conductivity vs. temperature for $La_{1-x}Sr_xCr_{0.2}Mn_{0.8}O_{3-\delta}$ in 1 % O_2 (see Table 5).

Measurements in 100 % O_2

The results for this atmosphere are shown in Figure 41 and are quite similar to those in 1 % O_2. Again, the sample with the higher overall conductivities was $La_{0.6}Sr_{0.4}Cr_{0.2}Mn_{0.8}O_{3-\delta}$, starting at 85 S/cm at 285 °C and reaching 150 S/cm at 900 °C. Once more, the samples with 20 % Sr and 50 % Sr demonstrate quite similar conductivities.

The activation energies are 0.18 eV for $La_{0.9}Sr_{0.1}Cr_{0.2}Mn_{0.8}O_{3-\delta}$, 0.15 eV for $La_{0.8}Sr_{0.2}Cr_{0.2}Mn_{0.8}O_3$ and 0.12 eV for $La_{0.6}Sr_{0.4}Cr_{0.2}Mn_{0.8}O_{3-\delta}$ and $La_{0.5}Sr_{0.5}Cr_{0.2}Mn_{0.8}O_{3-\delta}$ (see Figure 44 and Table 10).
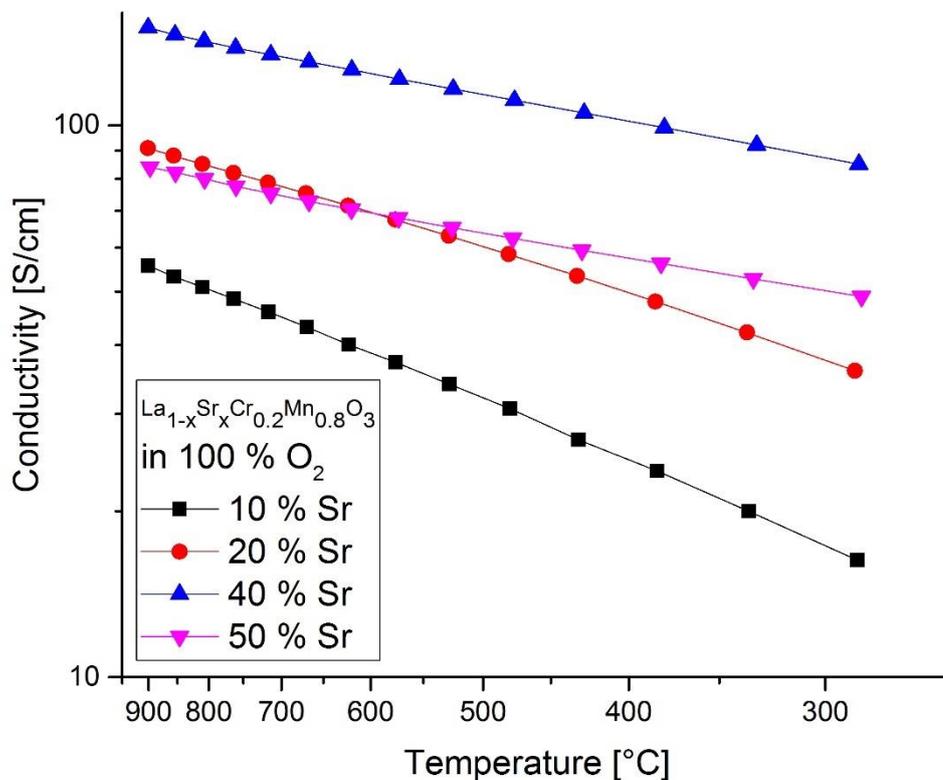
Figure 41: Arrhenius-type diagram of conductivity vs. temperature for La$_{1-x}$Sr$_x$Cr$_{0.2}$Mn$_{0.8}$O$_{3-\delta}$ in 100 % O$_2$ (see Table 5).

Discussion

The results for this measurement series differ from the previous results. The main difference is that Mn exhibits different chemical properties than Cr. For Mn, there are three different oxidation states which demonstrate similar stability. Therefore, the disproportionation of Mn^{3+} occurs to Mn^{2+} and Mn^{4+} [76]. When considering Mn^{4+} ions on Mn^{3+} sites, this is equivalent to an electron hole. Sr doping is thought to increase the amount of electron holes. However, the amount of charge carriers might not change when introducing Sr to LSCrM for higher Mn concentrations [26]. The observed increase of the conductivity in air might be explained by an increase in mobility.

This system is more complicated to analyze than $La_{1-x}Sr_xCrO_{3-\delta}$ due to the disproportion of the Mn^{3+}. Literature suggests that the amount of charge carriers is unaffected by Sr dopant concentration at higher Mn concentrations. It was reported in literature that, due to the disproportionation of Mn, Sr might not increase the amount of charge carriers (cf. Figure 42) [26, 77]. An increase in conductivity is therefore attributed to the mobility of the charge carriers.
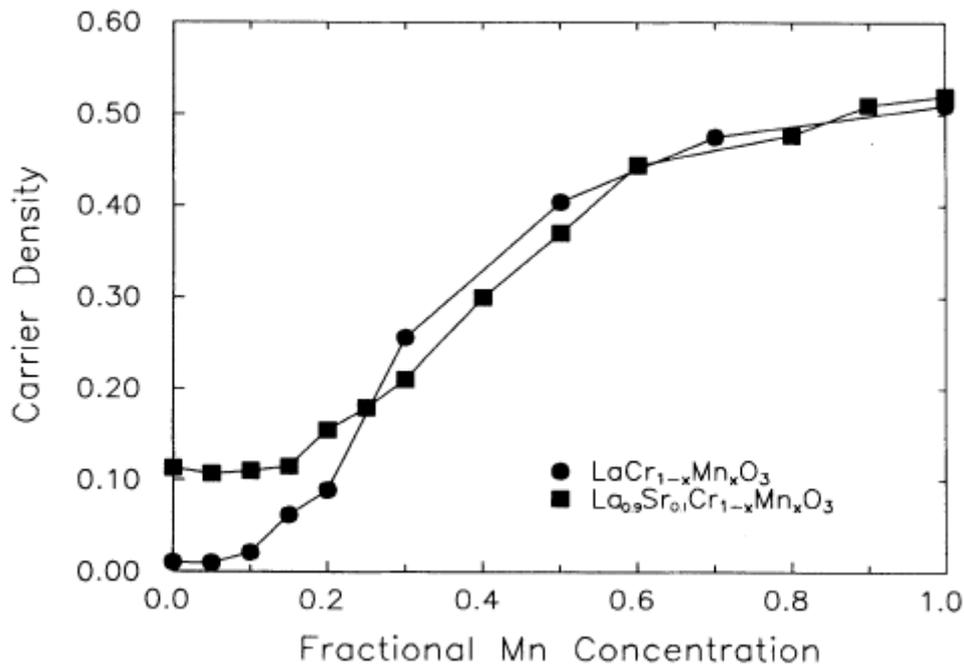
Figure 42: Carrier density at 1300 K versus fractional Mn concentration for undoped and 10 % Sr doped La(Cr,Mn)O₃; the charge carrier density was obtained from the Seebeck coefficient; the doped sample shows an increased carrier density only at low Mn concentrations; at about 25 % Mn there is no difference in the carrier density for the doped and the undoped material; however, the charge carrier density depends on the Mn concentration [26].

The increased mobility at higher Sr concentrations has been explained by a smaller radius of the Mn site, thus decreasing the Mn-Mn distance, due to the oxidation of Mn sites. In addition, the Mn-O-Mn angle gets closer to 180 °C. The increased mobility can be explained by a lower hopping energy [78, 79].

The very high Sr dopant concentrations of 40 % and 50 % Sr on the A-site might still have an effect on the amount of charge carriers, but in the samples with 10 % and 20 % Sr on the A-site the amount of charge carriers will be most likely be determined by the fixed amount of Mn. The Sr related increase in mobility can be observed under oxidizing atmospheres for Sr

dopant concentrations of 10 %, 20 % and 40 %. At higher Sr concentrations (50 %), the conductivity decreases, see Figure 43. This might be due to the high amount of Sr dopant concentration which has a negative relative charge, thus attracting the positively charged holes, leading to a localization of the polarons near to negatively charged Sr sites. This localization of electron holes would result in a decrease in mobility. However, as this system involves electron holes, the disproportionation of Mn^{3+}, oxygen vacancies and Sr'_{La}, an explanation might be more complex [26].

Under reducing conditions, the conductivity decreases when increasing the Sr concentration. This cannot be explained with p-type conductivity. As suggested in section 4.3.2.1, the conductivity might also be based on electrons. Using equations 4.5 and 4.6, a decrease in electrons can be seen for higher Sr concentrations. Assuming n-type conductivity, lowering the amount of electrons would decrease the conductivity, as it can be seen in Figure 43:

$$K = [V_O^{\bullet\bullet}] * [e']^2 \qquad\qquad (4.5)$$

with

$$[V_O^{\bullet\bullet}] = \frac{1}{2} * [Sr'_{La}] \qquad\qquad (4.6)$$

For the samples with 10 %, 20 % and 40 %, the decrease in conductivity is comparable to what could be expected from equations 4.5 and 4.6. However, the conductivity of the sample with 50 % Sr is one order of magnitude lower than the sample with 40 % in humid H_2. The respective conductivities are 22 S/cm for the sample with 10 % Sr, 16 S/cm for 20 % Sr, 7 S/cm for 40 % Sr and 0.9 S/cm for 50 % Sr. Variations from what could be expected from equations 4.5 and 4.6 might be due to changes in the mobility, which might depend on the Sr concentration [79]. An explanation for electrons as charge carriers might be the disproportionation of Mn^{3+}, resulting in Mn^{2+} and Mn^{4+} ions, which can be denoted as electrons or holes, respectively. Due to the high amount of Mn, there is already a high amount of charge carriers in the material, similar to a small bandgap semiconductor. The reducing atmosphere increases the amount of electrons, which could explain n-type conduction for these compositions in humid H_2 [26, 80].

The comparison of the conductivity for the different materials in this measurement series are shown in Figure 43.
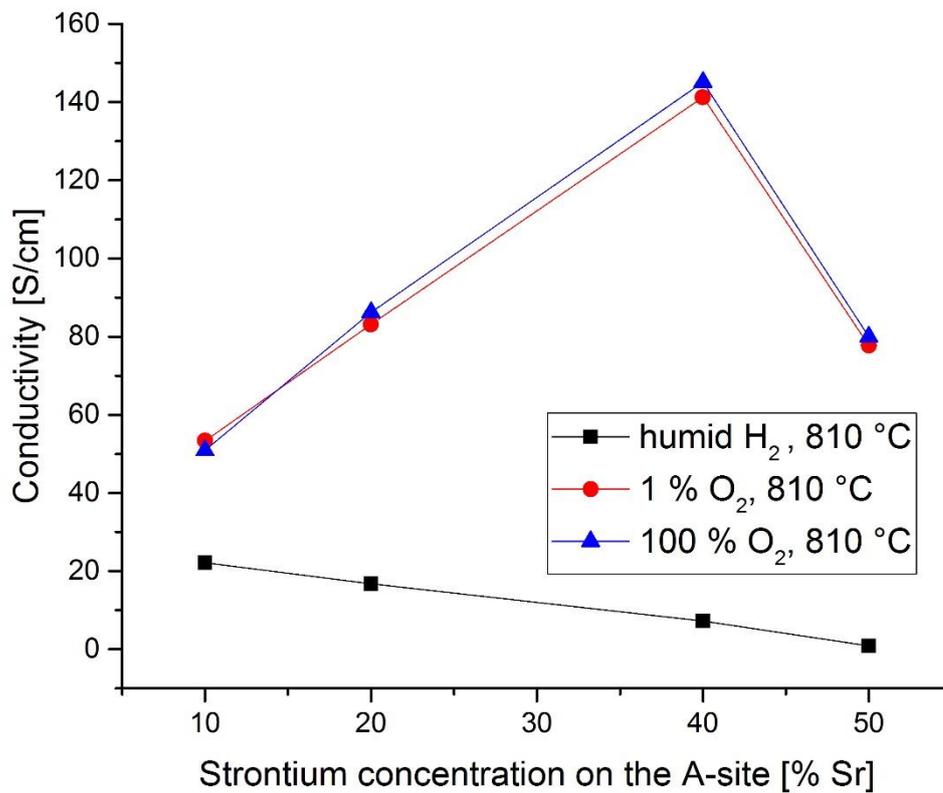
Figure 43: Conductivity versus Sr concentration for La$_{1-x}$Sr$_x$Cr$_{0.2}$Mn$_{0.8}$O$_{3-\delta}$ for different atmospheres at 810 °C.

These trends can also be observed when looking at the activation energies (see Figure 44). In humid H$_2$, higher Sr concentrations lead to higher activation energies. Higher activation energies are therefore found for compositions which exhibit lower electronic conductivities. Under reducing atmospheres, an increase in activation energy can be observed for increasing Sr concentration.
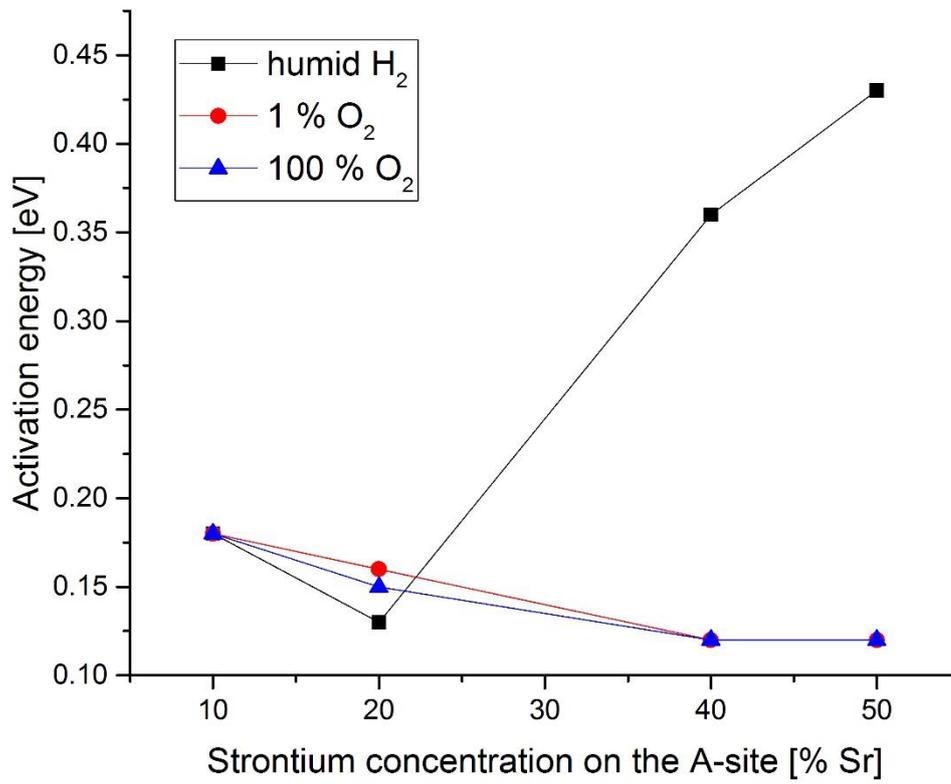
Figure 44: Activation energy versus Sr concentration for $La_{1-x}Sr_xCr_{0.2}Mn_{0.8}O_{3-\delta}$ for different atmospheres.

4.3.2.3 Investigation of the effect of varying the Cr:Mn ratio in $La_{0.9}Sr_{0.1}Cr_{1-x}Mn_xO_{3-\delta}$

In this measurement series, the amount of Sr dopant was kept constant at 10 % Sr. The samples used are highlighted in red in Figure 33. In theory, when mixing Cr and Mn on the B-site of the perovskite, Cr provides the stability under reducing conditions while Mn is electrochemically active [27]. Electron holes and oxygen vacancies are strongly associated with the valence state of Mn in these compositions, while Cr remains in its sixfold coordination state and trivalent oxidation state [81].

Therefore, it seems possible to tailor the requirements for an electrode materials, namely stability and conductivity, by changing the Cr:Mn ratio.

Measurements in humid H_2

The conductivities of the different $La_{0.9}Sr_{0.1}Cr_{1-x}Mn_xO_{3-\delta}$ compositions vary over a wide range, as can be seen in Figure 45. The conductivity changes by four orders of magnitude at 300 °C and nearly two orders of magnitude at 900 °C when varying the Mn content from 0 % to 80 % on the B-site. Overall, the lowest conductivities were obtained for the sample with 10 % Sr, starting at 10^{-3} S/cm at 300 °C and reaching 0.46 S/cm at 900 °C in humid H_2. With higher Mn concentrations, the conductivity also increased subsequently. The conductivity of $La_{0.9}Sr_{0.1}Cr_{0.85}Mn_{0.15}O_{3-\delta}$ is 10^{-3} S/cm at 300 °C and 0.69 S/cm at 900 °C. Two samples were prepared for the composition with 20 % Mn, conductivities of 0.78 S/cm and 1.17 S/cm were reached. Therefore, these compositions (10 % Mn, 15 % Mn, 20 % Mn) are not suitable as an anode since they do not meet the requirement of having at least a conductivity of 1 S/cm [47, 61]. The conductivity of $La_{0.9}Sr_{0.1}Cr_{0.65}Mn_{0.35}O_{3-\delta}$ is 0.04 S/cm at 300 °C and 1.29 S/cm at 900 °C. At 50% Mn doping the conductivity is comparable to the nominally undoped sample, resulting in a conductivity of 0.54 S/cm at 300 °C and 3.6 S/cm at 900 °C for the sample with 50 % Mn, compared to 0.34 S/cm at 300 °C and 4 S/cm at 900 °C for the sample without Mn. The highest conductivities in this measurement series were found in the sample with 80 % Mn, starting at 9 S/cm at 280 °C and going up to 22 S/cm a 900 °C.

The activation energies are 0.56 eV for the sample 0 % Mn, 0.61 eV for 10 % Mn as well as for 15 % Mn, 0.56 eV (0.55 eV for the second sample) for 20 % Mn, 0.38 eV for 35 % Mn, 0.24 eV for 50 % Mn and 0.18 eV for 80 % Mn (see Figure 49 and Table 10).
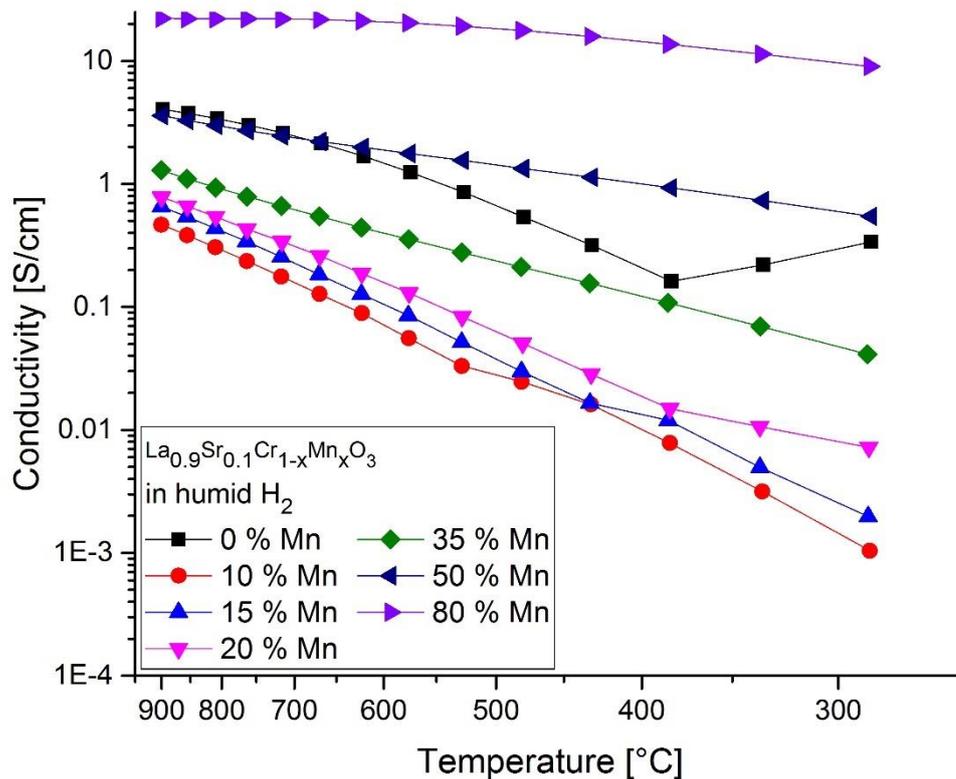
Figure 45: Arrhenius-type diagram of conductivity vs. temperature for $La_{0.9}Sr_{0.1}Cr_{1-x}Mn_xO_{3-\delta}$ in humid H_2 (see Table 5).

Measurements in 1 % O_2

The results for the measurements in 1% O_2 atmosphere are shown in Figure 46. Within the analyzed temperature range, the conductivity covers three orders of magnitude. The lowest conductivity was found in $La_{0.9}Sr_{0.1}Cr_{0.2}Mn_{0.8}O_{3-\delta}$, starting at 0.05 S/cm at 280 °C, reaching 4.4 S/cm at 900 °C. The highest conductivites in this measurement series were found in the sample with the highest Mn content, namely 80 % Mn, starting at 17 S/cm at 280 °C and reaching 57 S/cm at 900 °C. It is worth noting that the second highest conductivities were found in the sample containing no Mn.

The activation energies are 0.14 eV for the sample 0 % Mn, 0.28 eV for 10 % Mn, 0.35 eV for 15 % Mn, 0.51 eV (0.45 eV for the second sample) for 20 % Mn, 0.4 eV for 35 % Mn, 0.28 eV for 50 % Mn and 0.18 eV for 80 % Mn (see Figure 49 and Table 10).
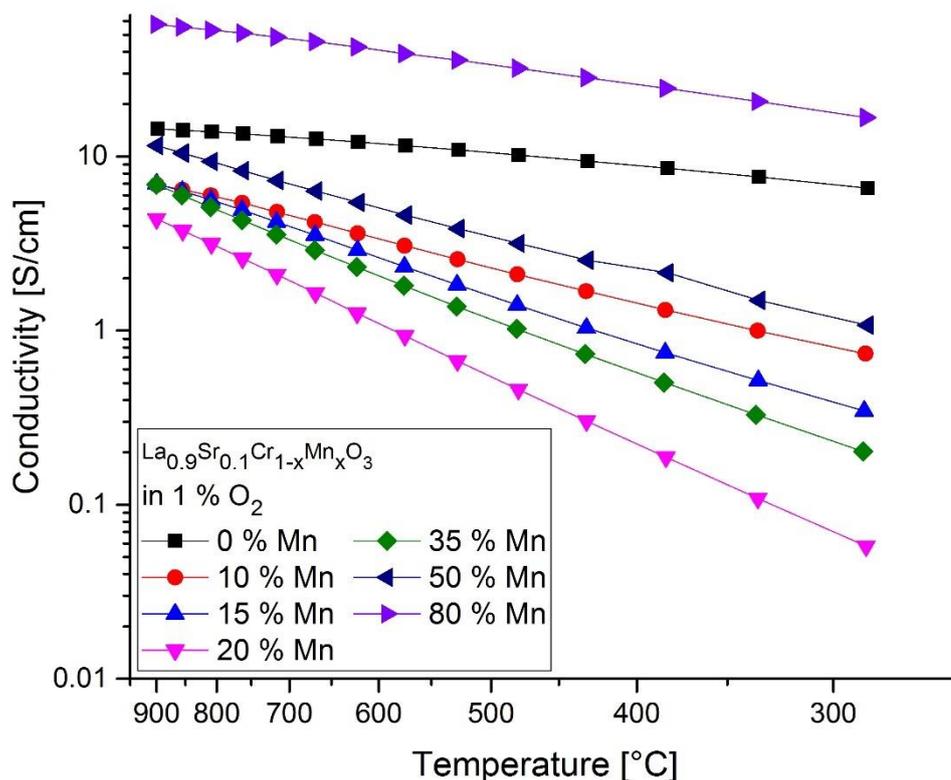
Figure 46: Arrhenius-type diagram of conductivity vs. temperature for La$_{0.9}$Sr$_{0.1}$Cr$_{1-x}$MnxO$_{3-\delta}$ in 1 % O$_2$ (see Table 5).

Measurements in 100 % O₂

Again, the observed conductivities within the analyzed temperature range are within three orders of magnitude (see Figure 47). The results for the 100 % O₂ atmosphere are quite similar to what was observed under 1 % O₂. The lowest conductivities were observed in the sample with 20 % Mn. The samples with 10 % Mn – 35 % Mn demonstrate, however, a similarly low

conductivity. The highest conductivity was obtained for $La_{0.9}Sr_{0.1}Cr_{0.2}Mn_{0.8}O_3$, the sample with the highest Mn concentration, followed by the second highest conductivity for $La_{0.9}Sr_{0.1}CrO_3$.

The activation energies are 0.14 eV for the sample 0 % Mn, 0.3 eV for 10 % Mn, 0.37 eV for 15 % Mn, 0.47 eV (0.45 eV for the second sample) for 20 % Mn, 0.4 eV for 35 % Mn, 0.27 eV for 50 % Mn and 0.18 eV for 80 % Mn (see Figure 49 and Table 10).
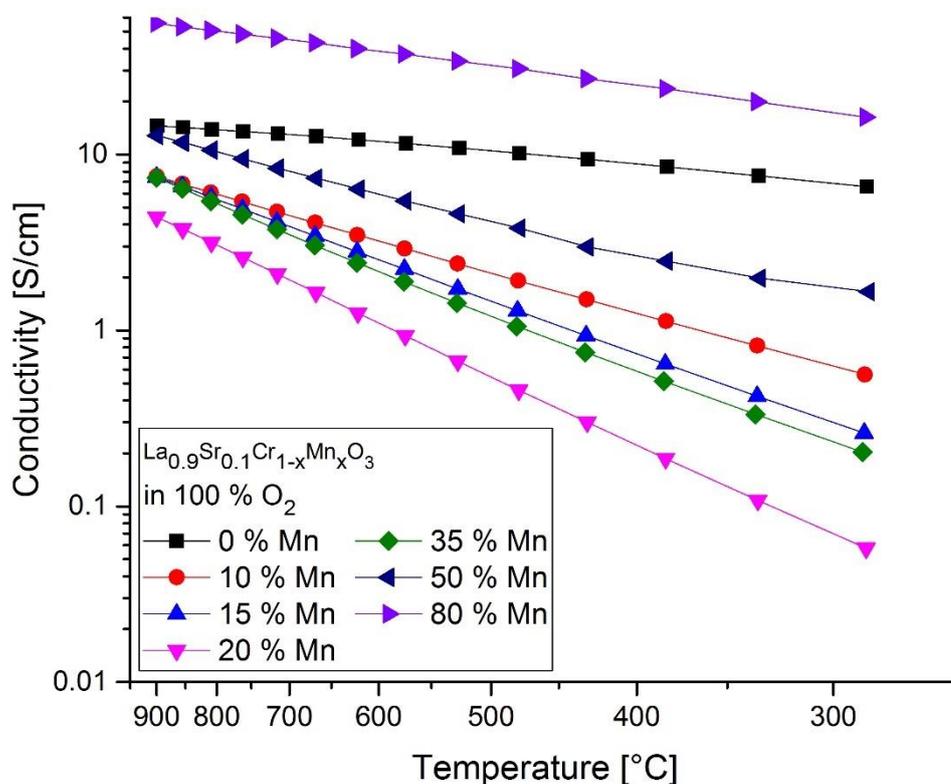
Figure 47: Arrhenius-type diagram of conductivity vs. temperature for $La_{0.9}Sr_{0.1}Cr_{1-x}Mn_xO_{3-\delta}$ in 100 % O_2 (see Table 5).

Discussion

The comparison for this measurement series is shown in Figure 48 for the conductivities at 810 °C and in Figure 49 for the activation energies. When plotting the conductivity versus the amount of Mn on the B site of the lattice, a minimum can be seen at 10 % - 20 % Mn. The

trend is largely independent of the atmosphere, starting at LSCr the conductivity drops about one order of magnitude and then rises with increasing Mn concentration. The minimum in humid H_2 is at about 10 % Mn, in oxidizing atmospheres at about 20 % Mn, the main difference between the different atmospheres is therefore the extent and location of the minimum.

There are two major factors, which influence the conductivity in LSCrM, see equation 2.1. On the one hand, there is the concentration of the charge carriers. The depencency of the charge carriers on the temperature can be explained by trapping, which lowers the amount of charge carriers, as well as the incorporation or excorporation oxygen, depending on the oxygen partial pressure. On the other hand, the mobility of the charge carriers also depends on the temperature.

The activation energies reach a maximum at 10 % - 20 % Mn, showing again a slight shift between reducing and oxidizing conditions. There seems to be a correlation between higher conductivities and lower activation energies, and vice versa.
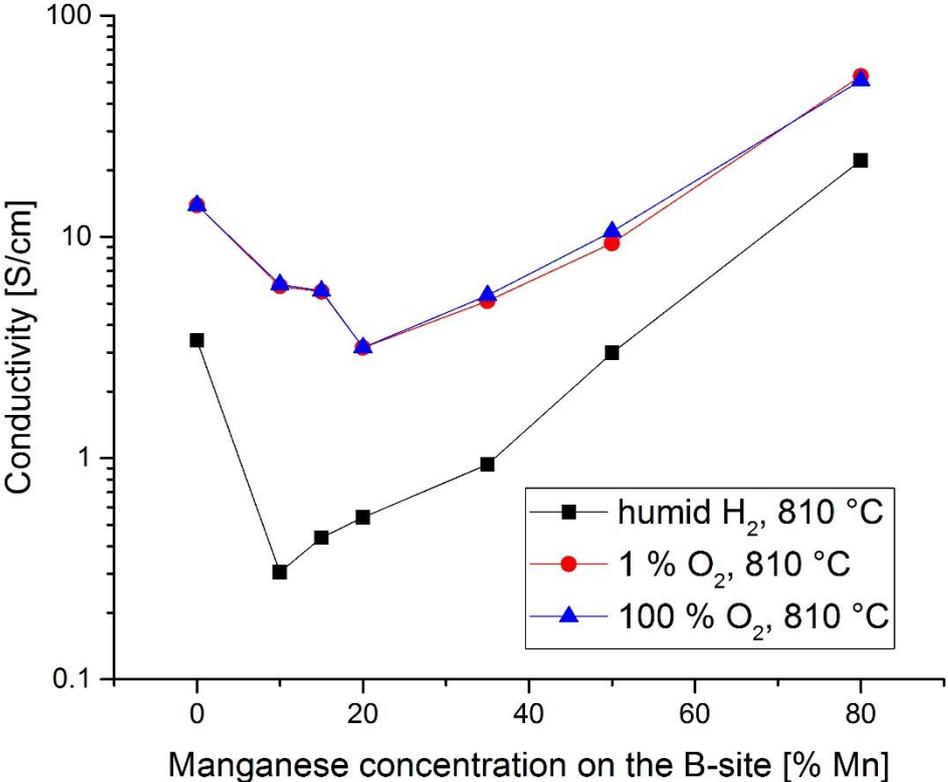
Figure 48: Conductivity vs. Mn concentration for $La_{0.9}Sr_{0.1}Cr_{1-x}Mn_xO_{3-\delta}$ for different atmospheres at 810 °C.
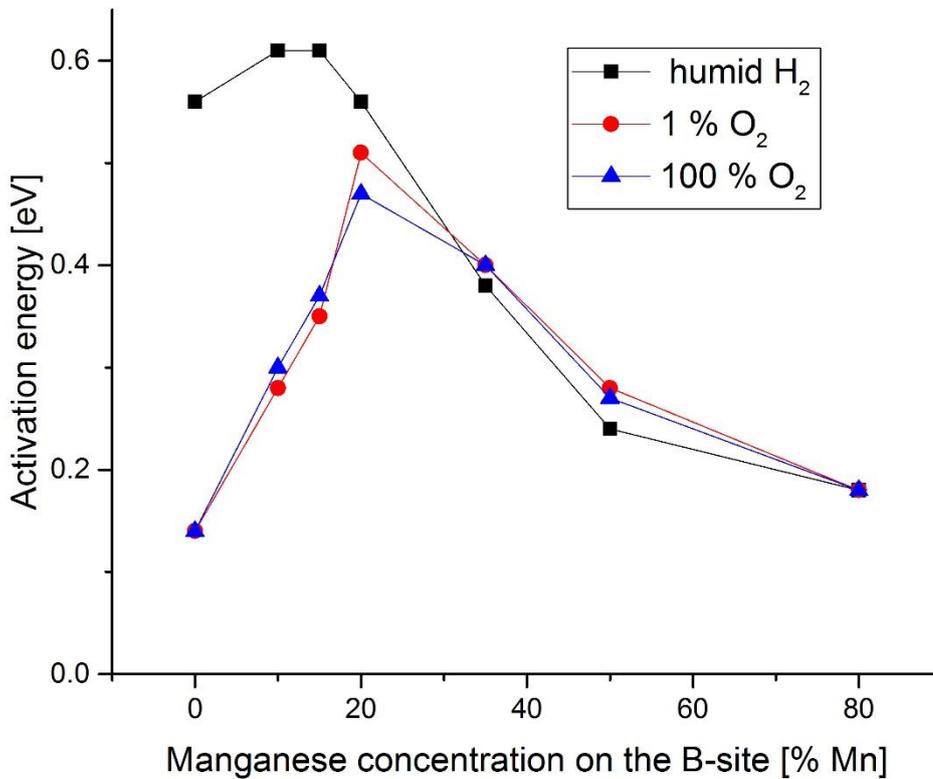
Figure 49: Activation energy vs. Mn concentration for $La_{0.9}Sr_{0.1}Cr_{1-x}Mn_xO_{3-\delta}$ for different atmospheres.

A phenomenological explanation can be used to illustrate the trends for the activation energy (see Figure 50). The Mn sites are energetically lower than the Cr sites [26]. When introducing low amounts of Mn in LSCr, the charge carrying polarons are trapped on these energetically lower Mn sites ("random well"), thus reducing the conductivity of the material [26]. Upon increasing the Mn concentration, percolation of the trapping levels occurs, thereby enabling electron hole transport from one Mn site to another, i.e. the formation of a new band occurs [26, 77]. Due to this percolation, the conductivity increases.

On a side note, the different amount of charge carriers for different compositions in this measurement series should be pointed out. While one could assume that the amount of charge carriers is constant due to the fixed Sr dopant concentration, it has been suggested that the amount of charge carriers might depend more on the Cr:Mn ratio than on the Sr

concentration (cf. Figure 42) [26]. While an increase in conductivity with Sr can be observed, this is attributed to the increased mobility [78, 79]. In this measurement series with a varying Cr:Mn ratio and a fixed Sr dopant concentration, the amount of charge carriers increases with higher Mn concentration.
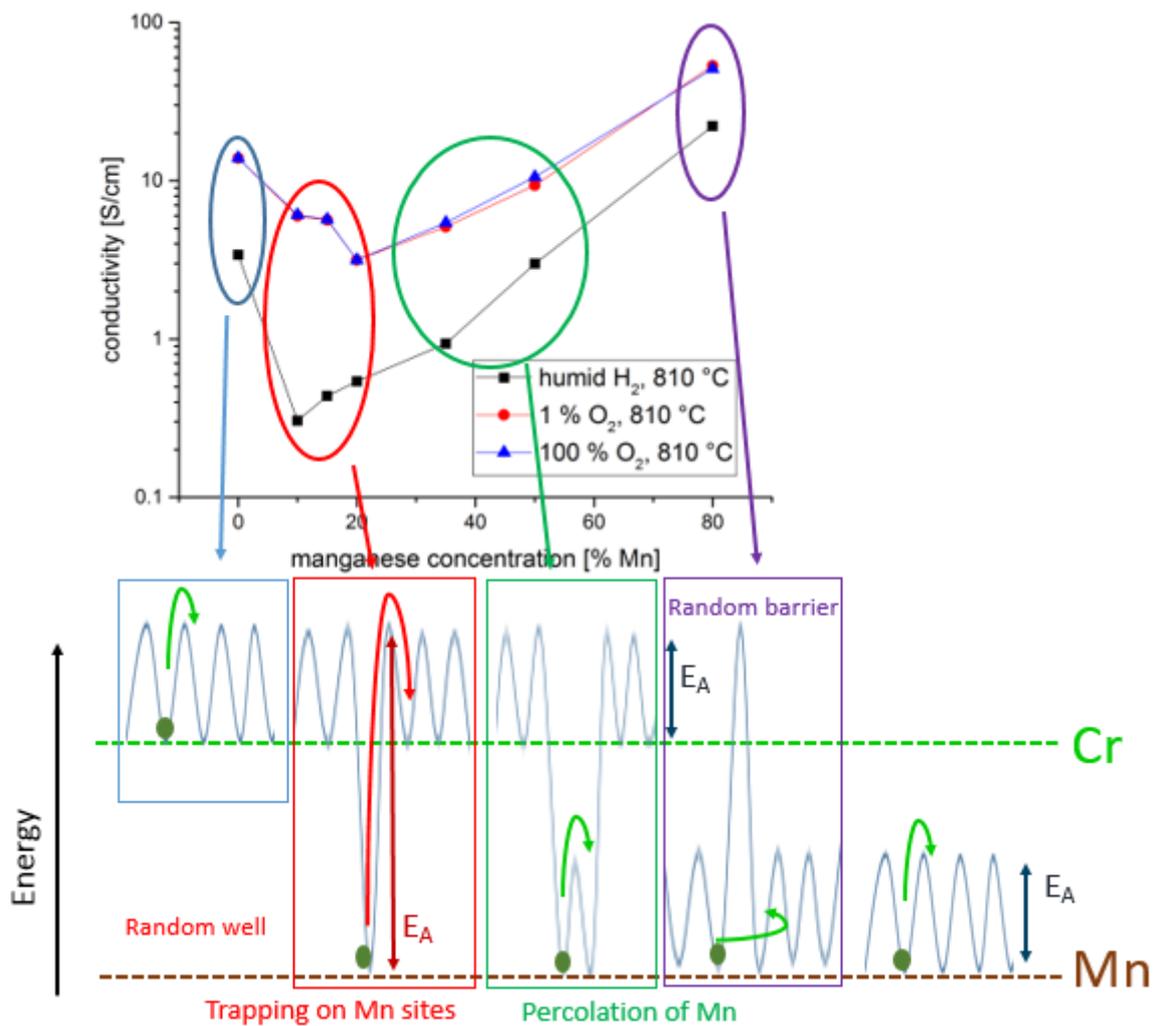
Figure 50: Schematic explanation for the minimum in conductivity in $La_{0.9}Sr_{0.1}Cr_{1-x}Mn_xO_{3-\delta}$ due to trapping on energetically lower Mn sites; the rise in conductivity can be explained by percolation of Mn sites.

For bulk samples, values between 1 S/cm at the minimum and 80 S/cm at 80 % Mn can be found [26]. In addition, the same trend can be seen for bulk samples. The measured conductivities are, therefore, in good agreement with bulk conductivities of LSCrM.
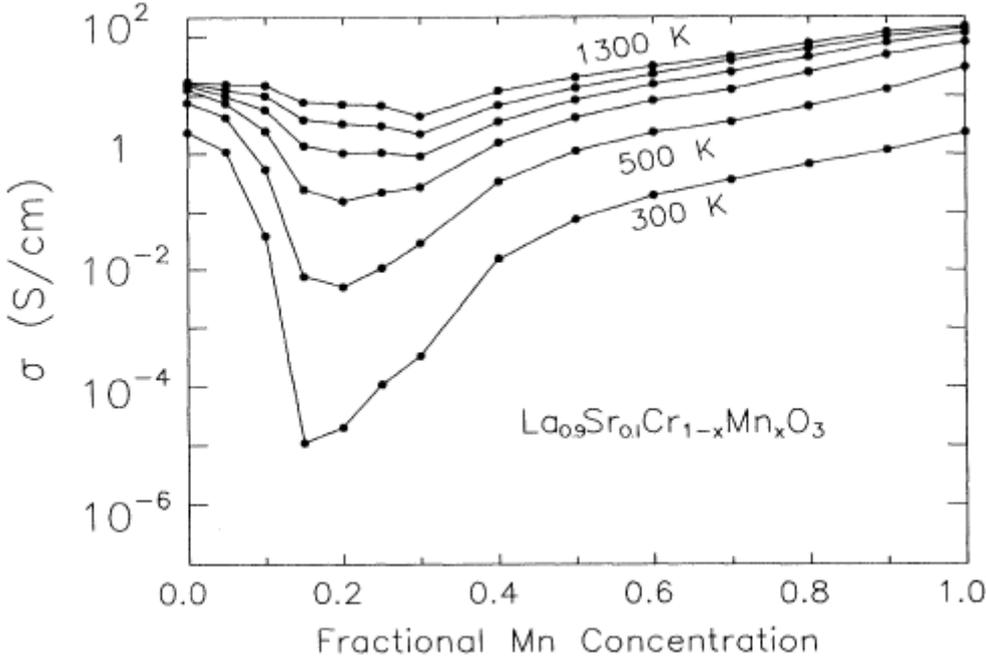
Figure 51: Bulk conductivities of $La_{0.9}Sr_{0.1}Cr_{1-x}Mn_xO_3$ for different temperatures [26].

4.3.3 Table of the measured activation energies

The activation energies measured in this work are shown in Table 10. The activation energies were obtained from $\log(\sigma T)$ vs. $1/T$ Arrhenius plot (see section 2.2.2).

Table 10: Activation energies for different LSCrM compositions in different atmospheres and deposited on different substrates

Material	E_A [eV] in			Substrate
	humid H_2	*1 % O_2*	*100 % O_2*	
$LaCrO_{3-\delta}$	1.37	0.30	0.29	MgO
$La_{0.9}Sr_{0.1}CrO_{3-\delta}$	0.56	0.14	0.14	MgO
$La_{0.8}Sr_{0.2}CrO_{3-\delta}$ (290 °C – 570 °C)	0.71	0.15	0.15	MgO
$La_{0.8}Sr_{0.2}CrO_{3-\delta}$ (620 °C – 900 °C)	0.43			
$La_{0.9}Sr_{0.1}Cr_{0.9}Mn_{0.1}O_{3-\delta}$	0.61	0.28	0.30	MgO
$La_{0.9}Sr_{0.1}Cr_{0.85}Mn_{0.15}O_{3-\delta}$	0.61	0.35	0.37	MgO
$La_{0.9}Sr_{0.1}Cr_{0.8}Mn_{0.2}O_{3-\delta}$	0.56	0.51	0.47	MgO
$La_{0.9}Sr_{0.1}Cr_{0.8}Mn_{0.2}O_{3-\delta}$	0.55	0.45	0.45	MgO
$La_{0.9}Sr_{0.1}Cr_{0.8}Mn_{0.2}O_{3-\delta}$	0.55	0.49	0.48	Al_2O_3
$La_{0.9}Sr_{0.1}Cr_{0.65}Mn_{0.35}O_{3-\delta}$	0.28	0.40	0.40	MgO
$La_{0.9}Sr_{0.1}Cr_{0.5}Mn_{0.5}O_{3-\delta}$	0.24	0.28	0.27	MgO
$La_{0.9}Sr_{0.1}Cr_{0.2}Mn_{0.8}O_{3-\delta}$	0.18	0.18	0.18	MgO
$La_{0.9}Sr_{0.1}Cr_{0.2}Mn_{0.8}O_{3-\delta}$ (deposition T: 550 °C)	0.35	0.19	0.18	Al_2O_3
$La_{0.9}Sr_{0.1}Cr_{0.2}Mn_{0.8}O_{3-\delta}$	0.25	0.18	0.16	Al_2O_3
$La_{0.9}Sr_{0.1}Cr_{0.2}Mn_{0.8}O_{3-\delta}$	0.18	0.18	0.18	LAO
$La_{0.8}Sr_{0.2}Cr_{0.2}Mn_{0.8}O_{3-\delta}$	0.13	0.16	0.15	MgO
$La_{0.6}Sr_{0.4}Cr_{0.2}Mn_{0.8}O_{3-\delta}$	0.36	0.12	0.12	MgO
$La_{0.5}Sr_{0.5}Cr_{0.2}Mn_{0.8}O_{3-\delta}$	0.43	0.12	0.12	MgO
$La_{0.5}Sr_{0.5}Cr_{0.2}Mn_{0.8}O_{3-\delta}$	0.44	0.10	0.10	LAO

4.4 Impedance spectroscopy

Impedance spectroscopy was used in this work to determine the electrochemical surface polarization resistance of $La_{0.9}Sr_{0.1}Cr_{1-x}Mn_xO_{3-\delta}$ for x = 0, 0.1, 0.35 and 0.8 (see Figure 33). When plotting the obtained data of a cell with $La_{0.9}Sr_{0.1}Cr_{1-x}Mn_xO_{3-\delta}$ as thin film working electrode on YSZ and Ni/YSZ as a counter electrode (see Figure 21) in a Nyquist plot, two semicircles are obtained. By fitting the data with an equivalent circuit diagram, the capacitances and the resistances are obtained (see Figure 52 and Figure 53 as well as section 2.8).
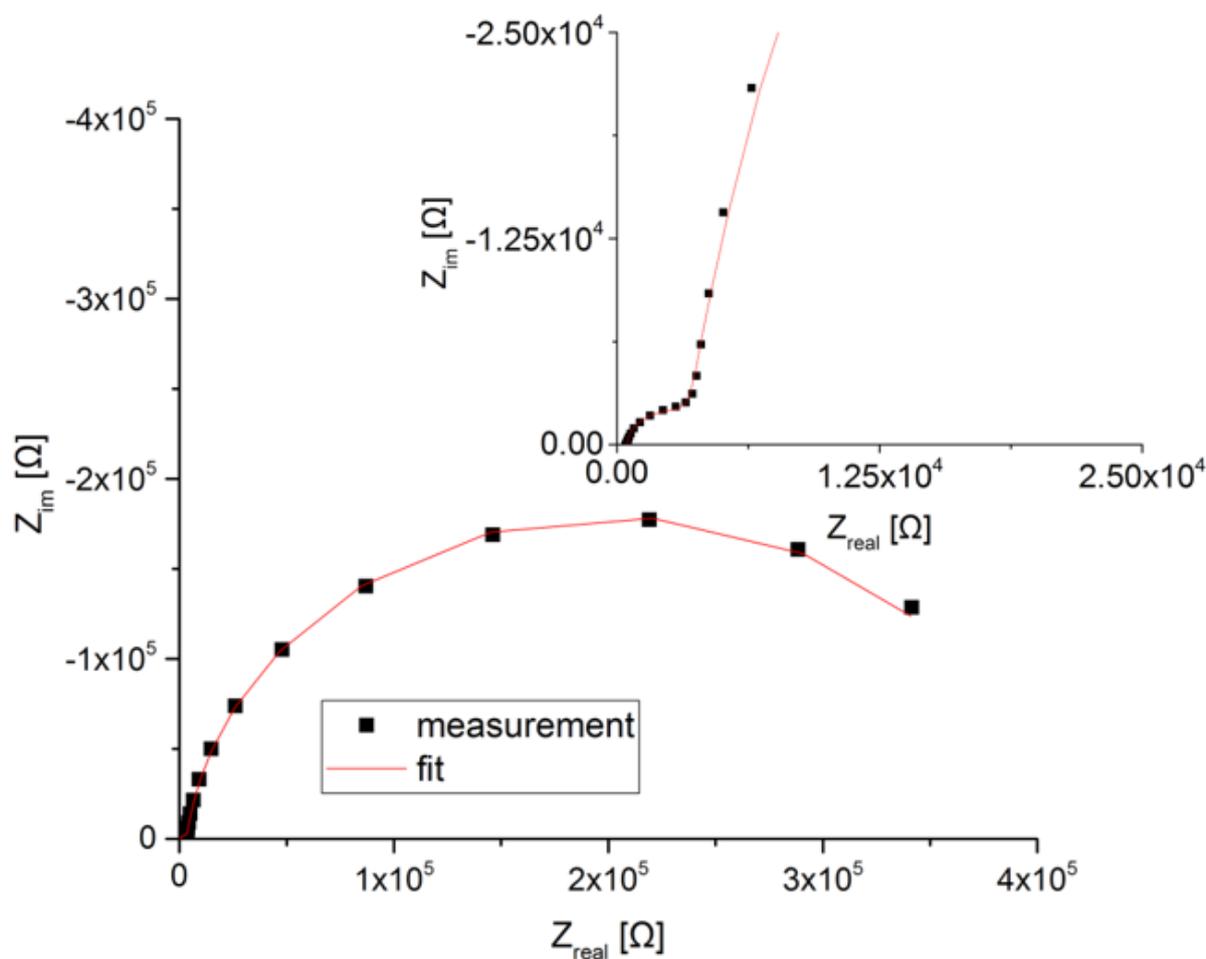
Figure 52: Measurement data of $La_{0.9}Sr_{0.1}Cr_{0.9}Mn_{0.1}O_{3-\delta}$ at 813 °C in humid H_2 and fit results (circuit in Figure 53); the high frequency section is shown in the magnification.

In case of a MIEC with surface limitations, the resistances might correspond to the interface and the surface incorporation, respectively (cf. Figure 17). However, as the variation of the electrode surface area was not investigated, no statement can be made regarding the mechanism. Therefore, the equivalent circuit as shown in Figure 53 was chosen for data analysis. By adding these two resistances, the electrode polarization resistance is obtained.
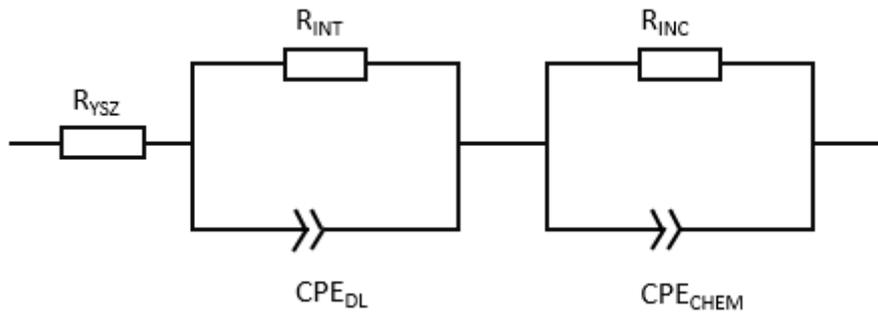
Figure 53: Equivalent circuit used for the data evaluation.

$$R_{elect.pol.} = R_{INT} + R_{INC} \qquad (4.7)$$

The electrochemical polarization resistance was extracted for different LSCrM compositions, which are shown in Figure 33.

Higher temperatures lead to a decrease of all resistances, see Figure 54. This is due to the improved conductivity (e.g. R_{YSZ}) as well as due to the improved electrode kinetics ($R_{elect.pol.}$).
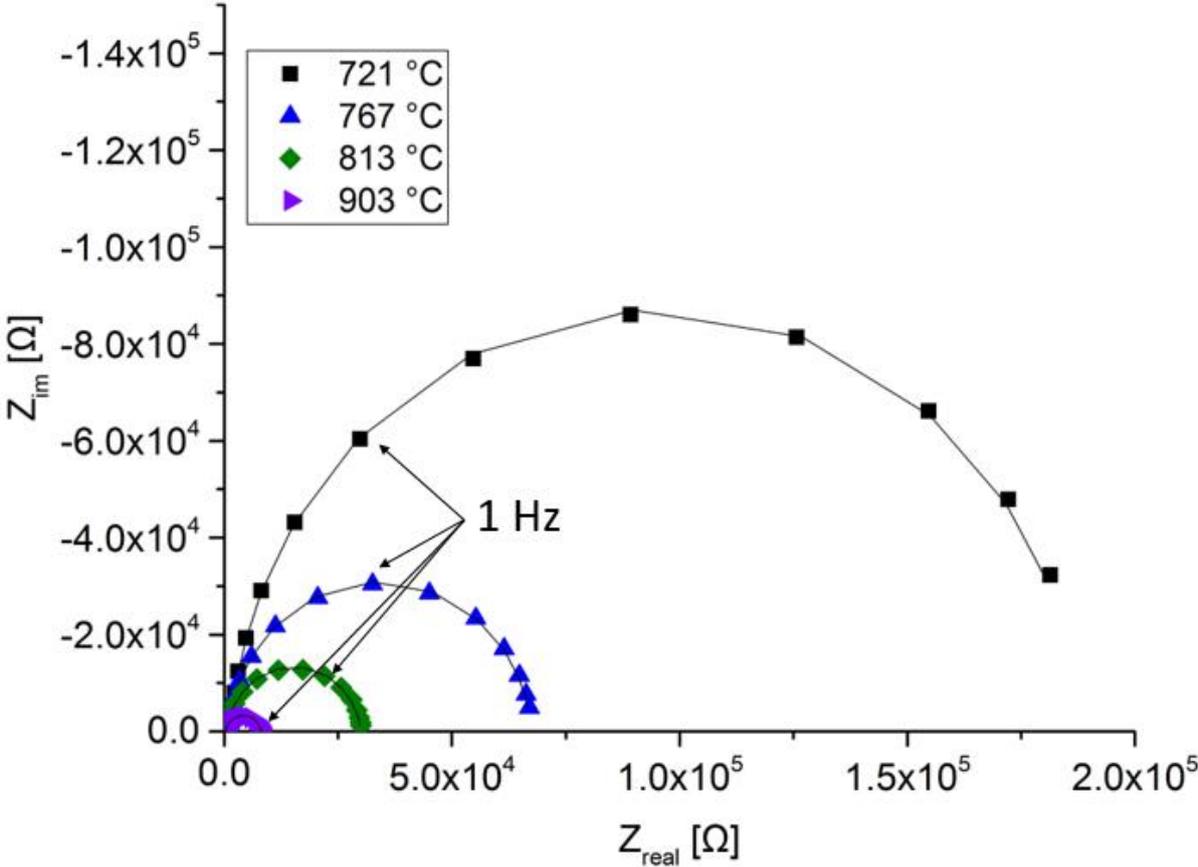
Figure 54: Comparison of impedance spectra measured in humid H_2 at different temperatures showing the effect of the temperature on the impedance spectra of $La_{0.9}Sr_{0.1}Cr_{0.2}Mn_{0.8}O_{3-\delta}$.

Impedance spectra measured at 813°C for the selected compositions are shown in Figure 55. $La_{0.9}Sr_{0.1}Cr_{0.2}Mn_{0.8}O_{3-\delta}$ shows by far the lowest electrode polarization resistance.
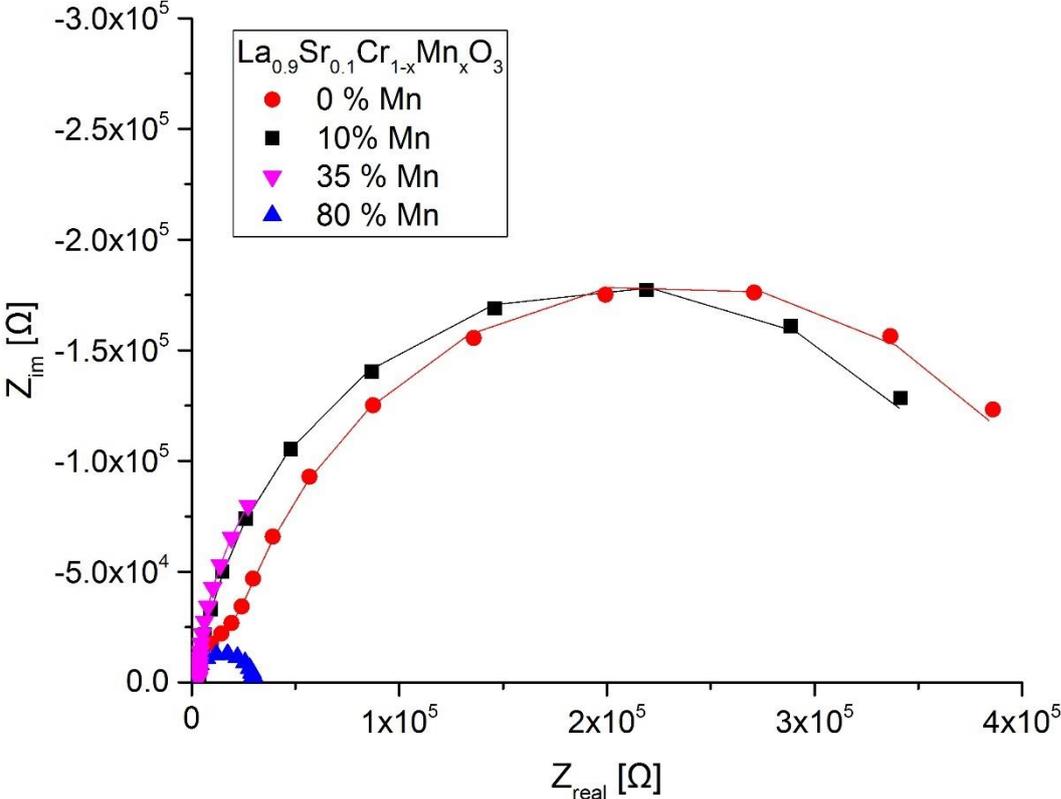
Figure 55: Comparison of the impedance spectra for different materials in humid H_2 at 813 °C.

4.4.1 Electrode polarization resistance in humid H_2

The area specific electrode resistance calculated for each material can be shown in an Arrhenius plot (see Figure 56). Only the area without Pt beneath was used for normalization (see Figure 21). This can be done under the assumption that the ionic conductivity is low; otherwise the electrode polarization resistance is four times as high [82]. The corresponding activation energies are summarized in Table 11.
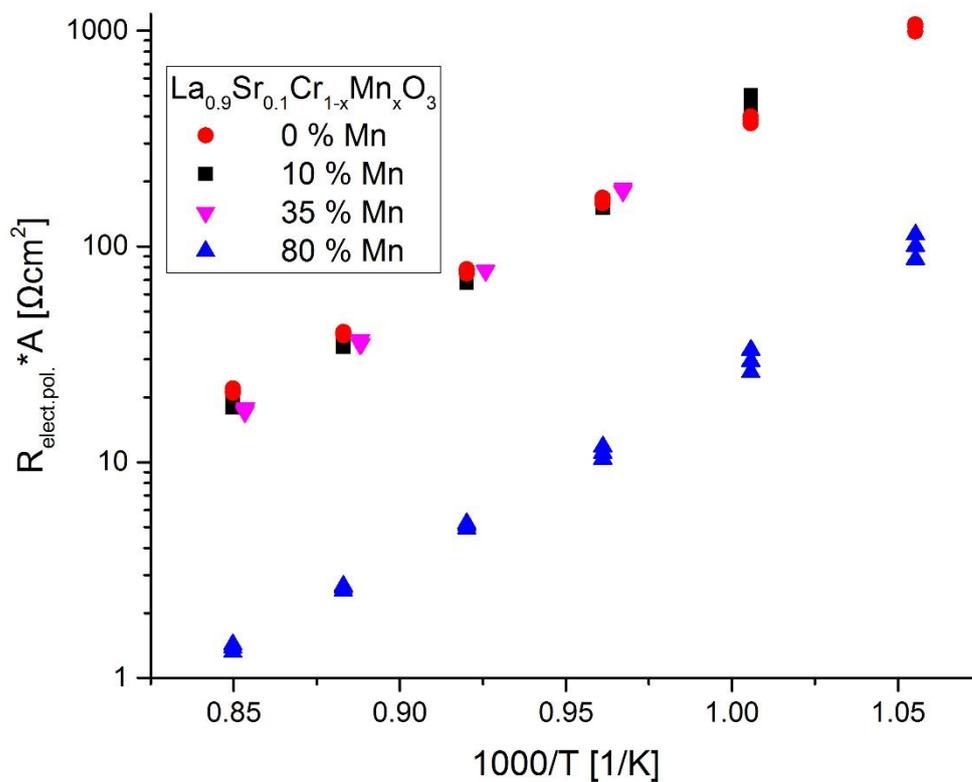
Figure 56: Arrhenius plot for the electrochemical electrode polarization resistance for different materials in humid H_2.

Table 11: Activation energies for the polarization resistance for different materials in humid H_2.

Composition	Activation energy [eV]
$La_{0.9}Sr_{0.1}CrO_{3-\delta}$	1.62
$La_{0.9}Sr_{0.1}Cr_{0.9}Mn_{0.1}O_{3-\delta}$	1.77
$La_{0.9}Sr_{0.1}Cr_{0.65}Mn_{0.35}O_{3-\delta}$	1.77
$La_{0.9}Sr_{0.1}Cr_{0.2}Mn_{0.8}O_{3-\delta}$	1.77

When comparing the polarization resistances of the different materials (see Figure 56), the rather low electrode polarization resistance of $La_{0.9}Sr_{0.1}Cr_{0.2}Mn_{0.8}O_{3-\delta}$ is worth mentioning. It is about one order of magnitude lower than for the other materials that were investigated in this study.

Electrode polarization resistances for other materials reported in literature are shown in Table 12.

Table 12: Electrode polarization resistances for different materials in humid H_2.

Material	Temperature [°C]	$R_{elect.pol.}$ [Ωcm^2]	Reference
$Sm_{0.2}Ce_{0.8}O_{1.9-\delta}$	650	20	[54]
$La_{0.6}Sr_{0.4}FeO_{3-\delta}$	668	5	[83]
$SrTi_{0.7}Fe_{0.3}O_3$	800	20	[84]
$SrTi_{0.3}Fe_{0.7}O_3$	800	7	[84]

The electrode polarization resistance for $La_{0.9}Sr_{0.1}Cr_{0.2}Mn_{0.8}O_{3-\delta}$ is about 100 Ωcm^2 at 674 °C in humid H_2. At 813 °C, the electrode polarization resistance of $La_{0.9}Sr_{0.1}Cr_{0.2}Mn_{0.8}O_{3-\delta}$ is about 5 Ωcm^2. Therefore, the electrode polarization resistances measured for $La_{0.9}Sr_{0.1}Cr_{0.2}Mn_{0.8}O_{3-\delta}$ are well within the range of other materials reported in literature.

4.4.2 Electrode polarization resistance in 100 % O_2

The electrode polarization resistances for different compositions are shown in Figure 57. As opposed to Figure 56, the difference between the individual compositions is much lower. This could again be explained by oxygen vacancies. In oxidizing atmospheres, the oxygen vacancies are filled up, lowering the ionic conductivity and probably also the oxygen exchange activity of the surface. The amount of Mn does not necessarily increase the amount of oxygen vacancies, which results in an equally low ionic conductivity for the different LSCrM compositions.
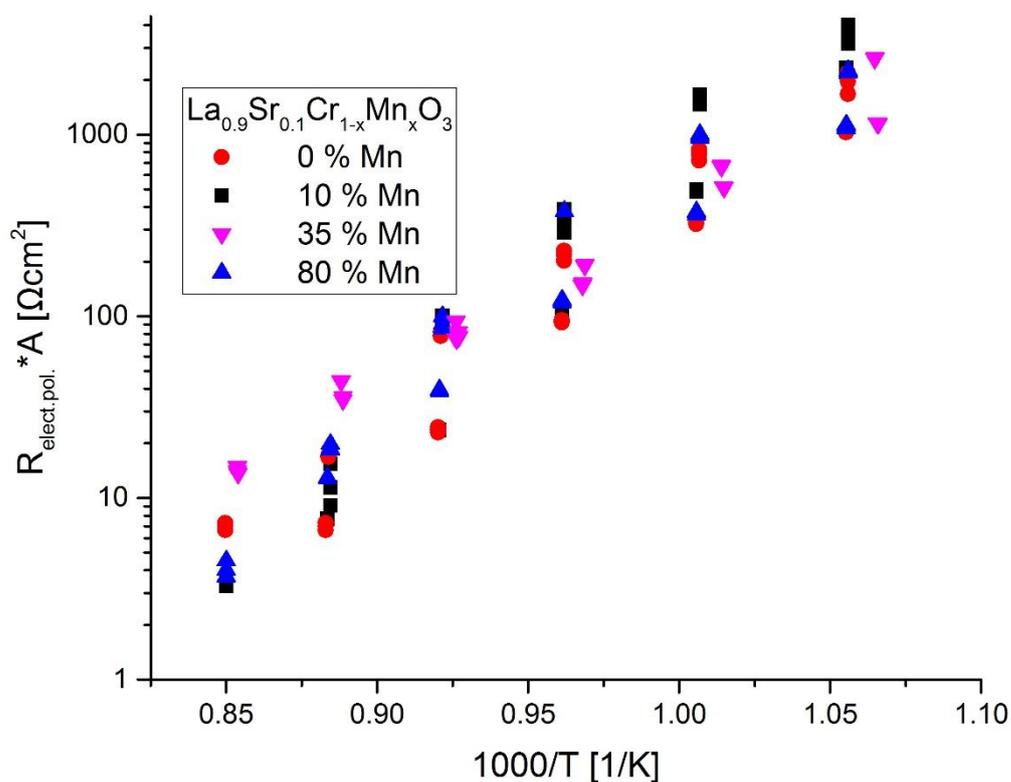
Figure 57: Arrhenius plot for the electrochemical electrode polarization resistance for different materials in 100 % O_2.

For $La_{0.8}Sr_{0.2}MnO_3$, the electrode resistances are about 58 Ωcm^2 at 800 °C [71]. In comparison, the electrode polarization resistances for different LSCrM compositions are between 22 Ωcm^2 and 90 Ωcm^2 at 813 °C.

The activation energies are shown in Table 13.

Table 13: Activation energies for the polarization resistance for different materials in 100 % O_2.

Composition	Activation energy [eV]
$La_{0.9}Sr_{0.1}CrO_{3-\delta}$	2.29
$La_{0.9}Sr_{0.1}Cr_{0.9}Mn_{0.1}O_{3-\delta}$	2.82
$La_{0.9}Sr_{0.1}Cr_{0.65}Mn_{0.35}O_{3-\delta}$	2.05
$La_{0.9}Sr_{0.1}Cr_{0.2}Mn_{0.8}O_{3-\delta}$	2.33

4.5 Comparison between the Van-der-Pauw measurements and the EIS measurements

4.5.1 Measurements in humid H_2

For the measurement series with a variation of the Cr:Mn ratio, the electronic as well as the electrochemical properties can be compared (see Figure 58). When the electrode polarization resistance is compared with the total conductivity of a material, no clear trend can be seen. $La_{0.9}Sr_{0.1}CrO_{3-\delta}$ has a one order of magnitude higher conductivity than $La_{0.9}Sr_{0.1}Cr_{0.9}Mn_{0.1}O_{3-\delta}$, but the polarization resistance is the same for both materials. In contrast to this, the conductivity of $La_{0.9}Sr_{0.1}Cr_{0.2}Mn_{0.8}O_{3-\delta}$ is also about one order of magnitude higher than in $La_{0.9}Sr_{0.1}Cr_{0.9}Mn_{0.1}O_{3-\delta}$, but the polarization resistance is about one order of magnitude lower in $La_{0.9}Sr_{0.1}Cr_{0.2}Mn_{0.8}O_{3-\delta}$. There is a huge difference in polarization resistance, but no clear correlation between high total conductivities and low polarization resistances can be found. However, at lower Mn concentrations the polarization resistance is rather high in comparison to $La_{0.9}Sr_{0.1}Cr_{0.2}Mn_{0.8}O_{3-\delta}$ with a rather high Mn content. The polarization resistance could therefore depend on the Mn concentration.
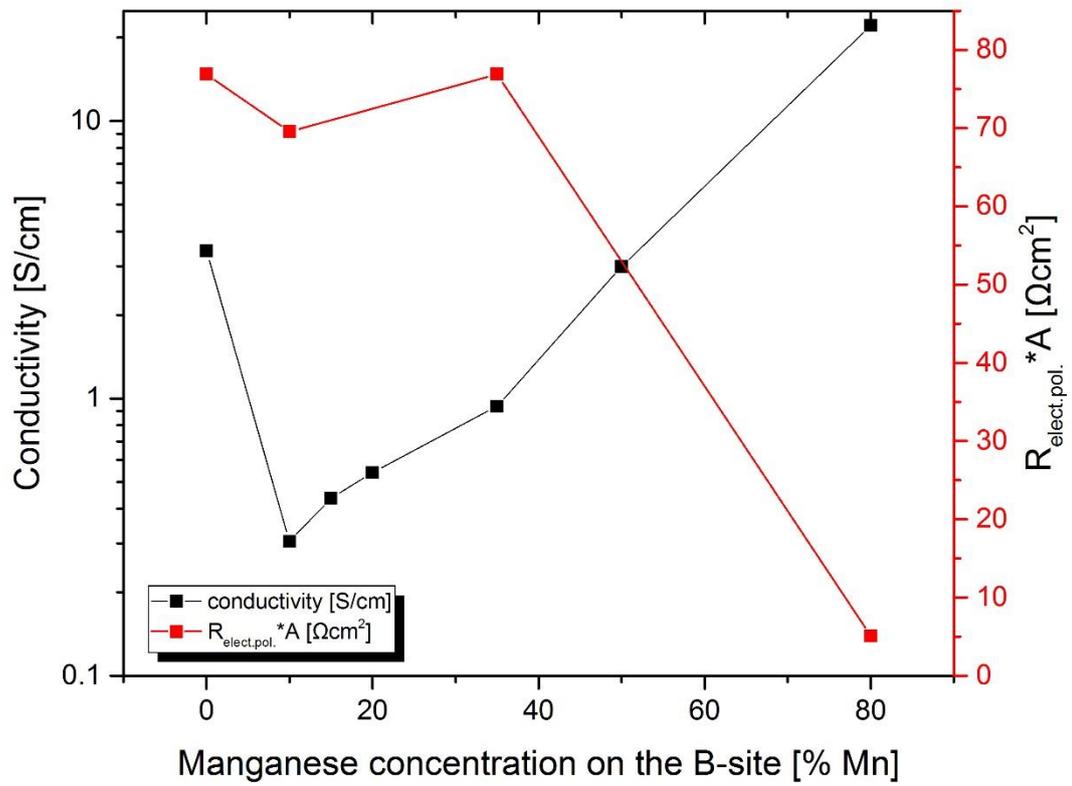
Figure 58: Comparison of the conductivity in humid H_2 and the polarization resistance in humid H_2 for varying Mn concentrations at 810 °C and a constant Sr concentration of 10 %.

4.5.2 Measurements in 100 % O$_2$

Figure 59 shows comparison of the results obtained by the Van-der-Pauw measurements and the EIS measurements under oxidizing atmospheres. The samples with 0 % Mn, 10 % Mn and 80 % Mn demonstrate quite a similar polarization resistance, while the electrode polarization resistance of La$_{0.9}$Sr$_{0.1}$Cr$_{0.65}$Mn$_{0.35}$O$_{3-\delta}$ is higher by a factor of two to three. A maximum in the polarization resistance can be observed approximately at the minimum in conductivity at 810 °C.
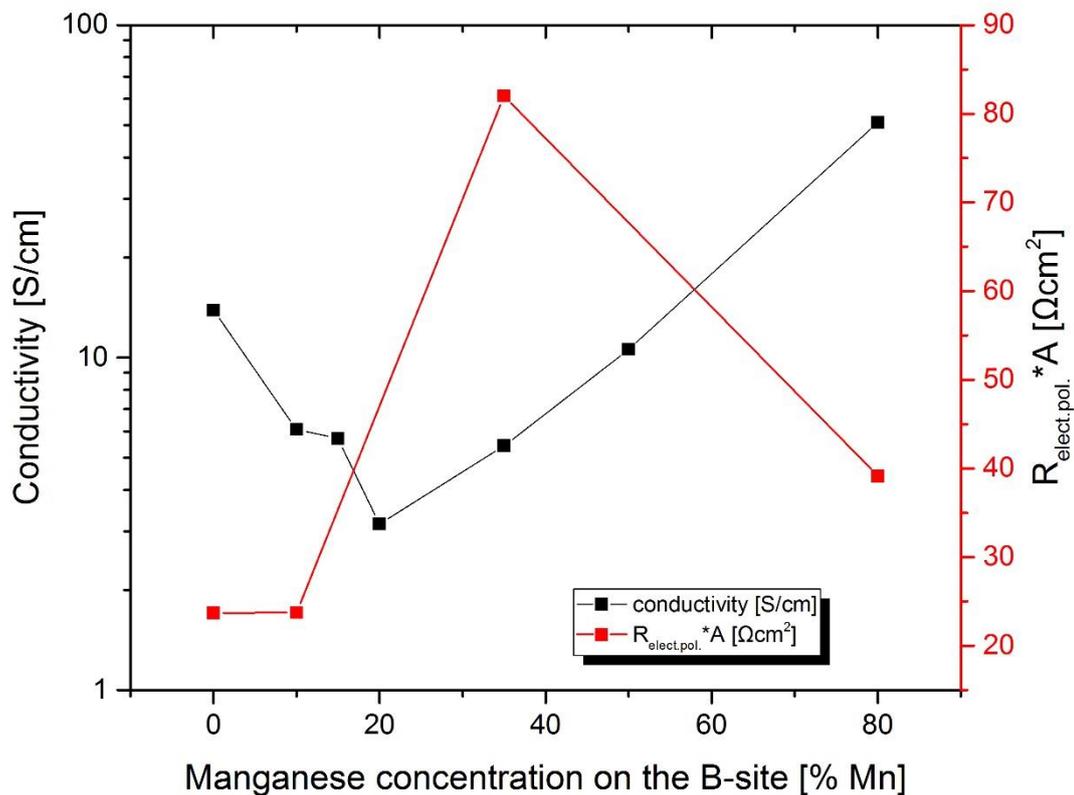
Figure 59: Comparison of the conductivity in 100 % O$_2$ and the polarization resistance in 100 % O$_2$ for varying Mn concentrations at 810 °C and a constant Sr concentration of 10 %.

5 Conclusion

The main findings of this work are as follows:

- Doping $LaCrO_3$ with Sr increases the conductivity in both oxidizing and reducing atmospheres. The increase in conductivity is two orders of magnitude in humid H_2 and one order of magnitude in 1 % O_2 and 100 % O_2 when comparing the undoped $LaCrO_{3-\delta}$ with the sample with 10 % Sr dopant concentration. This increase can be attributed to the formation of electron holes, thus increasing the amount of charge carriers. Further doping does not improve the conductivity to the same extent. A much lower increase or even a plateau-like state is reached at higher Sr dopant concentration of 20 % in humid H_2.

- By varying the Sr dopant concentration in $La_{1-x}Sr_xCr_{0.2}Mn_{0.8}O_{3-\delta}$, it was found that there is a maximum in conductivity at approximately 40 % Sr under oxidizing atmospheres, reaching 146 S/cm at 810 °C in 100 % O_2. The increase in conductivity is more likely to come from an increased mobility due to the Sr doping. The amount of charge carriers does not depend as strongly as supposed on the Sr dopant concentration, however, it might depend on the amount of Mn [26]. Under reducing conditions, a decrease in conductivity was observed when increasing the amount of Sr. This might be explained by electrons as charge carriers in those LSCrM compositions in humid H_2.

- A clear trend in conductivity was found in the measurement series of $La_{0.9}Sr_{0.1}Cr_{1-x}Mn_xO_{3-\delta}$. By varying the Cr:Mn ratio, a minimum results at $La_{0.9}Sr_{0.1}Cr_{0.9}Mn_{0.1}O_{3-\delta}$ under reducing atmosphere and at $La_{0.9}Sr_{0.1}Cr_{0.8}Mn_{0.2}O_{3-\delta}$ under oxidizing atmosphere. This minimum is approximately one order of magnitude lower than the conductivity of $LaCrO_3$. The minimum can be explained by a crossover from multiple trapping to site percolation. Electron holes are trapped on energetically lower Mn sites, thus resulting in a decrease in conductivities at low Mn concentration. When more and more Mn is introduced in the material, site percolation of Mn occurs and an increase in conductivity is observed.

- A correlation between the activation energy and the conductivity was found. Low activation energies are usually observed in compositions with a high conductivity and

vice versa. Activation energies most probably include contributions of both mobilities and concentrations.

- The reason for the pO₂ dependency of the conductivity can be explained with equation 4.4. The oxygen partial pressure influences the concentration of oxygen vacancies and electron holes, thus altering the conductivity of the material. In this study, measurements in 100 % O_2, 1 % O_2 and humid H_2 were carried out, covering a wide range of oxygen partial pressures.

- No clear correlation between total conductivity and the polarization resistance could be found in humid H_2. Materials with high conductivity and materials with low conductivity showed a rather high polarization resistance. The lowest electrode polarization resistance in humid H_2, which was one order of magnitude lower than the polarization resistances of the other materials, was found in $La_{0.9}Sr_{0.1}Cr_{0.2}Mn_{0.8}O_{3-\delta}$, which has the highest amount of Mn of all samples in this study. These findings suggest that Mn plays a vital role for the electrochemical properties of LSCrM regarding the oxidation of H_2.

- In 100 % O_2, the surface polarization resistances at 810 °C seem to follow the trend of the conductivity, resulting in a maximum electrode polarization resistance at 35 % Mn, which is close to the minimum of the conductivity.

- The activation energies for the polarization resistance are higher under oxidizing atmospheres than they are under reducing ones. The corresponding polarization resistances are, however, in general lower in oxidizing atmospheres, with the exception of $La_{0.9}Sr_{0.1}Cr_{0.2}Mn_{0.8}O_{3-\delta}$ in H_2, which has the lowest electrode polarization resistance measured in this work.

- All samples were investigated under both oxidizing and reducing conditions and did not decompose during the measurement. This shows an improved stability of LSCrM when compared to LSM.

6 Outlook

Currently ongoing research in the group deals with the electrochemical characterization of porous $La_{0.9}Sr_{0.1}Cr_{0.2}Mn_{0.8}O_{3-\delta}$/GDC composite anodes. This composite benefits from a high electronic conductivity of $La_{0.9}Sr_{0.1}Cr_{0.2}Mn_{0.8}O_{3-\delta}$ and a high ionic conductivity of GDC, while both materials also exhibit an acceptable conductivity of the respective other type. Therefore, an improved performance is expected. For biphasic LSCrM/LSCrM composite anodes, further investigations by means of impedance spectroscopy have to be carried out. While the Van-der-Pauw method yields the total conductivity, the ionic conductivity does not necessarily follow the same trend. A material with a high total conductivity may exert a low ionic conductivity. ^{18}O tracer diffusion measurements may reveal information on the ionic conductivity. Future research in the working group is going to deal with sulfur poisoning of LSCrM. In order to check the long-term stability in reducing atmosphere, degradation experiments could be conducted as well.

Possible applications of LSCrM include:

- anode materials. $La_{0.9}Sr_{0.1}Cr_{0.2}Mn_{0.8}O_{3-\delta}$ demonstrates a high total conductivity and a low surface polarization resistance. Furthermore, this composition was stable in humid H_2 during the time of the measurement.
- current collectors. Exhibiting a high total conductivity, $La_{0.9}Sr_{0.1}Cr_{0.2}Mn_{0.8}O_{3-\delta}$ can be used as a ceramic current collector.
- cathode materials in symmetrical SOFCs.

7 Appendix

7.1 Glossary

A	Area [m²]
A_T	Prefactor [S*K/cm]
C	Capacitance [F]
c	Concentration [mol/L]
D	Diffusion coefficient [cm²/s]
d	Thickness of the thin film [m]
d	y-intercept []
ΔG	Free enthalpy change [J/mol]
ΔH	Enthalpy change [J/mol]
ΔS	Entropy change [J/mol*K]
E_A	Activation energy [eV]
e_0	Elementary charge [C]
ε	Permittivity [F/m]
F	Faraday constant [C/mol]
f	Geometric factor []
φ	Potential [V]
I	Electrical current [A]
k_B	Boltzmann constant [eV/K]
l	Length of the sample [m]

μ	Chemical potential [J/mol]
μ^0	Chemical potential at standard conditions [J/mol]
$\tilde{\mu}$	Electrochemical potential [J/mol]
n	Charge carrier density [1/L]
n	Reaction unit amount [mol]
N_A	Avogadro constant [1/mol]
Q	Charge [C]
R	Universal gas constant [J/mol*K]
R	Resistance [Ω]
r	Reaction rate [mol/s]
$R_{AB,CD}$	Resistance (current measured between A and B applying a voltage between C and D) [Ω]
$R_{BC,DA}$	Resistance (current measured between B and C applying a voltage between D and A) [Ω]
ρ	Specific resistance [Ωm]
σ	Conductivity [S/m]
T	Absolute temperature [K]
T_{cold}	Lowest temperature within a process [K]
T_{hot}	Highest Temperature within a process [K]
U	Voltage [V]
u	Mobility [cm^2/s*V]
U_c	Open circuit voltage voltage [V]
W_{chem}	Chemical work [J/mol]
W_{el}	Electrical work [J/mol]
ω	Frequency [Hz]

ω_{carnot}	Carnot efficiency []	
$\omega_{el.chem.th}$	theoretical efficiency of an electrochemical process []	
ω_{gas}	efficiency for the gas usage []	
ω_{kin}	Kinetic efficiency []	
ω_P	Peak frequency [Hz]	
ω_r	Efficiency for all remaining processes []	
ω_{th}	Theoretical efficiency []	
ω_{total}	Total efficiency []	
x_i	Normalized concentration []	
z	Valency []	
Z	Impedance [Ω]	

7.2 Acronyms

AFC	Alkaline fuel cell
CIP	Cold isostatic pressing
CPE	Constant phase element
EIS	Electrochemical impedance spectroscopy
DMFC	Direct methanol fuel cell
GDC	Gd doped ceria
LAO	$LaAlO_3$
LSC	$(La, Sr)CoO_{3-\delta}$
LSCr	$(La, Sr)CrO_{3-\delta}$
LSCrM	$(La, Sr)(Cr, Mn)O_{3-\delta}$
LSM	$(La, Sr)MnO_{3-\delta}$
MIEC	Mixed ionic and electronic conductor
MFC	Mass flow controller
MSC	Metal supported cell
PAFC	Phosphoric acid fuel cell
PEMFC	Polymer electrolyte membrane fuel cell
SEM	Scanning electron microscopy
SMU	Source meter unit
SOEC	Solid oxide electrolyzer cell
SOFC	Solid oxide fuel cell
TPB	Triple phase boundary

XRD   X-ray diffraction

YSZ   Yttria-stabilized zirconia

7.3 List of figures

7.4 List of tables

7.5 Bibliography

1. Dell, R.M. and D.A.J. Rand, *Energy storage — a key technology for global energy sustainability.* Journal of Power Sources, 2001. **100**(1–2): p. 2-17.
2. Irvine, J.T.S., *The Bourner lecture: Power sources and the new energy economy.* Journal of Power Sources, 2004. **136**(2): p. 203-207.
3. Bauen, A., *Future energy sources and systems—Acting on climate change and energy security.* Journal of Power Sources, 2006. **157**(2): p. 893-901.
4. Irvine, J.T.S. *Electrochemical conversion of carbon dioxide and water*. in *ACS National Meeting Book of Abstracts*. 2011.
5. Srinivasan, S., *Fuel cells: from fundamentals to applications*. 2006: Springer.
6. Oshinori Kobayshi, Y.A., Tatsuo Kabata, Masanori Nishiura, Kazuo Tomida, Norihisa Matake, *Extremely High-efficiency Thermal Power System-Solid Oxide Fuel Cell (SOFC) Triple Combined-cycle System.* Mitsubishi Heavy Industries Technical Review 2011. **48**(3).
7. Bloom Energy. Available from: http://www.bloomenergy.com/fuel-cell/es5-data-sheet/. Accessed: 10.08.2016
8. Perry Murray, E., M.J. Sever, and S.A. Barnett, *Electrochemical performance of $(La,Sr)(Co,Fe)O_3$–$(Ce,Gd)O_3$ composite cathodes.* Solid State Ionics, 2002. **148**(1–2): p. 27-34.
9. Oh, E.-O., Whang, C.-M., Lee, Y.-R., Lee, J.-H., Yoon, K. J., Kim, B.-K., Son, J.-W., Lee, J.-H., Lee, H.-W., *Thin film yttria-stabilized zirconia electrolyte for intermediate-temperature solid oxide fuel cells (IT-SOFCs) by chemical solution deposition.* Journal of the European Ceramic Society, 2012. **32**(8): p. 1733-1741.
10. de Souza, S., S.J. Visco, and L.C. De Jonghe, *Reduced-Temperature Solid Oxide Fuel Cell Based on YSZ Thin-Film Electrolyte.* Journal of The Electrochemical Society, 1997. **144**(3): p. L35-L37.
11. Chen, Y.-Y. and W.-C.J. Wei, *Processing and characterization of ultra-thin yttria-stabilized zirconia (YSZ) electrolytic films for SOFC.* Solid State Ionics, 2006. **177**(3–4): p. 351-357.
12. Papurello, D., Lanzini, A., Fiorilli, S., Smeacetto, F., Singh, R., Santarelli, M., *Sulfur poisoning in Ni-anode solid oxide fuel cells (SOFCs): Deactivation in single cells and a stack.* Chemical Engineering Journal, 2016. **283**: p. 1224-1233.
13. Chen, H., Wang, F., Wang, W., Chen, D., Li, S., Shao, Z., *H_2S poisoning effect and ways to improve sulfur tolerance of nickel cermet anodes operating on carbonaceous fuels.* Applied Energy, 2016. **179**: p. 765-777.
14. Laurencin, J., Delette, G., Morel, B., Lefebvre-Joud, F., Dupeux, M., *Solid Oxide Fuel Cells damage mechanisms due to Ni-YSZ re-oxidation: Case of the Anode Supported Cell.* Journal of Power Sources, 2009. **192**(2): p. 344-352.
15. Sarantaridis, D., R.A. Rudkin, and A. Atkinson, *Oxidation failure modes of anode-supported solid oxide fuel cells.* Journal of Power Sources, 2008. **180**(2): p. 704-710.
16. Young, J.L. and V.I. Birss, *Crack severity in relation to non-homogeneous Ni oxidation in anode-supported solid oxide fuel cells.* Journal of Power Sources, 2011. **196**(17): p. 7126-7135.
17. Cassidy, M., G. Lindsay, and K. Kendall, *The reduction of nickel ·zirconia cermet anodes and the effects on supported thin electrolytes.* Journal of Power Sources, 1996. **61**(1): p. 189-192.
18. Rüttinger, M., Mücke, R., Franco, T., Büchler, O.,Menzler, N. H., Venskutonis, A., *Metal-supported cells with comparable performance to anode-supported cells in short-term stack environment*. in *ECS Transactions*. 2011.
19. Vasechko, V., D. Roehrens, and J. Malzbender, *Oxidation studies of anodes layer microstructures in metal supported solid oxide fuel cells.* Ceramics International, 2015. **41**(4): p. 5852-5856.

20. Tucker, M.C., *Progress in metal-supported solid oxide fuel cells: A review.* Journal of Power Sources, 2010. **195**(15): p. 4570-4582.

21. Faes, A., Hessler-Wyser, A., Zryd, A., Van Herle, J., *A Review of RedOx Cycling of Solid Oxide Fuel Cells Anode.* Membranes, 2012. **2**(3): p. 585.

22. Choi, Y., Brown, E.C., Haile, S.M., Jung, W.C., *Electrochemically modified, robust solid oxide fuel cell anode for direct-hydrocarbon utilization.* Nano Energy, 2016. **23**: p. 161-171.

23. Yoo, K.B., Park, B.H., Choi, G.M., *Stability and performance of SOFC with SrTiO$_3$-based anode in CH$_4$ fuel.* Solid State Ionics, 2012. **225**: p. 104-107.

24. Cassidy, M., Connor, P.A., Irvine, J.T.S., Savaniu, C.D., *5 - Anodes A2* in *High-Temperature Solid Oxide Fuel Cells for the 21st Century (Second Edition)*, M. Kendall, Editor. 2016, Academic Press: Boston. p. 133-160.

25. Sin, Y.-W., Petrovsky, V., Anderson, H.U.U., *Redox Stable Electrodes for Hydrogen Producing Solid Oxide Electrolyzer.* ECS Transactions, 2007. **2**(29): p. 1-7.

26. Raffaelle, R., Anderson, H.U., Sparlin, D.M., Parris, P.E., *Transport anomalies in the high-temperature hopping conductivity and thermopower of Sr-doped La(Cr,Mn)O$_3$.* Physical Review B, 1991. **43**(10): p. 7991-7999.

27. Tao, S., J.T.S. Irvine, and S.M. Plint, *Methane oxidation at redox stable fuel cell electrode La$_{0.75}$Sr$_{0.25}$Cr$_{0.5}$Mn$_{0.5}$O$_{3-\delta}$.* Journal of Physical Chemistry B, 2006. **110**(43): p. 21771-21776.

28. Ruiz-Morales, J.C., Canales-Vázquez, J., Savaniu, C., Irvine, J. T. S., Nuñez, P., *Materials for symmetrical solid oxide fuel cells*. in *ECS Transactions*. 2007.

29. Boulfrad, S., Nechache, A., Cassidy, M., Traversa, E., Irvine, J.T.S., *Electrochemical impedance spectroscopy investigation of the anodic functionalities and processes in LSCM-CGO-Ni systems*. in *ECS Transactions*. 2015.

30. Konysheva, E. and J.T.S. Irvine, *Thermochemical and structural stability of A- and B-site-substituted perovskites in hydrogen-containing atmosphere.* Chemistry of Materials, 2009. **21**(8): p. 1514-1523.

31. Konysheva, E.Y., X. Xu, and J.T.S. Irvine, *On the existence of A-site deficiency in perovskites and its relation to the electrochemical performance.* Advanced Materials, 2012. **24**(4): p. 528-532.

32. Tao, S. and J.T.S. Irvine, *Phase transition in perovskite oxide La$_{0.75}$Sr$_{0.25}$Cr$_{0.5}$Mn$_{0.5}$O$_{3-\delta}$ observed by in situ high-temperature neutron powder diffraction.* Chemistry of Materials, 2006. **18**(23): p. 5453-5460.

33. Maier, J., *Physical Chemistry of Ionic Materials*. 2005: John Wiley and Sons, Ltd.

34. Kröger, F.A. and H.J. Vink, *Relations between the Concentrations of Imperfections in Crystalline Solids*, in *Solid State Physics*, S. Frederick and T. David, Editors. 1956, Academic Press. p. 307-435.

35. Tilley, R.J.D., *Defects in Solids*. 2008: John Wiley & Sons, Inc.

36. Riess, I., *Mixed ionic-electronic conductors - Material properties and applications.* Solid State Ionics, 2003. **157**(1-4): p. 1-17.

37. Tuller, H.L., *Semiconduction and mixed ionic-electronic conduction in nonstoichiometric oxides: Impact and control.* Solid State Ionics, 1997. **94**(1-4): p. 63-74.

38. Byrnes, S.J.F., *Basic theory and phenomenology of polarons.* 2008.

39. Devreese, J.T., *Polarons.* Encyclopedia of Applied Physics, 1996. **14**: p. 383 – 409.

40. Devreese, J.T., *Fröhlich polarons from 0D to 3D: Concepts and recent developments.* Journal of Physics Condensed Matter, 2007. **19**(25). p. 255201-255224

41. Devreese, J.T. and A.S. Alexandrov, *Fröhlich polaron and bipolaron: Recent developments.* Reports on Progress in Physics, 2009. **72**(6). p. 066501-06653

42. Stephan, L., *Semiconducting transition metal oxides.* Journal of Physics: Condensed Matter, 2015. **27**(28): p. 283203.

43. Scholta, J.J., L.; Rohland, B.; Garche, J.; Bünger, U.; Rakin, P.; Simi M.;. *Small Scale PEM Fuel Cells in Combined Heat/Power Co-generation*. Available from: http://afrodita.rcub.bg.ac.rs/~todorom/tutorials/rad24.html, Accessed: 28.09.2016

44.   *Entropy - a further look.* Available from: http://digipac.ca/chemical/mtom/contents/chapter5/chap5_4.htm. Accessed: 10.08.2016

45.   Minh, N.Q., *Ceramic fuel cells.* Journal of the American Ceramic Society, 1993. **76**(3): p. 563-588.

46.   Minh, N.Q., *Solid oxide fuel cell technology - Features and applications.* Solid State Ionics, 2004. **174**(1-4): p. 271-277.

47.   Cowin, P.I., Petit, C.T.G., Lan, R., Irvine, J.T.S., Tao, S., *Recent progress in the development of anode materials for solid oxide fuel cells.* Advanced Energy Materials, 2011. **1**(3): p. 314-332.

48.   *Solid Oxide Fuel Cells (SOFCs).* Available from: http://www.aki.che.tohoku.ac.jp/~koyama/html/research/SOFC.html. Accessed: 10.08.2016

49.   Badwal, S.P.S., *Stability of solid oxide fuel cell components.* Solid State Ionics, 2001. **143**(1): p. 39-46.

50.   Minh, N.Q. *Development of reversible solid oxide fuel cells (RSOFCs) and stacks.* in *ECS Transactions*. 2011.

51.   Opitz, A.K., Kubicek, M., Huber, S., Huber, T., Holzlechner, G., Hutter, H., Fleig, J., *Thin film cathodes in SOFC research: How to identify oxygen reduction pathways?* Journal of Materials Research, 2013. **28**(16): p. 2085-2105.

52.   Opitz, A.K., Lutz, A., Kubicek, M., Kubel, F., Hutter, H., Fleig, J., *Investigation of the oxygen exchange mechanism on Ptyttria stabilized zirconia at intermediate temperatures: Surface path versus bulk path.* Electrochimica Acta, 2011. **56**(27): p. 9727-9740.

53.   Feng, Z.A., El Gabaly, F., Ye, X., Shen, Z.X., Chueh, W.C., *Fast vacancy-mediated oxygen ion incorporation across the ceria–gas electrochemical interface.* Nat Commun, 2014. **5**.

54.   Chueh, W.C., Hao, Y., Jung, W.C., Haile, S.M., *High electrochemical activity of the oxide phase in model ceria–Pt and ceria–Ni composite anodes.* Nat Mater, 2012. **11**(2): p. 155-161.

55.   *Chemgapedia.* Available from: http://www.chemgapedia.de/vsengine/media/vsc/de/ch/11/aac/vorlesung/kap_5/kap5_9/kap59_3/grafik/perows1_pdb_altref_001.jpg. Accessed: 10.08.2016

56.   Aguiar, P.B.a.J.A., *Ferromagnetism in Mn half-doped LaCrO$_3$ perovskite.* Journal of Applied Physics, 2013. **113**(17): p. 17E309.

57.   Sfeir, J., *LaCrO$_3$-based anodes: stability considerations.* Journal of Power Sources, 2003. **118**(1–2): p. 276-285.

58.   Bastidas, D.M. and J.T.S. Irvine. *LSCM based SOFC a suitable system for direct propane operation.* in *Proceedings of the 1st European Fuel Cell Technology and Applications Conference 2005 - Book of Abstracts*. 2005.

59.   Corre, G.P.G. and J.T.S. Irvine. *Studies on direct ethanol use in SOFCs.* in *ECS Transactions*. 2011. **35**(1): p. 2845-2854

60.   X.J. Chen, Q.L.L., K.A. Khor, S.H. Chan, *High-performance (La,Sr)(Cr,Mn)O$_3$/(Gd,Ce)O$_{2-\delta}$ composite anode for direct oxidation of methane.* Journal of Power Sources, 2007(165): p. 34-40.

61.   Tao, S. and J.T.S. Irvine, *Synthesis and Characterization of (La$_{0.75}$Sr$_{0.25}$)Cr$_{0.5}$Mn$_{0.5}$O$_{3-\delta}$, a Redox-Stable, Efficient Perovskite Anode for SOFCs.* Journal of the Electrochemical Society, 2004. **151**(2): p. A252-A259.

62.   Kharton, V.V., Tsipis, E.V., Marozau, I.P., Viskup, A.P., Frade, J.R., Irvine, J.T.S., *Mixed conductivity and electrochemical behavior of (La$_{0.75}$Sr$_{0.25}$)$_{0.95}$Cr$_{0.5}$Mn$_{0.5}$O$_{3-\delta}$.* Solid State Ionics, 2007. **178**(1-2): p. 101-113.

63.   Bastidas, D.M., S. Tao, and J.T.S. Irvine, *A symmetrical solid oxide fuel cell demonstrating redox stable perovskite electrodes.* Journal of Materials Chemistry, 2006. **16**(17): p. 1603-1605.

64.   Ruiz-Morales, J.C., Canales-Vázquez, J., Ballesteros-Pérez, B., Peña-Martínez, J., Marrero-López, D., Irvine, J.T.S., Núñez, P., *LSCM-(YSZ-CGO) composites as improved symmetrical electrodes for solid oxide fuel cells.* Journal of the European Ceramic Society, 2007. **27**(13-15): p. 4223-4227.

65. Ruiz-Morales, J.C., Canales-Vázquez, J., Lincke, H., Peña-Martínez, J., Marrero-López, D., Pérez-Coll, D., Irvine, J.T.S., Núñez, P., *Potential electrode materials for symmetrical solid oxide fuel cells.* Boletin de la Sociedad Espanola de Ceramica y Vidrio, 2008. **47**(4): p. 183-188.

66. Ruiz-Morales, J.C., Marrero-López, D., Canales-Vázquez, J., Irvine, J.T.S., *Symmetric and reversible solid oxide fuel cells.* RSC Advances, 2011. **1**(8): p. 1403-1414.

67. Yang, X. and J.T.S. Irvine, *$(La_{0.75}Sr_{0.25})_{0.95}Mn_{0.5}Cr_{0.5}O_3$ as the cathode of solid oxide electrolysis cells for high temperature hydrogen production from steam.* Journal of Materials Chemistry, 2008. **18**(20): p. 2349-2354.

68. van der Pauw, L.J., *A method of measuring specific resistivity and Hall effect of discs of arbitrary shape.* Philips Research Reports, 1958. **13**(1): p. 1-9.

69. van der Pauw, L.J., *A Method of Measuring the Resistivity and Hall Coefficient on Lamellae and Arbitrary Shape.* Philips Technical Review, 1958/59. **20**(8): p. 220-224.

70. *Wikimedia Commons*; Available from: https://commons.wikimedia.org/wiki/File:Vanderpauwshape.png. Accessed: 10.08.2016

71. Huber, T.M., Kubicek, M., Opitz, A. K., Fleig, J., *The relevance of different oxygen reduction pathways of $La_{0.8}Sr_{0.2}MnO_3$ (LSM) thin film model electrodes.* Journal of the Electrochemical Society, 2015. **162**(3): p. F229-F242.

72. Han, J.W., Jalili, H., Kuru, Y., Cai, Z., Yildiz, B., *Strain Effects on the Surface Chemistry of $La_{0.7}Sr_{0.3}MnO_3$.* ECS Transactions, 2011. **35**(1): p. 2097-2104.

73. T.M. Huber, E.N., G. Harrington, Y. Chen, D. Mendler, J. K. Sasaki, J. Fleig, B. Yildiz, and H. Tuller, *Limitations of Grain Boundary Engineering - Ionic Versus Electronic Conductivity.* In preparation.

74. Gupta, S., M.K. Mahapatra, and P. Singh, *Phase transformation, thermal expansion and electrical conductivity of lanthanum chromite.* Materials Research Bulletin, 2013. **48**(9): p. 3262-3267.

75. Jiang, S.P., Liu, L., Ong, K.P., Wu, P., Li, J., Pu, J., *Electrical conductivity and performance of doped $LaCrO_3$ perovskite oxides for solid oxide fuel cells.* Journal of Power Sources, 2008. **176**(1): p. 82-89.

76. Ahlgren, E.O. and F.W. Poulsen, *Thermoelectric power and electrical conductivity of strontium-doped lanthanum manganite.* Solid State Ionics, 1996. **86-88**(PART 2): p. 1173-1178.

77. Raffaelle, R., Anderson, H.U., Sparlin, D.M., Parris, P.E., *Evidence for a crossover from multiple trapping to percolation in the high-temperature electrical conductivity of Mn-doped $LaCrO_3$.* Physical Review Letters, 1990. **65**(11): p. 1383-1386.

78. van Roosmalen, J.A.M. and E.H.P. Cordfunke, *The Defect Chemistry of $LaMnO_{3\pm\delta}$. 4. Defect Model for $LaMnO_{3+\delta}$.* Journal of Solid State Chemistry, 1994. **110**(1): p. 109-112.

79. van Roosmalen, J.A.M., J.P.P. Huijsmans, and L. Plomp, *Electrical conductivity in $La_{1-x}Sr_xMnO_{3+\delta}$.* Solid State Ionics, 1993. **66**(3-4): p. 279-284.

80. Darvish, S., Sabarou, H., Saxena, S.K., Zhong, Y., *Quantitative Defect Chemistry Analysis and Electronic Conductivity Prediction of $La_{0.8}Sr_{0.2}MnO_{3\pm\delta}$ Perovskite.* Journal of The Electrochemical Society, 2015. **162**(9): p. E134-E140.

81. Plint, S.M., Connor, P.A., Tao, S., Irvine, J.T.S. *Electronic transport in the novel SOFC anode material $La_{1-x}Sr_xCr_{0.5}Mn_{0.5}O_{3+\delta}$.* Solid State Ionics, 2006. **177**(19-25 SPEC. ISS.): p. 2005-2008.

82. Nenning, A., Opitz, A. K., Huber, T. M., Fleig, J., *A novel approach for analyzing electrochemical properties of mixed conducting solid oxide fuel cell anode materials by impedance spectroscopy.* Physical Chemistry Chemical Physics, 2014. **16**(40): p. 22321-22336.

83. Kogler, S., Nenning, A., Rupp, G.M., Opitz, A.K., Fleig, J., *Comparison of electrochemical properties of $La_{0.6}Sr_{0.4}FeO_{3-\delta}$; Thin film electrodes: Oxidizing vs. reducing conditions.* Journal of the Electrochemical Society, 2015. **162**(3): p. F317-F326.

84. Nenning, A.V., L.; Miller, E.; Barnett, S.; Fleig, J., *The electrochemical properties of $Sr(Ti,Fe)O_{3-\delta}$ for anodes in solid oxide fuel cells.* In preparation.